Superhydrophobic Micro- and Nano-structured Surfaces: Fabrication, Wetting, and Evaporation

by

Ahmed Mahmood Aldhaleai

A thesis submitted in partial fulfillment of the requirements for the degree of

Master of Science

Department of Mechanical Engineering
University of Alberta

Abstract

Water-repellent, superhydrophobic (SH) surfaces have attracted a remarkable interest in researchers for both purely academic pursuits and industrial applications, including nanofluidics and microfluidics, coatings, and drag reduction, due to their unique self-cleaning and drag reduction properties. This thesis presents the synthesis, characterization, and application of superhydrophobic surfaces, which are inspired by lotus-leaf surfaces that repel water droplets. More specifically, we investigate the effects of nanograss structure and additive surfactant on both droplet wetting and evaporation dynamics. We furthermore use a thermodynamic model to design and fabricate SH surfaces using additive manufacturing.

We first investigated the initial wetting state, evaporating dynamics, and contact line movement of a naturally-evaporating water droplet on such SH surfaces of random nano-scale roughness, with an extremely low solid packing fraction, and surface roughness. Systematic measurements of the droplet contact angle, base diameter, height, and volume were performed for several SH nanograss surfaces. Our results show that all the droplets deposited initially form a gas-trapping, Cassie-Baxter state. Small droplets subsequently evaporate with a constant contact angle mode, followed by a mixed mode at the end of the droplet lifetime. On the contrary, for relatively large droplets, two distinct evaporation modes are found. Some of the larger evaporating droplets were initially in a constant contact angle mode and underwent a mixed mode, while others began with a mixed mode with slowly decreasing base diameter and contact angle. By increasing the droplet size, for the first time, stick-slip motions of the contact line for large droplets on SH nanograss surfaces were studied. The experimental data of contact angle-dependent evaporative mass flux are found to nearly collapse onto one universal curve for different droplet sizes and initial contact angles, in agreement with an evaporative cooling model.

To study the effect of the aqueous surfactant solutions on the wetting and the contact angle behavior of SH microstructures with high and low roughness levels, we experimentally and theoretically examine the influence of a double chain cationic surfactant, didodecyldimethylammonium bromide (DDAB), on the wetting states and contact angles on SH surfaces made of hydrophobic micro-cylinders. We use two types of micro-patterns of different surface roughness, r, and packing fraction, ϕ, and vary nine surfactant concentrations (C_{S}) in the experiments. At low C_{S}, some of the surfactant-laden droplets are in a gas-trapping, CB state on the high-roughness microstructures. In contrast, some droplets are in a thoroughly wetting Wenzel (W) state on the low-roughness microtextures. We found that the contact angle of CB drops can be well predicted using a thermodynamic model considering surfactant adsorption at the liquid-vapor (LV) and solid-liquid (SL) interfaces. At high C_{S}, however, all the DDAB drops wet on W mode. Based on a Gibbsian thermodynamic analysis, we find that for the two types of SH surfaces used, Wenzel state has the lowest thermodynamic energy and thus is more favorable theoretically. The CB state, however, is metastable at low C_{S} due to a thermodynamic energy barrier.

Although the SH surfaces fabricated using nano- or micromachining technologies are well-repelled water and other fluids, their fabrication processes can be complicated, time-consuming, and expensive. We report facile and simple (one- and two-step) approaches to fabricate SH surfaces with high contact angle (CA) and low roll-off angle (ROA) for self-cleaning and water-repellent applications. Using the one-step method, we are able to produce transparent superhydrophobic (TSH) surfaces with random roughness to study the effect of the regular patterns vs. the arbitrary structures in the SH CA and the wetting properties. In the two-step process, we incorporate a 3D-printing technique with the hydrophobic coating to produce robust SH textures composed of regular square pillars, which are designed according to a thermodynamic theory for a stable gas-trapping CB state. Our measurements of static and dynamic CAs of water drops on all the prepared SH surfaces agree well with a Cassie–Baxter model.

In summary, this thesis work contributes to a better understanding of the wetting and evaporation dynamics of pure water and surfactant drops on SH surfaces of different roughnesses and packing fraction levels. In particular, additive surfactants has strong effects on the wetting characteristics at high concentrations.

Preface

The majority of the experimental work presented in this thesis was performed by Ahmed Mahmood Aldhaleai under the supervision of Professor Peichun Amy Tsai. The work presented in Chapter 2 is done through collaboration with the nanograss SH samples fabricated by Dr. Faheem Khan.

Chapter 2 is based on a manuscript recently submitted to the International Journal of Heat and Mass Transfer: Ahmed Aldhaleai, Faheem Khan, Thomas Thundat, and Peichun Amy Tsai, "Evaporation Dynamics of Water Droplets on Superhydrophobic Nanograss Surfaces", under revision, 2020.

Chapter 3 of the thesis is taken from the journal paper by Ahmed Aldhaleai and Peichun Amy Tsai, "Effect of a Cationic Surfactant on Droplet Wetting on Superhydrophobic Surfaces", Langmuir, 36, 16, 4308-4316, 2020.

Chapter 4 is based on a manuscript recently submitted to Additive Manufacturing: Ahmed Aldhaleai and Peichun Amy Tsai, "Fabrication of transparent and microstructured superhydrophobic substrates using additive manufacturing", submitted, 2020.

Acknowledgements

First and foremost, I would like to express my sincere appreciation to my supervisor, Prof. Peichun Amy Tsai, for her research ideas, kind guidance and support, training, perseverance, constant encouragement, patience, and for providing me with many opportunities to develop my professional and technical skills, which have helped me constantly progressing throughout the research project to complete my master thesis.

I would like to extend my thanks to all my group members for their support for my work. I would like to express my sincere gratitude to Masoud Bozorg Bigdeli, Tsai-Hsing Ho, and Sourayon Chanda for their selfless help and encouragement, comments and suggestions on the experiments and data analysis.

I would like to express my appreciation and deepest affection to all my friends for their support and encouragement throughout this research, I would especially like to thank Ahmed Humadi, who has been a family away from home.

More importantly, a special thanks to the Hadhramout Establishment for Human Development (HEHD) for their financial support cooperation that helped me throughout my program.

Last but not least, I would like to thank my parents for their endless love and unconditional support throughout my whole life.

Contents

List of Tables

List of Figures

Chapter 1

Introduction

1.1 Wetting Phenomenon on a solid surface

The interaction between a solid and a liquid phase is known as surface wetting behavior. Wetting is one of the most common phenomena in daily life, and its application can be easily found in watercolor painting [1], droplet-based microfluidics [2], DNA extraction [3], inkjet printing [4, 5, 6], and so on. An understanding of the wetting phenomena of solids by liquids is essential in research, medical, and industrial processes, ranging from artificial tissue engineering to practical applications such as self-cleaning, oil-water separation, and anti-icing textiles. Especially surfaces with high liquid repellency, mostly inspired by nature, have attracted great attention in the last decade.

The contact angle is the angle where the intersection between the liquid-gas (lg) interface meets a solid-liquid (sl) interface, and it is used for the characterization of surface wettability.

1.1.1 Wetting on smooth surface

The wetting behavior on a flat and chemically homogeneous surface can be described by Young's [7] equation by balancing the interfacial forces at the three-phase contact line:

$$\cos\theta_Y = \frac{\gamma_{sg} - \gamma_{sl}}{\gamma_{lg}}. \tag{1.1}$$

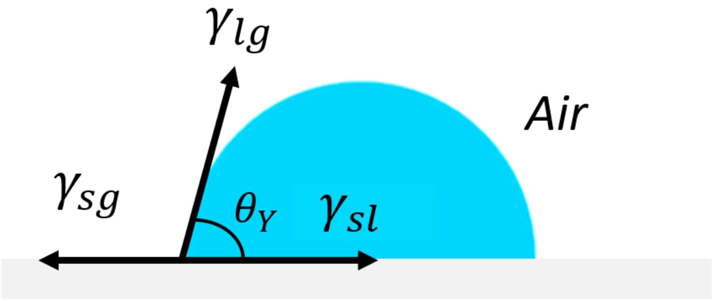

Figure 1.1. Schematic view of the droplet contact angle as in Young's equation.

Here γ_{sg} is the solid-gas (sg) surface tension, γ_{sl} is the solid-liquid interfacial tension, γ_{lg} is the liquid-gas interfacial tension, and θ_Y is the macroscopic Young's contact angle in a thermodynamic equilibrium.

1.1.2 Wetting on a rough surface: Wenzel's and Cassie's models

Since an ideally smooth and homogeneous surface does not exist in reality, micro- or nano-roughness, defects, or chemical heterogeneities can affect the wetting properties significantly. Surface hydrophobicity or hydrophilicity can be adjusted by either increasing or decreasing the surface roughness. In 1936 Wenzel (W) published a pioneering study on how surface roughness affects the apparent contact angle [8]. A roughness factor here (r) is defined as the ratio between the actual surface area beneath the drop and the horizontally projected area on a 2D plane. In the Wenzel model, the drop is deposited on a surface, and it is assumed that the droplet completely wets the asperities of the rough surface. The apparent contact angle on such a rough surface (θ_W) can be described as:

$$\cos\theta_W = r\cos\theta_Y, \tag{1.2}$$

which relates Young's contact angle, θ_Y, to the W apparent contact angle, θ_W. The W equation predicts that the apparent contact angle decreases on a hydrophilic material and increases on a hydrophobic material with increasing the surface roughness level. However, for an extremely rough, hydrophobic surface, the W model predicts a total drying of the surface ($\theta_W = 180°$), which is not physical due to the lack of contact between the drop and

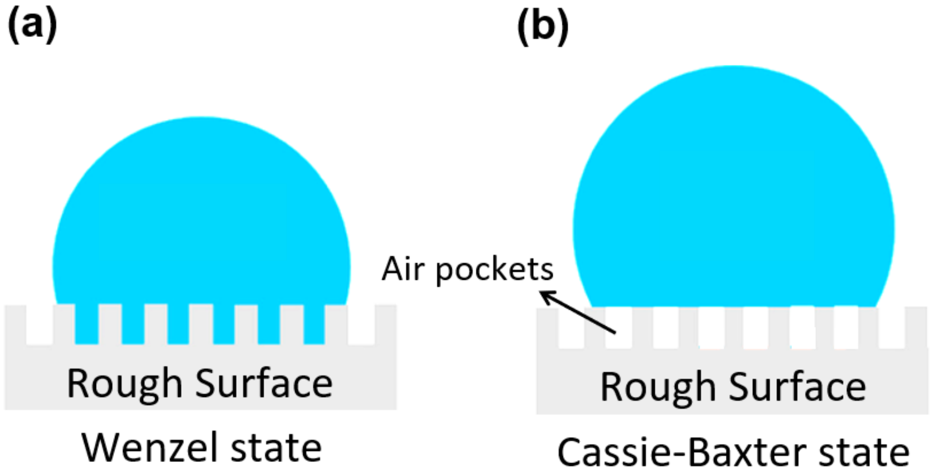

Figure 1.2. Scheme of (a) Wenzel's model and (b) Cassie-Baxter's model on rough surfaces.

the substrate. In this case, it is energetically favorable that the liquid drop rests on air pockets and touches the surface only on top of the asperities leading to a composite surface, which implies that a part of the surface under the drop remains dry.

The composite wetting regime was addressed in 1944 by Cassie and Baxter (CB) [9], the apparent contact angle on a composite surface consisting of two materials can be predicted from the following equation:

$$\cos\theta_{CB} = f_1 \cos\theta_1 + f_2 \cos\theta_2, \tag{1.3}$$

where θ_{CB} is the CB apparent contact angle, θ_1 and θ_2 are the contact angles on two different kinds of materials, and f_1 and f_2 are the fractional surface areas of the two components being in contact with the liquid drop. By considering that the liquid fully rests on air, the "contact angle" at the liquid-air interface would be 180° and $f_2 = 1 - f_1$. Here, the solid-liquid fraction f_1 can be replaced by ϕ. More precisely, the contact angle of such a "fakir" drop is an average between the angles on solid, and on air, equation (1.3) can be rewritten as follows:

$$\cos\theta_{CB} = \phi\cos\theta_Y + \phi - 1, \tag{1.4}$$

where ϕ represents the solid-liquid fraction under the contact area, θ_Y is Young's contact angle on a flat surface. This suggests that to achieve a high apparent contact angle, the contribution from the solid phase; should be as small as possible. In general, the more stable wetting state (either Wenzel or Cassie–Baxter) is determined by which exhibits the lower apparent contact angle. However, the Cassie–Baxter state may be kinetically trapped into a metastable state, even when the Wenzel state would be energetically favorable. Furthermore, in certain systems, transitions between the two wetting regimes can occur spontaneously, or they may be induced by an external stimulus.

1.1.3 Wetting Transition

Wetting transition or so-called Cassie-Baxter to Wenzel state transition is an irreversible process since the droplet in Wenzel state is more energetically favorable than the droplet in Cassie state. Such transition could be spontaneous or caused by many factors, such as drop impact from a certain height, external pressure on a droplet, evaporation of droplets on rough solid surfaces, or substrate vibration [10, 11, 12]. In the Wenzel model, the surface roughness can be defined as r [8]:

$$r = \frac{\cos\theta_W}{\cos\theta_Y}, \tag{1.5}$$

where θ_W is W apparent contact angle, and θ_Y is Young's contact angle. The apparent contact angle here can be estimated by minimizing the surface energy of a droplet. While in Cassie-Baxter state, because of the air trapped beneath a droplet on the solid surface, the contact angle is determined by the value on-air (180°) and θ_{CB} on the solid surface as shown previously. The solid-liquid fraction, ϕ, will be determined as follows [9]:

$$\phi = \frac{\cos\theta_{CB} + 1}{cos\theta_Y + 1}. \tag{1.6}$$

This equation is applicable for very rough surfaces with a large value of (r) or very hydrophobic surfaces (large θ_Y), while the Wenzel equation can hold for slightly hydrophobic solids (θ_Y just above 90°). Both equations (1.5) and (1.6) should thus be successively applied as the contact angle increases. To obtain the critical contact angle between the two states, one can use a model based on the comparison of the global surface energies, E_{CB} and E_W, for a CB and the Wenzel wetting droplet on the rough surfaces, respectively. The total surface energy E_{CB} or E_W is the magnitude of the total energies needed for creating interfaces when placing a CB or Wenzel drop onto the rough surfaces. Based on thermodynamics, a stable CB occurs when E_{CB} has a lower energy compared to that of a W wetting mode, i.e., $E_{CB} < E_W$, by tuning the surface parameters of r and ϕ. The total surface energies for the two states on the rough surfaces can be calculated using the roughness, r, and the solid fraction, ϕ [11, 13, 14, 15, 16]:

$$E_{\mathrm{CB}} = \ S_{\mathrm{b}}\ [\gamma_{\mathrm{sg}} r + \gamma_{\mathrm{lg}}(1 - \phi\ (1 + \cos\theta_{\mathrm{Y}}))] + \gamma_{\mathrm{lg}} S_{\mathrm{cap}}\ , \tag{1.7}$$

$$E_{\mathrm{W}} = S_{\mathrm{b}}\ [\gamma_{\mathrm{sg}} r - \gamma_{\mathrm{lg}} r \cos\theta_{\mathrm{Y}}] + \gamma_{\mathrm{lg}} S_{\mathrm{cap}}, \tag{1.8}$$

where γ_{sg} and γ_{lg} are the interfacial tensions for the solid-gas and liquid-gas interfaces, respectively, S_{cap} is the spherical cap surface area of the water drop entirely in contact with the air, and S_{b} is the base surface area.

One can arrive at the physical criterion of the critical contact angle θ^* that delineates the surface parameters for a stable CB vs. Wenzel state, by equating $E_{CB} = E_W$:

$$\cos\theta^* = \frac{\phi - 1}{r - \phi}. \tag{1.9}$$

From this equation, three states will be defined based on the contact angle. These regions will be summarized in Fig. 1.3. Figure 1.3 showed that for a moderate hydrophobicity where $90° < \theta_Y < \theta^*$, the apparent contact angle θ is fits better W model and the water penetrates surface texture. However, if $\theta_Y > \theta^*$, the water droplet will be sitting on the air pockets where the air remains trapped below the drop, and θ should be obtained using CB equation. A dotted line describes the metastable CB regime, and it is also reported that the CB regime is observed when $\theta_Y < \theta^*$ despite high surface energy.

We used the criterion discussed above to divide the wetting states into stable CB, metastable CB, and stable Wenzel states. However, the stability of the superhydrophobic surfaces (the thin air film separating the substrate from the water in the CB state) was studied in underwater experiments. Lee et al. [17] fabricated hydrophobic microstructures of a certain geometric criterion on hydrophobic nanostructured surfaces integrated with a measure for self-limiting electrolysis. The surfaces studied here maintained gas-trapped state under high liquid pressure up to 7 atm as well as in the presence of surface defects. Another study was done by Poetes et al. [18] using plastron superhydrophobic surfaces. Here, the stability of the plastron was studied in underwater experiments. The lifetime of the gas-trapped state of the plastron exhibited a rapid decrease from 385 hours to 1 hour by increasing the immersion depth from 0.3 m to 1.35 m, respectively.

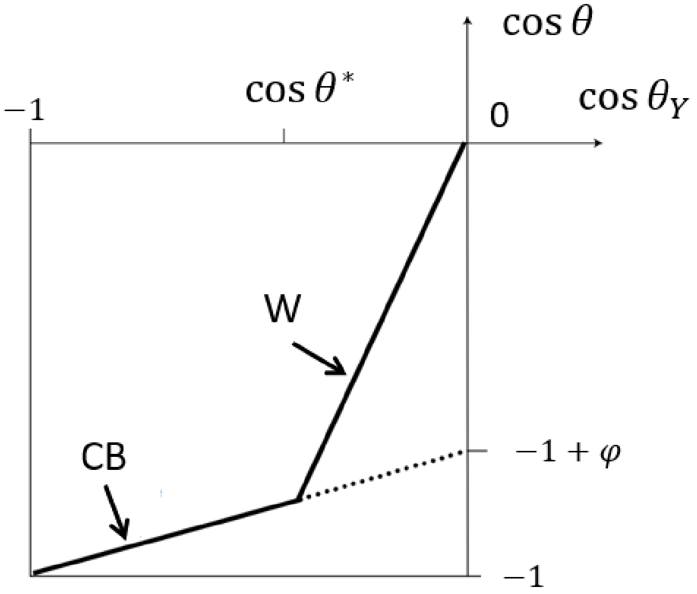

Figure 1.3. The relationship between Wenzel and Cassie models. Figure adapted from reference [19].

1.1.4 Contact angle hysteresis

A contact angle hysteresis (CAH) is an alternative evaluation of liquid mobility on a surface. When a small enough amount of liquid is added to a drop, the contact line will still be pinned, and the contact angle will increase; similarly, if a small enough amount of liquid is withdrawn from a drop, the contact line will still be pinned, and the contact angle will decrease. Therefore, a drop sitting on the solid surface has a range of contact angles from the advancing (maximal) contact angle to the receding (minimal) contact angle. The contact

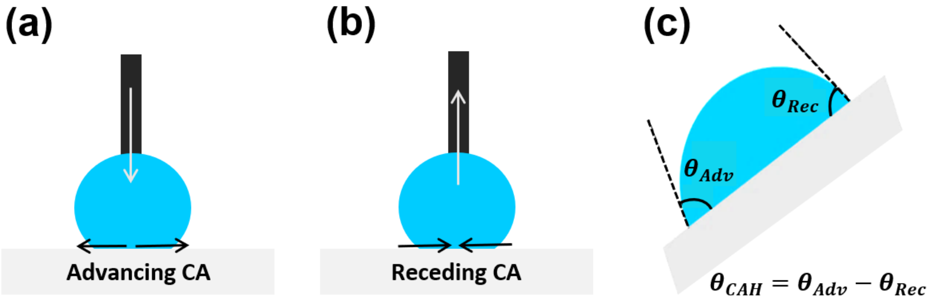

Figure 1.4. Schemes of (a) Advancing and (b) receding contact angle measurement using the captive-drop goniometry (CDG) method. (c) Advancing and receding contact angle using tilting-plate goniometry (TPG) method [21].

angle hysteresis, θ_{CAH}, is normally defined as the difference between the advancing contact angle (θ_{Adv}) and receding contact angle (θ_{Rec}) [20]:

$$\theta_{CAH} = \theta_{Adv} - \theta_{Rec}. \tag{1.10}$$

To measure the advancing and receding contact angles, two widely methods used: captive-drop goniometry (CDG) and tilting-plate goniometry (TPG) [21].

First, captive-drop goniometry (CDG): in captive-drop goniometry (CDG) method, the advancing contact angle is measured while adding volume into a droplet to the maximum just before the contact line of solid-air-liquid phase advances, while the receding contact angle is measured when removing volume from a droplet just before the reduction of the contact line of solid-air-liquid phases (as shown in Fig.1.4 (a-b)).

Second, tilting-plate goniometry (TPG): The tilting-plate goniometry measures the advancing and receding contact angles on both sides of a liquid droplet (left and right) when the solid surface is tilted at the sliding angle of this droplet towards the surface, as shown in Fig. 1.4c. In some cases, the liquid droplet does not leave the surface even when the surface is turned upside down (180°); here the advancing and receding contact angles are measured when the surface is tilted at 90°. According to equation (1.10), we can see that the tilting angle depends on the advancing and receding contact angle instead of the static contact angle. A smaller contact angle hysteresis is required to fabricate superhydrophobic surfaces. For a superhydrophobic surface, not only the static contact angle but also the tilting angle should be considered, which means droplets on the surface can easily escape at a certain angle ($\theta_{CAH} < 10°$). This small angle required in many applications, such as self-cleaning.

1.2 Superhydrophobicity

Both surface energy and surface roughness have a remarkable effect on the wetting properties (contact angle) of solid surfaces [11, 22]. Based on the contact angle between the drop and the solid surface, there are two types of surfaces: hydrophobic and hydrophilic. A hydrophobic material is known for its ability to repel water, which is different than the hydrophilic material that can easily get wet. The basis of these expressions comes from the Greek words "hydro" which means "water" and postfix "phobos" and "philia" meaning "fear" and "love" respectively. Both hydrophobic and hydrophilic materials can be characterized using static and dynamic contact angles. Based on the contact angle between the droplet and the surface, the surface called hydrophilic if the contact angle is below 90°. Conversely, hydrophobic surfaces have a contact angle above 90°. In a special case, when the contact angle is between 150° and 180°, and contact angle hysteresis (CAH) is less than 10°, the surface is called superhydrophobic (SH) [12, 23].

1.2.1 History of Superhydrophobic Materials

The research on surfaces with a high contact angle started a long time ago. Between 1907 and 1923, high contact angles (CA) around 160° and above were observed on surfaces coated with soot, arsenic trioxide and lycopodium powder, and another with galena modified with steric acids shows that research relating to superhydrophobic materials dates back a long time [23]. A few years later, Wenzel, Cassie and Baxter initiated the basics behind superhydrophobic phenomena [8, 9, 23]. After that, the research regarding such surfaces progressed slowly, especially according to surface geometry and or surface roughness effects on wetting behavior until 1996 when T. Onda et al. fabricated a super-water-repellent fractal surface made of alkylketene dimer with a water contact angle on this surface as large as 174° [24]. A year later, the origin of the "lotus effect" in nature was described by Neinhuis and Barthlott as a natural source of superhydrophobic surfaces [23]. They showed that the epicuticular wax crystalloids of such plants are responsible for their water repellent and self-cleaning properties [25, 26, 27]. Since then, significant research efforts have been devoted towards the understanding of the surface structure of different plants and animals that have similar properties and then the fabrication of such superhydrophobic coatings using relatively simple and inexpensive techniques. Most of the techniques presented in the literature include micro- and nanofabrication and chemical processes. For example, etching [28, 29], polymer coating [30], replica molding [31], self-assembly [32, 33], and electrospinning [34]. Superhydrophobic materials have become significant for many applications, including self-cleaning [35, 36], anti-fog [37, 38], anti-corrosion [39, 40], drag reduction [41, 42], and anti-icing surfaces [43, 44].

1.2.2 Existence of Superhydrophobicity in Nature

Considerable examples of superhydrophobic materials have existed in nature and have inspired researchers to duplicate them artificially. Taking the lotus leaf (Nelumbo nucifera) as an example of a naturally occurring superhydrophobic surface. This leaf is provided with a hierarchical surface structure (epicuticular wax crystals), which is responsible for the superhydrophobicity and the self-cleaning properties of such a plant. Once the lotus leaf is tilted, water droplets roll off the surface and collect dust and any other containment along the way due to the micro and nanoscale roughness on the leaf surface. Such micro- and nanoscale

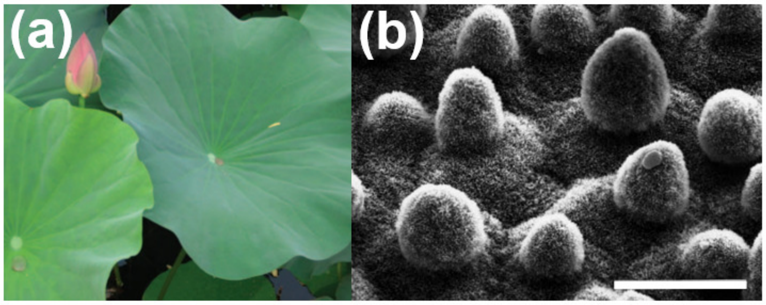

Figure 1.5. Superhydrophobic surface in nature. (a) Lotus leaves. (b) SEM image of the surface structures on the lotus leaf. The scale bar represents 20 μm. The figure is extracted from [23].

roughness decreases the adhesion and the contact area between the water droplets resulting from rain or fog, thereby enhancing the easy roll-off of these droplets from the surface of the leaf. Indian Cress (Tropaeolum majus) is another example of a self-cleaning water-repelling leaf with microscopic length-scale surface roughness [45]. Butterfly wings are also another example of superhydrophobic material that is responsible for protecting their body from water and contaminants through the hierarchical structure that makes their surface superhydrophobic [46]. These examples demonstrate that superhydrophobic behaviors exist widely in nature among plants and animals.

1.2.3 Applications of Superhydrophobicity in Science and Engineering

Superhydrophobicity is a term that has been used to describe extremely water repellent rough surfaces. There are many applications for superhydrophobic surfaces in both science and engineering. The most obvious uses for superhydrophobic surfaces are to repel water, which allows the surface to clean itself. The self-cleaning and water repellent properties are indeed used to make waterproof coating since we are surrounded by many surfaces that need to be clean, from window panels to car windshields and house walls. Apart from self-cleaning and water-repellent properties, superhydrophobic surfaces have a lot more applications, such as drag reduction, anti-corrosion, anti-bacterial, anti-icing, and oil-water separation.

I. **Drag reduction:** superhydrophobic surfaces can reduce the drag in the water by reducing the interaction between the water and the surface. This led to the formation of a thin air layer at the interface, which enhances the mobility of water droplets to travel on the superhydrophobic surfaces. Drag reduction in superhydrophobic surfaces has been investigated in-depth in recent years. For instance, superhydrophobic surfaces can be used on ships so they can travel with less energy consumption and drag in the water [41, 42, 47, 48, 49].

II. **Oil-water separation:** another significant application of superhydrophobic surfaces is in the field of oil-water separation. In most cases, these surfaces can be easily wetted by liquids with low surface tensions such as hydrocarbons than that of water. In this case, the superhydrophobic surfaces will be treated mostly on the membrane for oil-water separation

[50, 51]. Feng et al. showed that a mesh coated with PTFE revealed two different wettability behaviors for oil and water. For oil, it showed complete wetting (superoleophilic) property, while for water, it changed to an extremely nonwetting surface (superhydrophobic). The utmost difference in wettability for oil and water manifested the possibility to separate oil and water [52, 53, 54, 55].

III. **Anti-corrosion:** corrosion-induced failure plays a significant role, especially in microelectronic devices, pipelines, aircraft, and automobiles, leading to an enormous economic loss. The major type of corrosion is known as iron rushing. This kind is occurring mainly due to the exposure of metals to water and oxygen. To prevent such problem from happening and to improve the reliability of such devices is to coat them with superhydrophobic coatings that will enhance their water-repellency and anti-corrosion properties [35, 39].

IV. **Anti-icing:** when surfaces exposed to ice through freezing rain or super-cooled water, especially during winter in cold-climate regions, serious problems or sometimes material damage will occur to such surfaces. To protect these surfaces and delay the ice formation, superhydrophobic surfaces are a good option due to the least fraction of water contact [43, 44, 56].

1.2.4 Fabrication Methods for Superhydrophobic Surfaces

A superhydrophobic surface idea is mostly inspired by the “lotus leaf” due to the micro- and nanoscopic structure on the surface of this plant, and the entire surface is covered by a low surface energy wax. The existence of both low surface energy material and micro- and nano-scale roughness reduces the adhesion of water drops on the plant surface, and hence a combination of these factors can be used to fabricate superhydrophobic surfaces. There are various techniques reported in the literature to create superhydrophobic surfaces with different structures. Generally, most of these methods either start with preparing the rough surface by etching the surface followed by a surface hydrophobization treatment or using coating techniques to roughen the surface followed by hydrophobic coatings such as film or molecule deposition, self-assembly of hydrophobic layers, or solution coating. Here some recent development techniques are presented. An easy way to roughens glass, silicon, or metal surfaces is the plasma etching approach. The plasma etching method is an effective way to make the surface rough by polishing it to create micro or nano roughness in a single step. He et al. changed the hydrophilic silicon surface to superhydrophobic by altering the surface roughness and the chemical coating composition. They used reactive ion etching and catalyzed etching to prepare a superhydrophobic silicon surface with both micro- and nano dual-scale pillars. They found that the contact angle of water drops on silicon surfaces with nanopillars near to 150°, whereas the contact angle hysteresis remained less than 3° [57].

Another study was done by M. Lejeune et al. [58] to describe an efficient method to generate rough structures on silicon surfaces by using reactive etching of a photoresist layer. They used SF6 and CHF3 plasmas to generate the surface roughness on silicon surfaces for surface wettability modification. Due to the non-uniform removal of photoresist, the remains reside on the surface acts as a mask to generate roughness on the silicon surface. After the formation of the surface roughness, a CFx layer was deposited on the rough surface using plasma-enhanced chemical vapor deposition. The surfaces treated by the CHF3 plasma are all superhydrophobic up to 10 min of etching, whereas SF6 etching will not fabricate superhydrophobic after 2.5 min etching time. These results are due to differences in the Si etch rate with the two fluorocarbon gases. By increasing the etching time for SF6 to 5 min, the surface contact angle increased to 116°, which is approximately the contact angle on a flat surface for CFx coatings. Dorrer et al. also reported a method to control the superhydrophobicity or superhydrophilicity of a surface by manipulating the surface chemistry using different polymer coatings on Si nanograss surfaces fabricated by anisotropic plasma etching. They used a hydrophobic polymer poly(heptadecafluorodecylacrylate) (PFA) to coat Si nanograss surfaces, and they achieved contact angle as high as 179° with no observable hysteresis and very low solid-liquid fraction around $\phi = 10^{-4}$ [59].

Another widely used technique to generate surface roughness is lithography. Lithography is a technique to transfer structures from a mask onto a film or surface. In this approach, a photoactive polymer layer is irradiated by light through a featured mask followed by layer development where either the exposed or unexposed polymer is removed selectively, leaving a positive or negative image of the mask for the desired pattern on the surface. This technique can generate a very small, well-defined, and uniform structure. However, for industrial applications, surfaces need to be on a large scale, processed fast, and cheap, which limits the industrial applications of lithography. Bico et al. studied the effect of isotropic and anisotropic structures on superhydrophobicity by using lithography to generate some structures such as shallow cavities and stripes on Si surfaces. They observed that when deposited a small drop of water on such surfaces, the drops can look like a pearl with a contact angle close to 180° [60]. Shirtcliffe et al. also reported a lithography technique to produce a large area of high aspect-ratio patterns by using SU-8 as photoresist. The contact angle on the hydrophobized SU-8 pattern surface used here was around 155° with low solid-liquid fraction around ϕ = 0.19. The wettability of the pattern surface can be controlled by changing the pillar diameter, height, and the distance between the pillars [12]. Wang et al. [61] fabricated mushroom-shaped micro pillars mask using conventional lithography technique. Afterwards, PDMS of a good replication capability and low cost is used as a filling material to duplicate the structures from the template. Lee et al. [62] were able to achieve transparent and superamphiphobic surfaces from mushroom-like micropillar arrays by combining photolithography, replica molding, and self-assembly techniques. after that, they used O_2 plasma etching for 30 min to enhance the hydrophobicity of these surfaces. The advancing and receding contact angles after the etching process were 155° and 154°, respectively. Hu et al. [63] fabricated mushroom-shaped micropillars (MSMPs) using poly(methyl methacrylate) (PMMA) via electrohydrodynamic structuring technique. The MSMPs have a unique microscopic shape that is suitable to produce a highly robust nonwetting surface due to their specific overhang shape, which has a larger tip diameter than the shaft below. The measured apparent contact on the surfaces fabricated here was around 152°. A standard lithographic technique is also used to produce the master mold test structure of mushroom-shaped with overhanging caps. Subsequently, PDMS is used to duplicate the mushroom-shaped microstructure. Teflon is used as a chemical coating to enhance the surface superhydrophobicity. The advancing contact angles (CAs) of these microstructures were 166° ± 4.2°, 151° ± 2.9°, and 119° ± 2.2° when in contact with a water, ethylene, and olive oil droplet, respectively [64].

There are many more techniques previously reported to make the hydrophobic material rougher or to hydrophobized surfaces that already rough, such as sol–gel processing, layer-by-layer (LBL) and colloidal assembly, electrochemical reaction and deposition, electrospinning, and chemical (or physical) vapor deposition (CVD or PVD) [65]. These techniques were able to fabricate mostly two-dimensional (2D) patterns or only fabricate arbitrary structures unless using a higher expense mask with specific geometry or simple 3D structures [66, 67, 68]. Although some studies reported complex 3D structures, their process is quite complicated, time-consuming, and expensive [36, 69]. In recent years, additive manufacturing or as so-called 3D-printing technology has attracted much interest because it can not only produce 3D structures with well-defined geometries on both rigid and flexible substrates via a one-step process but can also be used for a wide variety of resin materials [22, 70]. Even though a few studies report that the 3D-printing technology is highly efficient in manufacturing SH surfaces [54, 55, 71, 72, 73, 74, 75, 76], there are still some challenges in the fabrication of resilient SH surfaces due to their short-term wetting stability or some additional complicated steps involved in the fabrication. Therefore, simple, more versatile, and commercial ways to manufacture 3D structured SH surfaces are still lacking and needs to be further studied, as the topic of the current thesis work presented in Chapter 4.

1.3 Sessile Droplet Evaporation on Superhydrophobic Surfaces

To date, many experimental and theoretical studies investigated the wetting and evaporation characteristics of droplets on surfaces with robust superhydrophobic features, so that surfaces always maintain high contact angles values. Three modes of droplet evaporation on superhydrophobic surfaces have been observed: a constant contact radius (CCR) mode, a constant contact angle (CCA) mode, and a mixed-mode [13, 14, 77, 78, 79, 80]. In the CCR mode, the contact line remains pinned while the contact angle reduces, whereas, in the

CCA mode, the contact angle remains fixed as the contact line recedes. The droplet contact radius and contact angle decrease simultaneously in the mixed mode. During droplet evaporation, droplets deposited on superhydrophobic surfaces may not be able to sustain their non-wetting Cassie-Baxter state, and transition to a Wenzel state may occur, which in turn leads to loss of superhydrophobicity of such surfaces. This evaporation process can trigger Cassie to Wenzel transition, due to a decrease in droplet size and the corresponding increase of the internal pressure [13, 81, 82]. The surface structure has also been reported to influence the stability of superhydrophobic surfaces. It has been debated that; a surface structure composed of a compact arrangement of pillars with higher aspect ratios is more likely to sustain its water repellent properties [14]. Experiments on wetting and evaporation are conducted on superhydrophobic surfaces with microscale surface structures that are usually concerned with a loss of SH properties during evaporation [13, 14]. However, using a finer scale, such as nanoscale features, may be beneficial in delay such transition. Due to the fabrication techniques and device limitations, experimental researches on SH surfaces with regular and random nanoscale surface roughness are still rare. Recent studies have revealed that the droplet evaporation rate on superhydrophobic surfaces was reported to be reduced due to the influence of the evaporative cooling effect at the droplet interface [83, 84, 85]. In this regard, the effect of the nano-structured SH on the wetting properties and the evaporation rates of water droplets needs to be studied through carefully designed experiments, presented in Chapter 2 of this thesis.

1.4 Surfactant Solutions

Amphiphilic surfactants or as so-called surface-active agents are molecules that tend to reduce the interfacial tension at the interface [86, 87, 88, 89, 90, 91, 92]. Surfactant generally consists of two distinct regions: a nonpolar hydrophobic tail, which avoids contact with water molecules and a polar hydrophilic head group with an affinity towards water via hydrogen bonding, dipole-dipole interaction or ion-dipole interaction [93, 94]. The hydrophobic tail is composed of a hydrocarbon chain that can be linear, cyclic, or branched [93, 94, 95, 96].

Due to the coexistence of both hydrophilic polar head and nonpolar hydrophobic tail on the same molecule, the surfactant can adsorb at the solid-liquid or liquid-vapor interfaces and form self-organized structures. Generally, surfactants are classified into four main types according to the charge of the polar hydrophilic head group: anionic, cationic, non-ionic, and zwitterionic surfactants [97, 98].

1.4.1 Anionic surfactants

Anionic surfactants can be divided according to their polar hydrophilic head group into carboxylates, sulfates, sulphonates, and phosphates [97, 98]. The most commonly produced anionic surfactants are linear alkylbenzene sulphonates, alkyl ethoxy sulphates, and alkyl sulphates. Examples of common anionic surfactants are sodium dodecyl sulphate (SDS), sodium dodecylbenzene sulphonate, and sodium laureth sulphate [88, 89, 91].

1.4.2 Cationic surfactants

The hydrophilic group in the cationic surfactants carries a positive charge. The most common cationic surfactants used are long-chain amines or quaternary ammonium salts. Halides or sulphates are used as counterions, while amine-based surfactants must be in a protonated state to function, so they cannot be used in alkaline conditions [97, 98]. Cationic surfactants can be mixed with water and with non-ionic and zwitterionic surfactants, except anionic surfactants. Many of the applications of cationic surfactants are based on the adsorption of the surfactant at solid surfaces because many natural and synthetic surfaces are negatively charged, such as antistatic agents in hair conditioners, softening agents in fabric softeners, corrosion inhibitors, and anticaking agents in fertilizers. Examples of cationic surfactants, dodecyltrimethylammonium bromide (DDAB), dipalmitoylethyl dimonium chloride, ethyl lauroyl arginate hydrochloride, and didecyldimethylammonium chloride (DDAC) [99, 100].

1.4.3 Non-ionic surfactants

The polar hydrophilic head group in the non-ionic surfactants can be either an uncharged polyethyleneoxide or polyhydroxyl chain. The most common advantages of non-ionic surfactants are the compatibility with all other types of surfactants, water, and electrolytes. Non-ionic surfactants are used as emulsifiers, wetting agents, and dispersing agents, e.g., in cleaning products, laundry detergents, cosmetics, paints, and paper products [97, 98]. Common examples of non-ionic surfactants are Tween 20, Triton X-100, and Brij 58 [93, 94, 95, 96].

1.4.4 Zwitterionic surfactants

Zwitterionic surfactants are electrically neutral because their hydrophilic head groups have both a positive and a negative charge. Most of the zwitterionic surfactants are pH-sensitive, which means they change the state of ionization with change pH values. Therefore, they are very mild to the skin and eyes and thus can be used in shampoos, cosmetics, and fabric softeners. Zwitterionic surfactants can show either anionic or cationic surfactant features depend on the solution type. In alkaline solution, pH-sensitive zwitterionic show features of anionic surfactants and acidic solutions features of cationic surfactants. Like non-ionic, zwitterionic can also be mixed together with all other types of surfactants. Examples of common zwitterionic surfactants are l auryl hydroxysultaine and sodium lauroamphoacetate [97, 98].

Surface active agents are omnipresent in many fundamental and industrial applications, such as mixing immiscible liquids, e.g., water and oil, forming an emulsion, for dispersing nanoparticles in a base fluid, to tune the wetting and spreading of the working fluids, or in microfluidic devices to control the coalescence of emulsion droplets [101, 102, 103, 104, 105]. Wetting and spreading of pure liquids on SH surfaces have been extensively reported in the literature [13, 14, 35, 37, 44, 48, 49, 56, 106, 107, 108]. Amphiphilic aqueous surfactant solutions, on the other hand, were investigated to a less extent and there are only few experimental studies reported CB-W transition of surfactant drops on SH surfaces [86, 89, 93, 94, 95, 96]. What's more, theoretical models regarding the prediction of the stability and the probability of surfactant concentration-dependent CB and W wetting states are still lacking, and hence the full understanding is still missing. Therefore, this motivates a part of the thesis work, presented in Chapter 3.

1.5 Overview of the thesis

The primary objective of this thesis is to use a facile, simple and non-expensive fabrication techniques to obtain superhydrophobic surfaces of different geometrical parameters and roughnesses and to give a better understanding of the wetting and evaporation dynamics of pure water and surfactant-laden droplets on these surfaces. The first work toward this objective was the experimental study of wetting and evaporation dynamics of pure water drops (in terms of the contact angle, base diameter, droplet height, and droplet volume) on nanograss superhydrophobic surfaces with extremely low solid-liquid fraction, reported in Chapter 2 to understand the effect of the nanograss structure on both droplet wetting and evaporation dynamics.

In addition to the pure water, we next investigate the effect of cationic surfactant (DDAB) of different initial concentrations on droplet wetting upon microstructured superhydrophobic surfaces of various geometrical parameters and surface roughnesses. Here, the effect of DDAB surfactant concentration on the wetting state is studied through the static and dynamic contact angle measurements via side-view snapshots of droplets and through the bottom-view snapshots for the wetting state analysis, discussed in Chapter 3.

Since most of the previously reported fabrication techniques to obtain superhydrophobic surfaces were sophisticated, time-consuming, and costly expensive, we report facile, simple, and cheap one and two-step processes to prepare transparent super-repellent and superhydrophobic surfaces of different roughness levels, reported in details in Chapter 4.

Chapter 2

Evaporation Dynamics of Water Droplets on Superhydrophobic Nanograss Surfaces[1]

2.1 Introduction

Droplet evaporation is an omnipresent process that also finds plentiful decisive applications, including watercolor painting [1], droplet-based microfluidics [2], DNA extraction [3], inkjet printing [4, 5, 6], and fabrications of bio-materials and photonic crystals through self-assembly [6, 109, 110]. Therefore, fundamental understating of droplet evaporation dynamics under various key parameters, such as surface structure or roughness [14, 111], nano-particle suspensions [112], and surface wettability [113] is crucial so as to control the processes tailored for the desired applications. In particular, evaporating droplets on superhydrophobic (SH) surfaces has recently received a significant interest because of their promising applications for self-cleaning [37, 107, 108], improving corrosion resistance [35], optical devices [38, 114, 115], anti-icing [44, 56], anti-fouling [106], and friction control [47, 48, 49]. SH sur-

---

[1] The material presented in this chapter is based on Aldhaleai, A., Khan, F., Thundat, T., and Tsai, P.A., "Evaporation Dynamics of Water Droplets on Superhydrophobic Nanograss Surfaces", under revision, International Journal of Heat and Mass Transfer, 2020.

faces are commonly characterized by a large contact angle ($\theta \gtrsim 150\,^{\circ}$) with water and small contact angle hysteresis (CAH), the difference between advancing and receding contact angles [11]. Deposition of water droplets on SH surfaces relies on the interplay between surface chemistry and roughness, while two common wetting modes are observed: (i) Cassie-Baxter wetting (CB or the so-called Fakir) with air (or vapor) trapped under-beneath the droplet [9, 11, 116] and (ii) Wenzel (W) regime where the liquid fills in the surface cavities [8]. Albeit various beneficial applications, it has remained challenging to use superhydrophobic surfaces for long-term stability since most of them lose their liquid-repellency once exposed to chemical [117], high temperature environments [118, 119] or surfactant additives [40]. Another factor that limits the commercial use of the SH surfaces is the occurrence of the irreversible wetting transition from Cassie-Baxter to Wenzel state during evaporation [11, 13, 14, 79, 120, 121, 122, 123], thereby destroying the superhydrophobicity of a low CAH and air-trapping state.

Both static wetting (in terms of static contact angle) and water evaporation dynamics on SH micro-textures, e.g., regular micro-pillars [3, 14, 79, 124, 125, 126, 127, 128, 129], random micro-fibers [107, 117, 118], or micrometer-sized mushroom-shaped pillars [80, 130], have been actively studied over the last two decades. Whereas, in comparison, fewer studies have been conducted on SH nano-scale structures or fibers [14, 35, 37, 40, 56, 111, 114, 118, 131] primarily due to challenges of nano-fabrications. Besides the packing fraction, ϕ, the length scale of surface roughness can play a crucial role in the pinning (or retention) and de-pinning forces exerted on droplets by solid surfaces/textures [129], thereby affecting contact line movement and evaporation modes of water droplets on various SH surfaces. The evaporation dynamics and dynamic wetting on superhydrophobic nano-textured surfaces (e.g., SH nanograss-liked surfaces), however, were investigated to a less extent [59, 132, 133, 134]. In particular, experiments regarding the contact line movement of evaporating drops on SH nanograss surfaces (with pointy or needle-liked contact areas) are rare, and hence the full understanding is still missing. Further investigations are hence needed to shed light on the roughness effect on evaporation modes and rates as well as contact line movement on

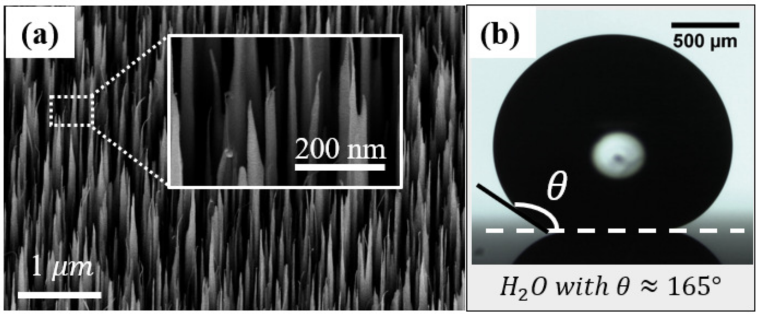

Figure 2.1. (a) SEM image of superhydrophobic nanograss (NS) surface with random nanoscale structure; (b) the corresponding side-view snapshot showing a large contact angle ($\theta \approx 165°$) of water droplet.

various SH surfaces.

In this work, we fabricated SH nanograss-liked surfaces and investigated the initial wetting state, evaporating dynamics, and contact line movement of a naturally-evaporating water droplet on such SH surfaces of random nano-scale roughness, with an extremely low solid packing fraction, $\phi = 0.05 \pm 0.01$, and surface roughness, $r = 1.05 \pm 0.01$ (see Fig. 2.1). Here, ϕ and r are conventionally defined as the ratio of the liquid-solid surface area to the total (liquid-solid and liquid-gas) areas and the ratio of the total surface area to the projected one (on a 2D plane), respectively, and estimated using a nanocone geometry (see Appendix A.1, for details). Systematic measurements of the droplet contact angle, base diameter, height, and volume were performed for several SH nanograss surfaces. Our results highlight the influences of nano-roughness and droplet size on the evaporation dynamics. By increasing the droplet size, for the first time, stick-slip motions of the contact line for large droplets on SH nanograss surfaces were studied.

2.2 Experimental

2.2.1 Sample preparation

Several SH nanograss surfaces were fabricated using reactive ion etching (RIE) on 4-inch wafers, cleaned using a standard piranha solution in prior. Fig. 2.1a shows a side-view, SEM image of such SH surface used. The formation of nanograss is a result of the passivation and etching process in a standard RIE etching process. The RIE etching is performed using a mixture of H_2 and O_2 gases with a flow rate of 100 standard cubic centimeters per minute (sccm) and 80 sccm, respectively. Additionally, trace value of SF6 plasma is also supplied and used during the etching process. The etching and passivation steps are performed at a pressure of 80 mTorr and 150 mTorr, respectively. During RIE, plasma power is adjusted between 150W and 135W for the steps of passivation (for 52 s) and etching (for 12 s), respectively. After the nanograss formation, the wafer is coated with photoresist, which provided protection during the subsequent step of dicing. After dicing, each 1 cm × 1 cm piece is soaked in acetone overnight; this step helps in removing photoresist completely.

2.2.2 Droplet evaporation experiments

For the evaporation experiments, water droplets of 10-μL are gently deposited on the NG surface using a syringe pump. One camera (Thorlabs DCC3240C) coupled with a long-range magnifying lens (Navitor 12×) was used to record side-view of the evaporating droplet at 1 fps (frame per second). Fig. 2.1b is such a snapshot showing the initial wetting state of Cassie-Baxter state [11], while air is trapped beneath, and the drop rests on the top of the nanograss with a large contact angle, $\theta > 160°$.

To analyze the evaporation dynamics, we first extracted the shape of droplets from the side-view snapshots using ImageJ software [135]. Subsequently, a Matlab code based on the axisymmetric drop shape analysis (ADSA) method was applied to measure the drop volume (V), contact angle (θ), droplet height (h), and the drop size. The ADSA method numerically fits a theoretical Laplacian curve based on the Young–Laplace equation with the gravitational effect with known surface tension values to an experimental profile of the drop shape obtained [136, 137, 138]. The experiments were performed under ambient temperature (22 ± 1°C) at 1 atm and slightly varying relative humidity (RH) conditions.

2.3 Results and Discussion

2.3.1 Evaporation dynamics

Fig. 2.2 illustrates the evaporation dynamics of water droplets on SH nanograss (NG) surface in terms of dimensionless time (t/t_f) normalized by the total evaporation time (t_f), under slightly different RH $\approx 24.8 \pm 1.2\%$. Fig. 2.2 shows that the droplet on the SH NG surfaces began with a large $\theta \approx 166^\circ \pm 1.5^\circ$ in a CCA mode, in agreement with a CCA-mode evaporation observed on SH surfaces with nano-roughness and a low CAH $\approx 5^\circ$ by Kulinich et al. [139]. In comparison, previous data of the evaporation dynamics on SH nano-structured (NS) pillars [14] started with a CCR mode, subsequently followed by a CCA mode, and ended the evaporation with a mixed mode. Remarkably, all the water droplets on SH NG surfaces were in a CB state, whereas the droplets on SH nanostructured pillars can form a CB droplet for high roughness $r > 3.51$ and a Wenzel droplet for relatively low $r < 1.98$ [14], as shown in Fig. 2.2 a-b. As revealed in Fig. 2.2b, for SH nanograss surfaces we observed that for small water droplets (of initial diameter $D_0 \approx 2.6 \pm 0.17$ mm) the contact diameter (D_b) decreases linearly with the dimensionless time from 0 to 90% t_f at a slope of $\approx$ -1 ± 0.2, implying a very mobile contact line without pinning on SH NG surfaces. This corresponds to the linearly decreasing of D_b/D_0 with a decaying slop of $\beta = -0.39 \pm 0.04$, obtained with a best linear-fit in Fig. 2.2b, because of simultaneous decreasing H and V during evaporation (shown in Fig. 2.2 c-d). Fig. 2.2c reveals that the droplet volume changes non-linearly with time, consistent with the evaporation characteristics on SH carbon nanofibers (CNF) [77] with a random structure and large initial $\theta \approx 150^\circ$. However, the evaporation mode observed on such SH CNFs of random roughness is CCR [77], different from the CCA initially observed by our SH Nanograss surface. In comparison, recent studies on SH nanoporous membrane made of hydrophobized anodic aluminum oxide (AAO) show a CCR mode of evaporating droplets, with a pinned contact line, during most of evaporation time [78]. The authors discussed that evaporating water droplets stick on such surfaces, very likely, because of air entrapped in the nanoscale pores that are not interconnecting [78]. These comparisons

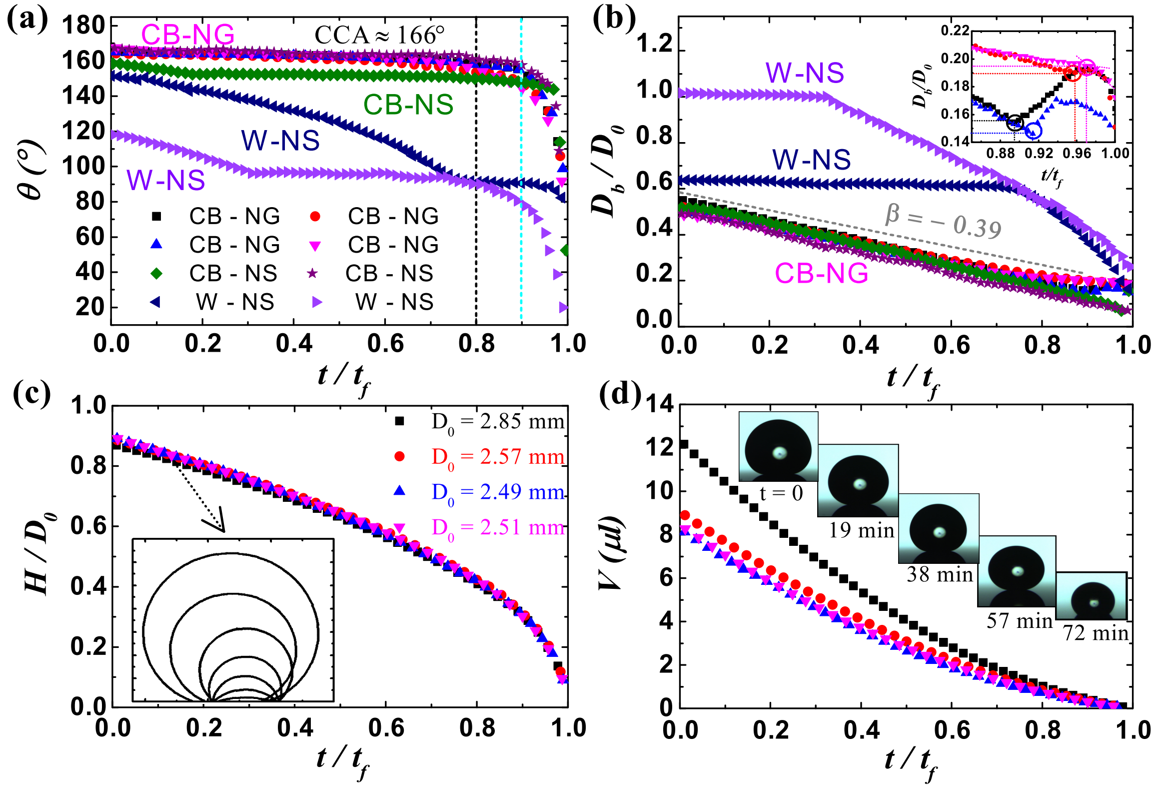

Figure 2.2. Time-evolution of (a) contact angle, θ, (b) dimensionless base diameter, D_b/D_0 of evaporating water droplets on the SH nanograss (NG) surfaces (shown in Fig. 2.2a) (■, •, ▲, ▼). Here, time, t, is normalized with the total evaporation time, t_f. The length scale is normalized with, D_0, the free drop diameter of the same initial volume. Initially, for $t/t_f = 0 - 0.8$, the drop evaporates with a constant contact angle (CCA) mode with average $\theta \approx 166°$, while the dimensionless contact diameter, D_b/D_0, decreases linearly with dimensionless time with a decaying slope of $\beta = -0.39$. At the end of the evaporation (for t/t_f between 0.8 and 1), both D_b and θ decrease, corresponding to a mixed mode. The inset in (b) reveals a slight increase in D_b after $\approx 0.9t_f$ as the droplet underwent a CB to Wenzel (W) transition while water impregnating into the rough cavities. For a comparison, the previous experimental data by Bussonniére et al. [14] using more regular, nanostructures (NS) are also plotted (♦, ★, ◂, ▸) for θ and D_b in (a) and (b), respectively. Depicted in (c) is the dimensionless droplets, H/D_0, for four independent droplets. The inset shows the contours for an evaporating droplet with $D_0 = 2.85$ mm. Time-varying droplet volume, V, is shown in (d), and the insets show the time evolution of droplet shape for $V_0 = 12$ μl.

highlight that both ϕ and the shape or morphology of nano-textures or nano-roughness play an important role in the pinning of contact line and, hence, initial evaporation mode, being CCR or CCA.

Once the evaporation time reaches $0.9t_f$, the transition from partially-wetting CB to

Wenzel state occurs at a critical contact angle, ranging from 114° to 155.6° and critical base diameter, $D_b = 450 \pm 60$ μm, where the contact diameter underwent a slight increase shown by the Fig. 2.2b inset. We estimated that the Laplace pressure inside the droplet increased during the process from its initial value, $\Delta P_L = 111.4 \pm 6.8$ Pa to the critical Laplace pressure, ΔP_L^*, ranging from 305.4 Pa to 591.4 Pa (estimated from four independent experiments). The value of Laplace pressure is calculated using the drop radius of curvature (see Appendix A.2 for the details). Such CB to W transition could be triggered by the decrease in the droplet size so that the Laplace pressure increase inside the droplet from its initial value to the critical Laplace pressure. We identified such CB-W transition by an increase in D_b since water penetrates nano-rough structures and thus enlarges the contact diameter. This method agrees with and is also used by a recent study on drops evaporating on pillar-like microtextured SH surfaces [123]. The corresponding critical contact angles, contact diameters, and Laplace pressure are reported in Appendix A.2.

Water droplets on our SH NG surfaces were in a CB state with a large CA ($\theta > 160°$) and evaporated mostly in CCA mode, followed by a mixed mode. During final evaporation $t > 0.9\, t_f$, both θ and D_b decrease simultaneously, in a so-called mixed mode, until completely dry out [79]. A CCA mode followed by a final mixed mode on SH surfaces with a small CAH has also been observed during evaporation on SH micro-patterned surfaces and random nanostructure with low $\phi \lesssim 0.04$ [59, 79, 123]. In comparison, whereas for SH nano- and microstructured surfaces with a higher ϕ [79, 80], three sequential stages of evaporation dynamics of (i) CCR, (ii) CCA, and (iii) mixed mode (of CCR and CCA) were reported. Combing with our data on SH NG surfaces, the above comparisons between various experimental data reveal that, despite different types of surface morphology, water droplets on various superhydrophobic surfaces of small packing fraction ϕ and a low CAH evaporate in a CCA mode initially. On the other hand, regardless of micro or nano-sized roughness, droplets evaporate in a CCR mode initially on SH surfaces with a large CAH.

2.3.2 Stick-Slip motion for large droplets

In contrast to smoothly decreasing in D_b for the small droplets (of $D_0 \approx 2.6$ mm) shown in Fig. 2.2, stick-slip motions of the contact line were observed during the evaporation of relatively large droplets (of $D_0 \approx 4.2 \pm 0.2$ mm) deposited carefully. Fig. 2.3 a-b shows such (jumping) results of the contact angle and diameter evolution of large evaporating droplets on SH NG surfaces, for initial air-trapping CB state for different droplets with different RH between 21% and 52%. Two distinct initial modes of evaporation were observed when depositing large water droplets $D_0 \geqslant 4$ mm on SH NG surfaces. First set of data (■,◂) in Fig. 2.3 a have slightly different free drop diameter $D_0 \approx 4.04$ and 4.43 mm, respectively, and started initially at CCA mode similar to small droplets, while D_b recedes steeply. On the other hand, the other data for $D_0 \approx 4.13$ mm (●) and 4.08 mm (▲) underwent a mixed mode (of CCR and CCA) evaporation with very slowly decreasing D_b and θ. When t/t_f between 0.9 and 1, mixed mode occurs, while both θ and D_b diminishes simultaneously.

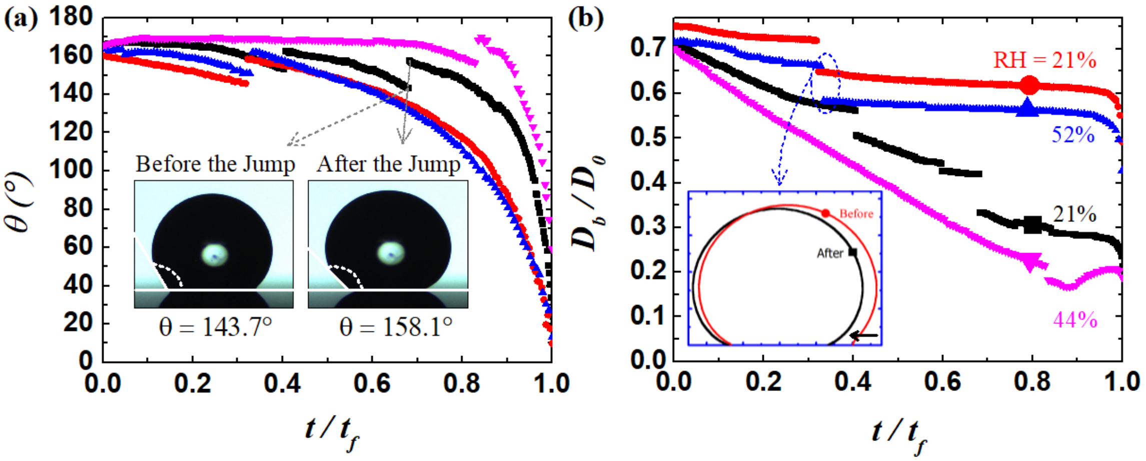

Figure 2.3. (a) Contact angle, θ, and (b) the normalized contact diameter, D_b/D_0, as a function of the normalized time, t/t_f, measured for water droplets of $D_0 \approx 4.2$ mm at various relative humidity (RH). In (a) and (b), stick-slip motions are observed for large droplets, and the insets show the droplet shape before and after the jump in changing θ. This trend repeated for the all stick-slip/jump events observed for various large droplets of $D_0 = 4.04$ (■), 4.13 (●), 4.08 (▲), and 4.43 (◂) mm.

Experimentally, we observe that water drop has a certain initial contact angle, θ_0, after the deposition of the droplet. Water droplet starts to lose liquid during evaporation, resulting in a deviation from that of the initial equilibrium state due to the changes in droplet shape and CA, causing the triple line to move [140]. When θ_0 reaches a minimum possible value below or equal the receding contact angle, $\theta_r \approx 156.9° \pm 1.2°$, which is measured by using a sessile drop method while reducing the droplet volume on the surface. Subsequently, the contact line starts to move, and the first jump is observed. The advancing contact angle for the SH NG surfaces is also measured, $\theta_a \approx 164.5° \pm 0.6°$, with the sessile drop method by slowly increasing the droplet volume. With the average θ_a and θ_r measured, one can estimate the magnitude of the adhesion force, F_{adh}, between the water droplet and SH NG surface, via $F_{adh} = C_g R_b \gamma(\cos\theta_r - \cos\theta_a)$ [10, 141], where C_g is a geometric prefactor depending on the shape of the drop base on the solid surface ($C_g = 4/\pi$ for a circular contact, e.g., Eq. (10) in Ref. [141]), and R_b is the base radius of the droplet. Based on the equation, our estimates of the droplet adhesion forces on the SH NG surfaces are ≈ 3 and $6\ \mu N$ for the small and large water droplets used, respectively. The order of magnitude of these adhesion forces calculated is consistent with (but smaller than) previous estimations using micro-pillared SH surfaces [142].

The stick-slip motion is revealed by a sudden decrease of D_b and an abrupt increase in θ, indicated by the sudden movement of the three-phase contact line occurring for all the large droplets. Fig. 2.3a insets, for example, display a water droplet of $D_0 = 4.43$ mm before and after the slip or jump motion, with their θ changing from 156° to 168° (which recovers to nearly its initial value of $\theta_0 \pm 3°$) and D_b from 0.96 mm to 0.82 mm.

This jumping motion is very likely attributed to the excess free energy available due to the reduction in the droplet size and θ [143]. Using the thermodynamic Gibbs free energy of the drop due entirely to interfacial free energies, Shanahan [140] proposed a theoretical model estimating certain excess energy as a criterion for contact line movement. The excess free energy per unit length is associated with the contact line movement by δr, resulting in the change in θ on smooth or rough surfaces, and can be expressed as [140]:

$$\delta\tilde{G} \approx \frac{\gamma \sin^2\theta_0 (2 + \cos\theta_0)(\delta r)^2}{2r}, \tag{2.1}$$

where γ is the surface tension at the liquid-air interface, θ_0 is the initial equilibrium contact angle of the surface, δr is the slipped distance local to the stick-slip event, and r is local pinned contact radius before the triple line slips. As evaporation proceeds, the slipped distance, δr, the distance between the actual contact radius, r, and the corresponding equilibrium value, r_o, increases, and hence $\delta\tilde{G}$ increases with $(\delta r)^2$. When $\delta\tilde{G}$ reaches the potential energy barrier value, sufficient energy is available, causing the triple line to jump to its new equilibrium position at a lower contact radius. While CA after the jump recovers nearly to the initial θ_0, as shown in Fig. 2.3a.

To calculate the excess free energy, we measured θ_0, δr, and r during each slip events using eq. (2.1) (see Appendix A.3 for the values). The average jumping distance, δr, on our SH NG surfaces is 132 ± 40 μm, contrastingly compared to that of approximately the micro-pillar spacing of $O(10\ \mu\text{m})$ for evaporating droplets stick and slip on SH regular micro-pillars [124, 127]. Intriguingly, the latter indicates that the origin of the stick-slip motion of contact line stems from the pinning and de-pinning forces exerted by the individual (regular) pillars where water droplet sticks upon, which is consistent with the results reported for periodic nano-pillars by Molecular Dynamics (MD) simulation [129]. In contrast, for our SH NG surfaces due to needle-liked structures, large water droplets can slip with a much greater δr. The average value of $\delta\tilde{G}$ calculated for the large droplets on SH NG surfaces is about 10^{-8} J m^{-1}. This value is one order of magnitude less than that reported by Shanahan and Sefiane on randomly rough PTFE substrates [144], and in the same order of magnitude of those reported by Ramos on microstructured PTFE surfaces [145]. The low values for $\delta\tilde{G}$ on microstructured PTFE and our SH NG surfaces can be attributed to the robust superhydrophobicity of their and our substrates. In a CB state, the small solid-liquid contact area, resulting in a high contact angle, can decrease $\delta\tilde{G}$ values.

2.3.3 Evaporation rate

The classical theory of the vapor-diffusion model is widely used to predict the evaporation mass flux across the vapor-liquid interface of an evaporating droplet [146]. In this model, Popov assumed that the vapor transport by free convection, induced by the density difference between dry and humid air, is negligible compared to diffusive transport. The influence of the evaporative cooling of the droplet on the evaporation rate is also neglected. Hence, the vapor transport occurs mainly by diffusive spreading of the water vapor in air. To determine the diffusive out mass flux from the drop surface, the change in the vapor concentration field around the droplet, $\Delta c = c_s - c_\infty$, has to be calculated. Here, c_s is the saturated vapor concentration at the surface and c_∞ is the vapor concentration away from the droplet. To formulate the problem, a cylindrical coordinate system (r,z,Φ) is used, with r being the radial coordinate, z the normal direction to the substrate, and Φ the azimuthal angle coordinate. The origin of this system is chosen such that $z = 0$ corresponds to the substrate and $r = 0$ to the center of the droplet. In this case, the problem is axisymmetric, that is, Φ-independent. The boundary conditions imposed along the spherical-cap droplet with arbitrary contact angle θ are (i) $c = c_s$, the saturated vapor concentration, along the droplet surface; (ii) $c = c_\infty$, the ambient vapor concentration, far away from the drop; and (iii) the substrate is impermeable, hence $\partial c/\partial z = 0$ along the substrate. The diffusive flux is given by $J = -D\nabla c$. Popov used analytical solution to determine the rate of mass loss from a droplet of arbitrary contact angle, and we provided these equations in Appendix A.4.

This model was able to predict the evaporation rate for some experimental studies conducted in ambient air on carbon nanofiber (CNF) [77], smooth hydrophobized silicon wafers, and rough hydrophobic Teflon [147]. The simplification ingrained in the model such as assuming that vapor-diffusion is the only transport mechanism governing the droplet evaporation without considering the evaporative cooling may limit its applications to other experimental data, and it has been shown to either underpredict [148, 149] or overpredict [83, 84, 85] the evaporation rate.

Here, we compare the experimental dimensionless mass flux rate, $\dot{M} = \frac{\dot{m}}{R_b D(c_s - c_\infty)}$, in Fig. 2.4 using water droplets on SH NG surface, where R_b is the base radius, D is the water vapor diffusion coefficient in air, c_S is the saturated vapor concentration, and c_∞ is the vapor concentration far away from the droplet, with the analytical vapor-diffusion model (dashed line) [146] and with a numerical simulation (solid line) considering cooling effect

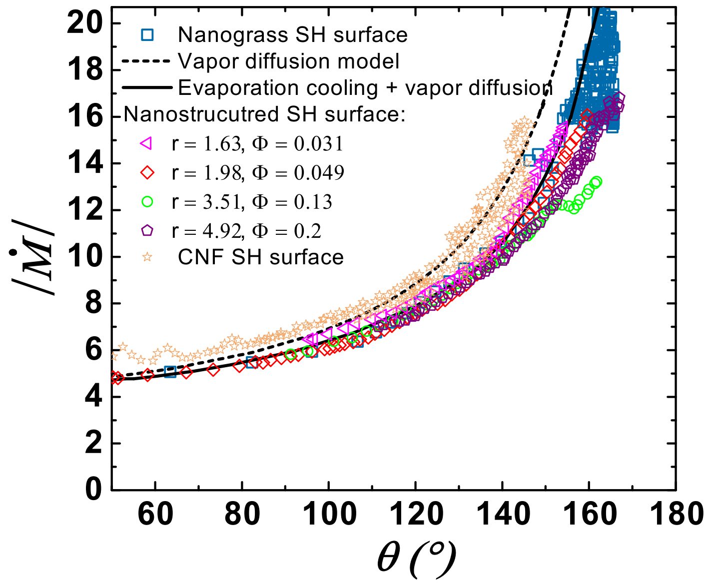

Figure 2.4. Water evaporation rate on SH nanograss surface. The dimensionless evaporation mass flux rate, $|\dot{M}|$ (measured from the measured droplet volume) as a function of CA (θ) for different droplets. Comparison between our experimental results (□) with a vapor diffusion model derived by Popov [146] (- - - -) and an evaporation cooling model [85] (——) displayed that the low evaporation rate observed can be attributed to a cooling effect. For a comparison, the previous experimental data by Bussonniére et al. [14] (◁,◊,○, ⬠) using SH NS and Gelderblom et al. [77] (☆) using SH carbon nanofiber (CNF) are also plotted.

[85]. The direct form of the Popov model concludes that the rate of mass loss only depends on the contact angle but slightly overestimates the evaporation rates measured on our SH NG surfaces.

Our data is in agreement with the recent studies by Bussonniére et al. [14] and Dash et al. [125], revealing that droplets evaporate more slowly on SH nano-patterned surfaces. Further numerical simulation [85] suggested that this deviation is likely attributed to the evaporative cooling effect. At a high contact angle, the contact diameter becomes small, limiting the heat flux between the substrate and drop, which in turn leads to a decrease of saturated vapor concentration, and hence slower evaporation. Our data reveal a better agreement with the numerical simulation considering a cooling effect during evaporation [85], and with the results using SH nano-structured surfaces [14]. At high CA, more than ≈ 150°, the experimental data deviate from the cooling model (Solid line in Fig. 2.4) with a lower rate. This deviation may attribute to the spherical droplet assumption used in both models and the observed perversion of the drop shape at such a high CA from a spherical cap [85, 146].

2.4 Conclusions

In summary, the wetting state, evaporation dynamics, and contact line movement of evaporating water droplets on SH nanograss surfaces with an extremely low $\phi \approx 5\%$ were experimentally elucidated. Different from that evaporating drops can form either CB or Wenzel state, depending on r and ϕ, on more regular SH micro- or nano-structured pillars, all small droplets on SH NG surfaces formed a gas-trapping CB wetting state and evaporated in a constant contact angle mode for most of the droplet lifetime. Besides, beneficial to various applications, the SH nanograss surfaces delay the CB to Wenzel Wetting transition to a later time at $0.9t_f$. In contrast to smaller drops, stick-slip motions of the contact line were observed for the first time, for large droplets of initial drop size of $D_0 \approx 4.2$ mm on SH nanograss surfaces. This jumping motion is attributed to the excess free energy (of $O(10^{-8} Jm^{-1})$) available in the system, due to the change in the droplet shape and contact angle, and hence the contact line movement when θ reaches θ_r. Finally, the classical vapor-diffusion model slightly overpredicts the water evaporation rate on SH nanograss surfaces with a low CAH and smaller contact area, while the evaporative cooling effect could better predict the evaporation rate. In terms of applications, using the superhydrophobic nanograss surfaces water droplets evaporate mostly in a constant-contact-angle mode, with a very mobile contact line, and delay the CB to W wetting transition (to 0.9 t_f), compared to the initial CCR mode and pinning contact line observed on most of SH regular micro-structures and nano-pillars. This suggests robust SH surfaces composed of nano-grass structures of a low ϕ ($\lesssim 0.05$) and a low CAH for advantageous, self-cleaning surfaces with water droplets.

Chapter 3

Effect of a Cationic Surfactant on Droplet Wetting on Superhydrophobic Surfaces[1]

3.1 Introduction

The wetting and spreading characteristics of pure liquids on solid surfaces is of significant interest in several engineering and industrial applications, including droplet-based microfluidics [104, 105], coating [38], inkjet or electrohydrodynamic jet printing [150], and membranes technology, especially for oil-water separation [54, 55]. In the past two decades, droplet wetting on low-energy surfaces, as so-called ultrahydrophobic or superhydrophobic (SH) surfaces with water contact angle (CA) ($\theta \geq 150°$) and small contact angle hysteresis (CAH), has received a great interest due to their promising applications for friction control, anti-icing, anti-fouling, self-cleaning, and improving corrosion resistance [35, 37, 44, 47, 48, 49, 56, 106, 107, 108]. Such surfaces are not only chemically hydrophobic but also physically rough, consisting of both micro/nano-scaled roughness or structures. These useful SH surfaces allow the drop to sit on the top of the surface textures with air trapped underneath

---

[1] The material presented in this chapter is based on Aldhaleai, A. and Tsai, P.A., "Effect of a Cationic Surfactant on Droplet Wetting on Superhydrophobic Surfaces", Langmuir, 36, 16, 4308-4316, 2020.

with a partial gas-liquid interface, as the so-called Cassie-Baxter (CB) or "Fakir" wetting state [9, 11].

The presence of a gas layer minimizes the interfacial energy, thereby making a CB state more favorable by reducing the contact area between the liquid and solid phases. However, the long-term stability of the preferred CB state on SH surfaces is still challenging and can be lost through an irreversible wetting transition to Wenzel (W) state, where the liquid fills in the surface cavities, when exposed to chemical [117], high temperature environment [118, 119], surfactant additives [40], or evaporation [13, 15]. To date, the wetting properties of SH surfaces have been extensively investigated, but mostly limited to pure liquids [11, 13, 14, 35, 37, 38, 44, 47, 48, 49, 56, 106, 107, 108, 151, 152, 153]. In contrast, amphiphilic aqueous surfactant solutions have been investigated to a less extent on SH surfaces, and there are only a handful experimental studies reported CB-W transition of surfactant-laden drops on SH surfaces [86, 87, 88, 89, 90, 91, 92, 93, 94, 95, 96].

In this work, we investigate experimentally and theoretically how a cationic surfactant and its concentration changes the contact angle (CA) and wetting state of a droplet on ultra-hydrophobic microstructures of different solid-fraction (ϕ) and surface roughness (r). Systematic measurements of both CA and wetting states were conducted for nine DDAB surfactant concentrations. We compare our experimental results with thermodynamic predictions that consider surfactant adsorption at interfaces to examine C_S-dependent CA. Using Gibbsian thermodynamic analysis, we also elucidate theoretically the probability and the stability of the experimentally observed CB state at low C_S.

3.2 Experimental

3.2.1 Sample Preparation and Materials

Transparent polydimethylsiloxane (PDMS) microstructured SH surfaces with a square array of parallel cylindrical pillars (of height $H = 4.8$ μm) were prepared using a replica modeling process [13]. Two pattern diameters (D) and pitches (P): $D = 4.9$ μm, $P = 7.5$ μm (surface

S1) and $D = 4.6\ \mu$m, $P = 14.5\ \mu$m (surface S2) were used to obtain different ϕ and r (see Fig.3.1). The packing fraction, $\phi = \frac{\pi D^2}{4P^2}$, is the ratio of the liquid-solid surface area (pillar-top area) to the total (liquid-solid and liquid-gas) areas, and surface roughness, $r = 1 + \frac{\pi DH}{P^2}$, is the ratio of the total surface area to the projected one (on a 2D plane). In other words, r describes the relative change in the liquid-solid area for a rough surface compared to a flat surface in a Wenzel state [8], while ϕ describes the percentage of the liquid–solid contact area in a Cassie–Baxter case [9].

The surfactant solutions were prepared by dissolving didodecyldimethylammonium bromide (DDAB) powders (Sigma-Aldrich, 98%, with a critical micelle concentration (CMC) of = 0.085 mM) in ultrapure Milli-Q water (PURELAB Ultra, resistivity: 18.2 MΩ.cm) for nine different normalized concentrations, $C_{\mathrm{S}} = C/\mathrm{CMC} = 0$, 0.02, 0.05, 0.1, 0.2, 0.25, 0.5, 0.75, and 1, where C is DDAB surfactant concentration, and C_{S} is the normalized surfactant concentration by the critical micelle concentration (CMC). All solutions were prepared in glass beakers that were first cleaned with acetone, subsequently with ethanol, and finally rinsed thoroughly with Milli-Q water.

3.2.2 Wetting Experiments

For each surfactant concentration, ten drops were gently deposited using a 10 μl micropipette on each freshly made microstructured SH and flat PDMS surfaces. Two synchronized cameras were used to record the side and bottom views of the droplets upon deposition at 1 fps (frame per second). The side-view was recorded using a CCD camera (Thorlabs DCC3240C) coupled with a long-range magnifying lens (Navitor 12×) and the bottom-view using a color camera (Axiocam 105) integrated into an inverted microscope (Zeiss, with a 5× objective). To measure the contact angles, we first extracted the shape of droplets from the side-view snapshots for the first and last 10 s of a 100 s acquisition period using ImageJ software [135]. Subsequently, a Matlab code based on axisymmetric drop shape analysis (ADSA) method was applied to measure the contact angle (θ) [14, 136, 137, 138]. Advancing and receding contact angles were also measured using the sessile drop method

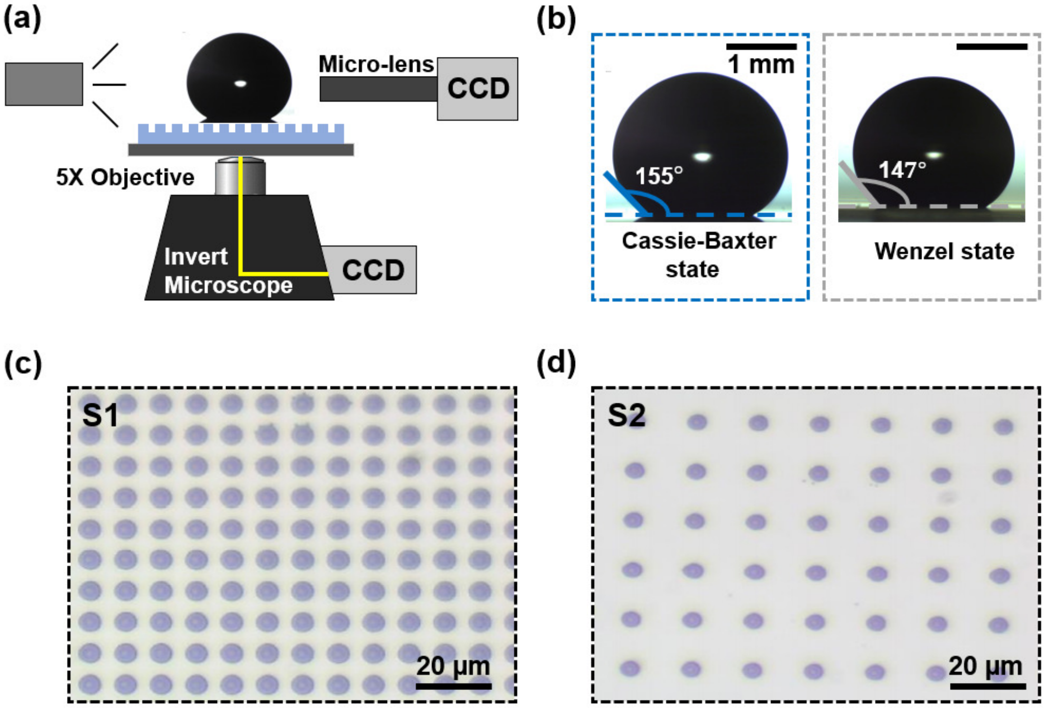

Figure 3.1. Schematic of the experimental setup in (a). (b) Different initial wetting states: side-view of a DDAB-laden droplets of $C_{\mathrm{S}} = 0.1$ resting on a SH surface of $r = 1.33$, $\phi = 0.08$ (S2) in a CB state and in a W state, respectively. (c-d) Microscopic images of the two types of superhydrophobic microstructures used, with a square pillar pattern with a pillar diameter (D) and pitch (P), first, $r = 2.31$, $\phi = 0.34$ (for the SH S1 surface) in (c), and second, $r = 1.33$, $\phi = 0.08$ (for the SH S2 surface) in (d), respectively.

by slowly increasing and decreasing the droplet volume on the surface, respectively. Drop wetting states were determined through the bottom-view snapshots (see Fig. 3.2). All experiments were performed under ambient temperature (24 °C) at 1 atm and relative humidity of 29 ± 3%.

3.3 Theoretical

3.3.1 Contact angle models

To investigate the dependence of CAs and wetting states on the normalized cationic surfactant concentration, C_{S}, we follow a thermodynamic model proposed by Milne et al.[154] studying SDS-surfactant drop (on a Teflon SH surface). This theory combines the Gibbs adsorption equation, Young's, Cassie-Baxter, and Wenzel equations with adsorption isotherm to explain the effect of surfactant adsorption at each interface, which subsequently will influence the thermodynamic CAs. Firstly, the Gibbs adsorption describes the differential change in surface energy with a differential change in a surfactant concentration (C_{S}) in the aqueous solution:

$$d\gamma_{\mathrm{xy}} = -\Gamma_{\mathrm{xy}}\mathcal{R}Td\ \ln\ (C_{\mathrm{S}}), \tag{3.1}$$

where γ_{xy} is the interfacial tension, Γ_{xy} is the surface coverage per unit area of surfactant at the interface xy (x and y represent a liquid (L) solid (S), or vapor (V) phase), $\mathcal{R}$ is the universal gas constant, T is the absolute temperature, and C_{S} is the non-dimensional surfactant concentration.

To compute Γ_{xy}, we use general isotherm equation proposed by Zhu-Gu [155] including Langmuir-type (L), S-type (S) and two plateaux- type (LS) adsorption isotherms. This general isotherm can be applied to liquid-vapor (LV), solid-liquid (SL), and solid-vapor (SV) interfaces, but here we assume no adsorption at the solid–vapor interface (i.e., $\Gamma_{\mathrm{SV}} = 0$). The adsorption isotherm, Γ_{xy}, is:

$$\Gamma_{xy} = \Gamma_{xy}^{\infty}\frac{K_{xy}C_{\mathrm{S}}^{n_{xy}}}{1 + K_{xy}C_{\mathrm{S}}^{n_{xy}}}, \tag{3.2}$$

where Γ_{xy}^{∞} is the maximum surfactant concentration at the interface, K_{xy} is the equilibrium constant for adsorption, and n_{xy} is known as an empirical fitting parameter in the Zhu–Gu [155] adsorption isotherm.

By coupling the Gibbs adsorption equation (eq. (3.1)) with Zhu-Gu [155] adsorption isotherm (eq.(3.2)) and integrating at the LV interface, one obtains an expression for LV interfacial tension γ_{LV} as a function of surfactant concentration, C_{S}:

$$\gamma_{\mathrm{LV}}(C_{\mathrm{S}}) = \gamma_{\mathrm{LV}}^{0} - \frac{\Gamma_{\mathrm{LV}}\mathcal{R}T}{n_{\mathrm{LV}}}\ln\ (1 + K_{\mathrm{LV}}C_{\mathrm{S}}^{n_{\mathrm{LV}}}), \tag{3.3}$$

where γ_{LV}^{0} is the LV interfacial tension of pure water, i.e., for $C_{\mathrm{S}} = 0, \Gamma_{\mathrm{LV}}$ is the maximum surfactant concentration at the LV interface, $\mathcal{R}$ is the universal gas constant, T is the absolute temperature, K_{LV} is the adsorption equilibrium constant, and n_{LV} is an empirical fitting parameter. These LV adsorption parameters (Γ_{LV}, K_{LV}, and n_{LV}) are obtained by fitting eq. (3.3) to the experimental data of surface tension as a function of DDAB concentration [100, 99], i.e., $\gamma_{\mathrm{LV}}(C_{\mathrm{S}})$.

To account for the surfactant adsorption on the SL interface, we applied a similar approach by solving Young's equation [7]: $\cos\theta_{\mathrm{Y}} = (\gamma_{\mathrm{SV}} - \gamma_{\mathrm{SL}})/\gamma_{\mathrm{LV}}$, where γ_{SV}, γ_{SL}, and γ_{LV} are the interfacial tension at the SV, SL, and LV interfaces, respectively. Using the Gibbs adsorption, i.e., eq. (3.1) and Zhu-Gu eq. (3.2) for the SL and LV interfaces, one can arrive at a modified Young equation [154] depending on surfactant concentration:

$$\theta_{\mathrm{Y}}(C_{\mathrm{S}}) = \cos^{-1}\left(\frac{\cos\theta_{\mathrm{Y}}^{0}\gamma_{\mathrm{LV}}^{0} + \frac{\Gamma_{\mathrm{SL}}^{\infty}\mathcal{R}T}{n_{\mathrm{SL}}}\ln\ (1 + K_{\mathrm{SL}}C_{\mathrm{S}}^{n_{\mathrm{SL}}})}{\gamma_{\mathrm{LV}}^{0} - \frac{\Gamma_{\mathrm{LV}}^{\infty}\mathcal{R}T}{n_{\mathrm{LV}}}\ln\ (1 + K_{\mathrm{LV}}C_{\mathrm{S}}^{n_{\mathrm{LV}}})}\right), \tag{3.4}$$

where θ_{LV}^{0} is the Young contact angle for pure liquid on flat PDMS. This modified Young equation relates the contact angle of a drop on flat homogeneous surface with C_{S} (i.e., $\theta_{\mathrm{Y}}(C_{\mathrm{S}})$) and is used to fit our experimental data of $\theta_{\mathrm{Y}}(C_{\mathrm{S}})$ on flat PDMS to compute the surfactant adsorption parameters (i.e., Γ_{SL}, K_{SL}, and n_{SL}) at the SL interface (see Appendix B.2 for the details regarding the data fitting).

Two classical models are widely used to describe the contact angle on rough, rigid, homogeneous, and chemically inert surfaces. On the one hand, Wenzel (W) [8] equation is applied when the liquid has fully penetrated the cavities of the surface: $\cos\theta_{\mathrm{W}} = r\cos\theta_{\mathrm{Y}}$, where θ_{W} is the Wenzel CA, and r is the surface roughness. On the other, when the liquid sits on top of the surface texture, with air trapped beneath the drop in the surface cavities, Cassie-Baxter (CB) [9] equation is used: $\cos\theta_{\mathrm{CB}} = \phi\cos\theta_{\mathrm{Y}} - (1-\phi)$, where θ_{CB} is CB CA and ϕ is the packing fraction of the liquid-solid surface area (pillar-top area) to the total (SL and LV) areas. To account for the surfactant adsorption for a drop on such rough surfaces, C_{S}, r and ϕ will affect surfactant adsorption since the surfactant molecules will adsorb to both the LV and SL interfaces. Following the same process by substituting the modified Young equation (eq.(3.4)) into the W and CB equations, we arrive in the forms of the Milne et al.[154] modified W and CB CA equations:

$$\theta_{\mathrm{W}}(C_{\mathrm{S}}) = \cos^{-1}\left(\frac{\cos\theta^{0}_{\mathrm{W}}\gamma^{0}_{\mathrm{LV}} + r\frac{\Gamma^{\infty}_{\mathrm{SL}}\mathcal{R}T}{n_{\mathrm{SL}}}\ln\ (1 + K_{\mathrm{SL}}C_{\mathrm{S}}^{n_{\mathrm{SL}}})}{\gamma^{0}_{\mathrm{LV}} - \frac{\Gamma^{\infty}_{\mathrm{LV}}\mathcal{R}T}{n_{\mathrm{LV}}}\ln\ (1 + K_{\mathrm{LV}}C_{\mathrm{S}}^{n_{\mathrm{LV}}})}\right), \tag{3.5}$$

$$\theta_{\mathrm{CB}}(C_{\mathrm{S}}) = \cos^{-1}\left(\frac{\cos\theta^{0}_{\mathrm{CB}}\gamma^{0}_{\mathrm{LV}} + \phi\frac{\Gamma^{\infty}_{\mathrm{SL}}\mathcal{R}T}{n_{\mathrm{SL}}}\ln\ (1 + K_{\mathrm{SL}}C_{\mathrm{S}}^{n_{\mathrm{SL}}}) + (1-\phi)\frac{\Gamma^{\infty}_{\mathrm{LV}}\mathcal{R}T}{n_{\mathrm{LV}}}\ln\ (1 + K_{\mathrm{LV}}C_{\mathrm{S}}^{n_{\mathrm{LV}}})}{\gamma^{0}_{\mathrm{LV}} - \frac{\Gamma^{\infty}_{\mathrm{LV}}\mathcal{R}T}{n_{\mathrm{LV}}}\ln\ (1 + K_{\mathrm{LV}}C_{\mathrm{S}}^{n_{\mathrm{LV}}})}\right), \tag{3.6}$$

where θ^{0}_{W} and θ^{0}_{CB} are the W and CB CAs for pure liquid on a rough surface and can be estimated using: $\cos\theta^{0}_{\mathrm{W}} = r\cos\theta^{0}_{\mathrm{Y}}$ and $\cos\theta^{0}_{\mathrm{CB}} = \phi\cos\theta^{0}_{\mathrm{Y}} - (1-\phi)$, respectively. Here, θ^{0}_{Y} is the Young CA for pure water on a flat PDMS surface, $\mathcal{R}$ is the universal gas constant, T is the absolute temperature, $\Gamma^{\infty}_{\mathrm{LV}}$ and K_{LV} are Zhu–Gu [155] adsorption parameters that describe the maximum surfactant concentration at the LV interface and the equilibrium constant for adsorption, respectively. $\Gamma^{\infty}_{\mathrm{SL}}$ and K_{SL} represent similar quantities but for the SL interface, and n_{LV} and n_{SL} are empirical fitting parameters in the Zhu–Gu [155] adsorption isotherm.

Eqs. (3.4) - (3.6) are predictive equations to quantify the influence of DDAB surfactant adsorption at the LV and SL interfaces on the contact angle of the drops on flat and textured surfaces (characterized by ϕ and r). In terms of physical mechanisms, the first term in the numerator in eq. (3.5) and eq. (3.6) describes the effect of the surface roughness and the solid-fraction on the CA of pure water. The second term in the numerator expresses the effect of surfactant adsorption on the SL interface. The third term in the numerator in the modified CB equation and the denominator for both modified W and CB equations describe the effect of surfactant adsorption on the LV interface as a function of C_{S} in determining the contact angle on textured surfaces. It is worth noting that we have not considered any pinning effects for both CB and W contact angles. On the one hand, such theoretical prediction for a Wenzel state, usually with pinning contact line, can contribute to some errors, and has shown a deviation from the experimental data by previous studies using SDS surfactants [154]. On the other hand, such consideration without a contact line pinning is acceptable for predicting a CB contact angle since the CB mode generally accompanies with high CAs and high mobility [156]. In addition, to the best of our knowledge, no predictive theory for the pinning of the contact line in the CB state is available.

3.4 Results and Discussion

3.4.1 Wetting states

Figure 3.2 shows the side and bottom-view snapshots on both superhydrophobic microstructures (surfaces S1 and S2) with two distinct wetting states: Cassie-Baxter (CB) and Wenzel (W). To distinguish between these states, a bright contact area at the center was observed when the drop sitting on top of the surface roughness with air underneath, representing a CB drop. In contrast, a dark central, contact area was observed when water completely wets the surface structure as in a Wenzel state. Such color contrast (bright vs. dark) between the CB and Wenzel wetting is caused by the different refractive indices between air and water.

Our results shown in Fig. 3.2 reveal that drops were in a CB state when C_{S} between 0 and 0.25 on the higher-r SH surface S1 ($r = 2.31$, $\phi = 0.34$) but in a W state when C_{S} ranges from 0.5 to 1 (Fig. 3.2a). On the lower-r SH surface S2 ($r = 1.33$ and $\phi = 0.08$), with 9-10 independent experiments, we observed that DDAB drops of C_{S} between 0 and 0.75 can sometimes form a CB or a Wenzel wetting state, while their representative experimental snapshots are shown in Fig. 3.2(b1) and 3.2(b2), respectively. At 1 CMC, DDAB drops were always in a Wenzel wetting state for both SH surfaces, S1 and S2. We discuss and explain the probability for the presence of different wetting states (being a CB or Wenzel state) experimentally and theoretically in the later sections. In brief, depending on the surface parameters, r and ϕ, there is a wetting transition from a CB to W wetting state of DDAB drops with increasing C_{S} for both SH surfaces.

3.4.2 C_{S}-dependent contact angles

Fig. 3.3 shows the experimental and theoretical results for the C_{S}-dependent CAs of CB and W drops on both SH surfaces: S1 (♦) and S2 (●). The CAs of CB drops on the SH

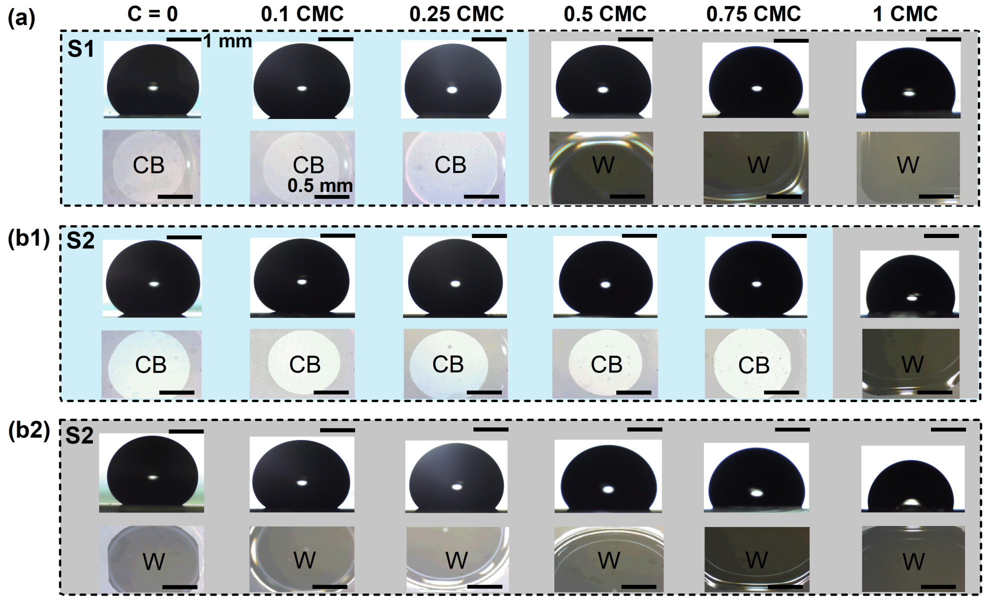

Figure 3.2. Side- and bottom-view snapshots of drops with different surfactant concentrations of DDAB, C (0 to 1 CMC), on the SH microstructured surface S1 ($r = 2.31$, $\phi = 0.34$) in (a) and surface S2 ($r = 1.33$, $\phi = 0.08$) in (b1 and b2), showing a transition from Cassie–Baxter (CB) to Wenzel (W) wetting at high DDAB concentration. Both DDAB concentration and the surface parameters influence the wetting state. On one hand, as revealed in (a), DDAB drops on the high-r SH surface (S1) were always in a gas-trapping CB state at low C (of $C = 0$ to 0.25 CMC) and a Wenzel state at high C. On the other, we observed that low-C drops (of $C = 0$ to 0.75 CMC) can sometimes form a CB, as shown in (b1), or a Wenzel state, as revealed in (b2), on the lower-r SH (S2). At 1 CMC, all drops were in a W mode.

microstructures, S1 (♦) and S2 (●), were almost constant regardless of the change in C_{S}. However, the CAs decreases with increasing C_{S} for Wenzel drops and reach a minimum value of $\theta \simeq 100°$ and $\theta \simeq 80°$ for S1 (◇) and S2 (□), respectively.

The theoretical predictions were estimated using the modified W and CB equations, i.e., eq. (3.5) and (3.6). As revealed in Fig. 3.3, there is a good agreement between our experimental data (filled symbols) and the predictions (solid lines, eq. (3.6)) of the C_{S}-dependent CAs of CB drops, particularly for the SH surface S2. This better agreement for the S2 may be attributed to the smaller solid fraction (lower ϕ) and, hence, less pinning of the contact line. Both measured and predicted CB CAs on the lower-ϕ S2 are larger compared to those on the higher-ϕ S1 due to greater liquid-air contact with smaller ϕ.

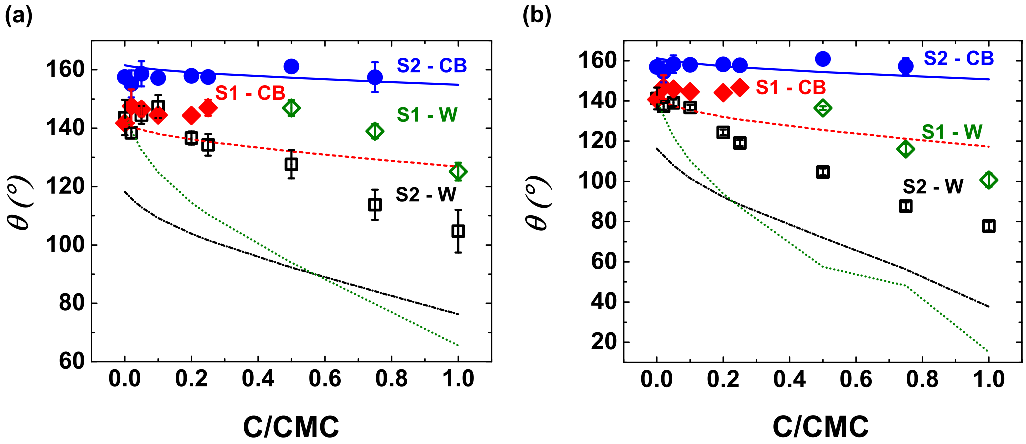

Figure 3.3. Measured and predicted contact angles for DDAB droplets at concentrations between 0 and 1 CMC on two SH microstructures: high-r S1 and and low-r S2. The CA data were measured during the first 10 s in (a) and last 10 s in (b) of a period of 100 s right after the droplet deposition. Different symbols denote CB (♦) and W (◇) drops on the high-r S1, while CB (●) and W (□) drops on the low-r S2. The error bars represent the standard deviations of ten drops for each C_{S}. Theoretical prediction of the CB and W contact angles considering surfactant adsorption, given by eqs. (3.5)-(3.6), are also plotted for S1 (- - -, ⋯⋯) and S2 (—, -·-·), respectively.

While there is a good agreement of the C_{S}-dependent contact angles of CB drop on both SH surfaces, the prediction using a modified W equation was not good for both S1 (⋯⋯) and S2 (-·-·) surfaces (dashed lines in Fig. 3.3). This may be attributed to a larger deviation due to the pinning contact line whose effect was not considered in the theory for a Wenzel DDAB drop on the microstructures [91, 157]. In addition, to get better predictions of the C_{S}-dependent CAs of W-state drops, one may need to include the contribution from pinning for W drops due to the greater solid-liquid contact area (higher ϕ) [157, 158]. It has been shown that the modified CB equation can predict the measurements of CB CAs successfully and can be expanded to other types of surfaces with different ϕ and r values as well as various surfactant solutions once the data of θ_{Y} and γ_{LV} are available.

3.4.3 Advancing and receding contact angles

The wetting behavior of DDAB surfactant drops on flat PDMS and both microstructured SH surfaces S1 and S2 is also investigated through the measurements of advancing (θ_{Adv})

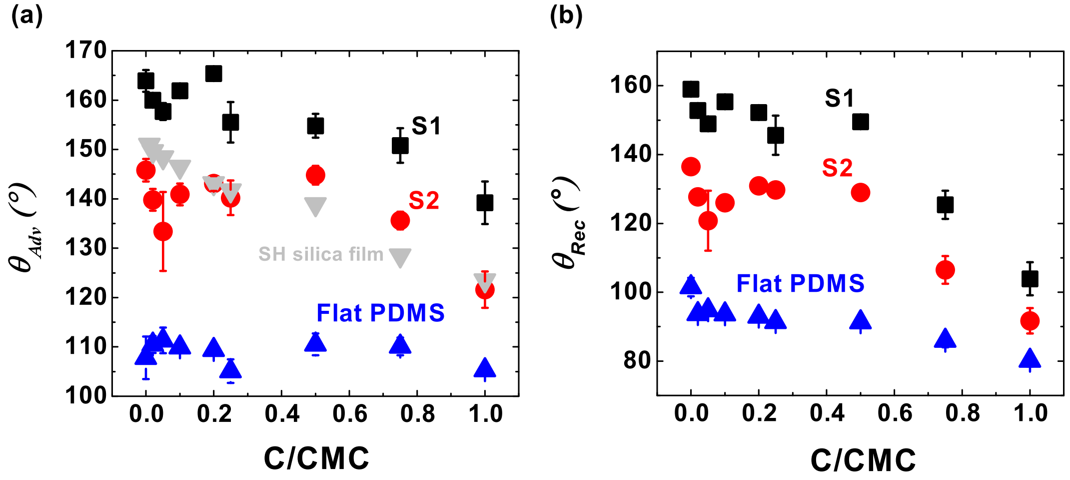

Figure 3.4. (a) Advancing and (b) receding contact angles measured for DDAB drops at for different concentrations between 0 and 1 CMC on three types of surfaces: Flat PDMS (▲), SH microstructures S1 (■) and S2 (●), using a sessile drop method by adding (or withdrawing) liquid to measure the advancing (or receding) CAs. Error bars show the standard deviations obtained from ten experiments. The advancing contact angles for DDAB drops on a SH silica-based thin film (▼) are plotted for comparison [96].

and receding (θ_{Rec}) CAs as a function of C_{S}, shown in Fig. 3.4a and 3.4b, respectively. On higher-r S1, the advancing and receding CAs for pure water ($C_{\text{S}} = 0$) measured to be $\theta_{\text{Adv}} = 163.9 \pm 2.2°$ and $\theta_{\text{Rec}} = 159.0 \pm 1.4°$, respectively. Both the advancing and receding CAs decrease with increasing C_{S} and reach a minimum value when $C_{\text{S}} = 1$ of $\theta_{\text{Adv}} = 139.3 \pm 4.3°$ and $\theta_{\text{Rec}} = 103.9 \pm 4.8°$, respectively. The lower-ϕ and r S2, on the other hand, showed lower advancing and receding CAs of pure water $\theta_{\text{Adv}} = 145.8 \pm 2.3°$ and $\theta_{\text{Rec}} = 136.5 \pm 0.74°$. We may attribute the lower advancing and receding CAs on S2 to a CB to Wenzel wetting transition, which occurs during the measurement and subsequently the liquid homogeneously wets on the surface textures resulting in a lower CA. Similarly, as C_{S} is increased, the advancing and receding CAs on S2 start to decrease when $C_{\text{S}} > 0.5$ and reach a minimum value at $C_{\text{S}} =1$ of $\theta_{\text{Adv}} = 121.6 \pm 3.7°$ and $\theta_{\text{Rec}} = 91.7 \pm 3.7°$, respectively. Both surfaces S1 and S2 lost their superhydrophobicity with increasing C_{S} when $C_{\text{S}} > 0.5$ (Fig. 3.4a-b).

As shown in Fig. 3.4a, our measurement for the advancing CA on S2 reveals a good agreement with that on SH thin-film porous sol–gel surface (▼)[96]. Finally, the advancing CAs on flat PDMS are nearly constant for C_S from 0 to 1, while the receding CAs reduce from $\theta_\mathrm{Rec} = 101.5 \pm 2.7^\circ$ at $C_\mathrm{S} = 0$ to $\theta_\mathrm{Rec} = 80.1 \pm 1.7^\circ$ at $C_\mathrm{S} = 1$.

3.4.4 Free energy analysis for the stability and metastability of the wetting states

Although the modified CB eq. (3.6) well predicted C_S-dependent CA for CB drops, it doesn't explain the probability and the stability of the wetting states (shown in Fig. 3.2). To get a better understanding concerning the stability and the metastability of the observed wetting behavior and to explain the occurrence of different wetting states depending on the C_S on the different microstructures, we carried out an analysis starting from the Gibbsian thermodynamics [15, 91, 159, 160, 161, 162, 163], following the work by Shardt et al. [91] using SDS surfactants, and analytically estimated the free energy (E) for our composite system of DDAB-laden surfactant droplets sitting on a microstructured surface. The derived free energy equation, $E - E_0$, with respect to the assumed reference state has the form of Shardt et al. [91] free energy:

$$E - E_0 = \gamma_\mathrm{LV} \pi R^2 (2 - 3\cos\theta + \cos^3\theta) - 4\pi\gamma_\mathrm{LV} R_0^2, \tag{3.7}$$

where E_0 is the free energy at the assumed reference state of a spherical drop without any SL contact; R is the spherical cap radius of curvature; R_0 is the initial radius of a spherical drop of 10 μl; $\cos\theta = f\cos\theta_\mathrm{Y}(C_\mathrm{S}) - f_1$. Here, f is the ratio of the SL surface area (pillar-top area) to the total (SL and LV) areas, and f_1 is the ratio of the LV interfacial area to the total projected area beneath the drop (See Appendix B.3 for the derivation).

We followed a model that a droplet transiting from CB to W wetting state usually occurs through two main phases described below [15, 16, 91]. In this first phase, after droplet deposition, the liquid is falling down along the pillars with an assumed flat LV interface as in a CB wetting state (with $f = \phi$ and $f_1 = 1 - \phi$), until it wets the bottom of the surface. Here, we assume that only the cylinder's walls are wet and the bottom surface is not wet, so f increases and $f_1 = 1 - f$. At the end of the first phase, the value of f further increases

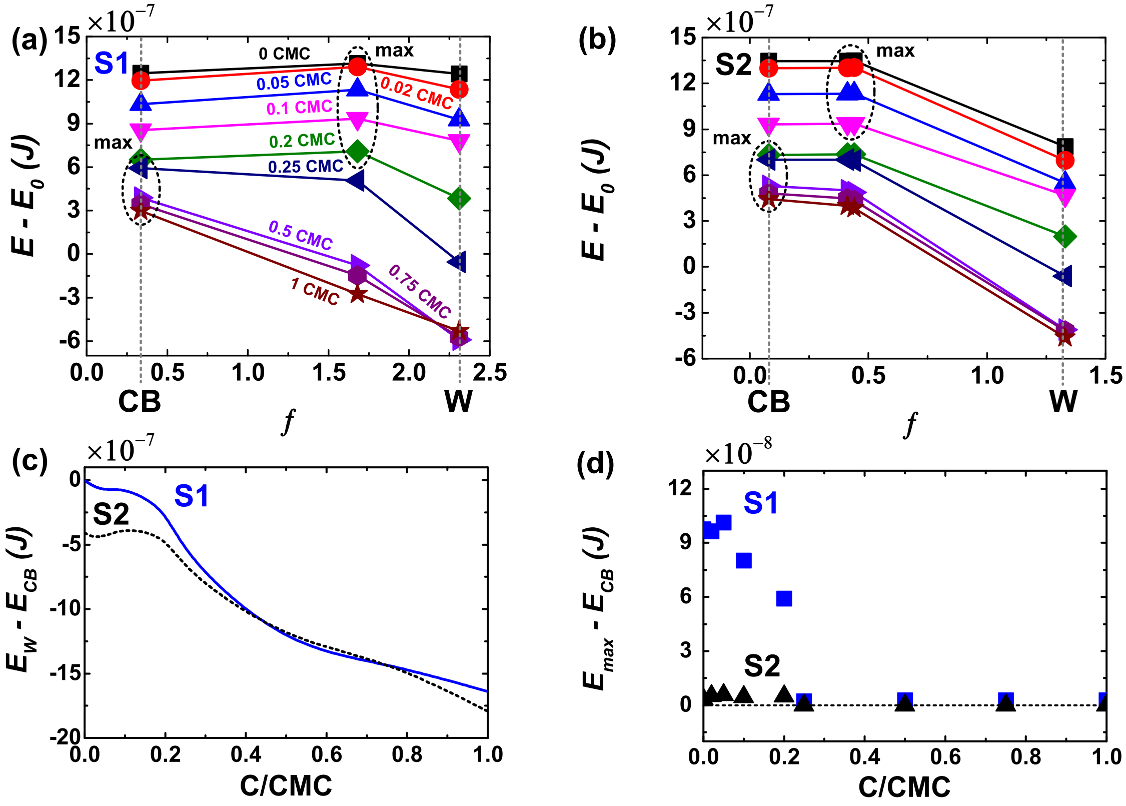

Figure 3.5. Free energy (E) with respect to the reference state (E_0) during the wetting transition of the drop from CB to W passing through the intermediate states where the drop partially wet the microstructures for 9 surfactant concentrations on SH surfaces S1 in (a) and S2 in (b). (c) The difference between the W and CB free energy as a function of $C_\mathrm{S} = C/CMC$ is of the order of 10^{-7} J for S1 (━) and S2 (┅). (d) The free energy barrier (i.e., the difference between the maximum free energy (E_{max}) and the CB free energy, $E_{max} - E_{CB}$, as a function of C_S for S1 (■) and S2 (▲).

as the solid–liquid contact area increases. In the second phase, liquid gradually wets the bottom surface from the pillar edges towards the center. In other words, f continues to increase until the bottom area is completely wetted with the liquid, while $f_1 = r - f$. A full transition to Wenzel wetting occurs when $f = r$ and $f_1 = 0$, where $\cos\theta = r\cos\theta_\mathrm{Y}(C_\mathrm{S})$ as in the Wenzel equation [8, 9, 15].

Fig. 3.5 (a-b) shows the free energy, E, of DDAB-surfactant droplets with respect to the chosen reference state, E_0, for nine different values of C_S on the high-r SH surface S1 in (a) and low-r S2 in (b), as a function of f. Here f describes the depth of liquid penetration in between the pillars. On the one hand, for droplets with C_S from 0 to 0.2 CMC on both

SH surfaces, the free energy first increases as f increases until the maximum free energy (E_{max}) is reached, and subsequently decreases to reach a minimum value of the free energy in a Wenzel state. On the other, for C_{S} between 0.25 and 1 CMC on both surfaces, the free energy of the DDAB drop initially starts from a maximum value at a CB state and continuously declined as f increases until the Wenzel state, which has lower free energy by $\mathcal{O}(10^{-7}J)$ compared to that of the CB state. The difference in the free energy between W and CB as a function of C_{S} (Fig. 3.5c), $E_W - E_{CB} < 0$, reveals that Wenzel state is theoretically and thermodynamically preferred since E_W is the lowest, in agreement with the typical CB-W transition criterion observed previously for pure liquid [11, 13, 14, 15, 164, 165]. However, based on the analysis there is a free energy barrier between the CB and W states, $E_{max} - E_{CB} > 0$ (see Fig. 3.5d), to be overcome for a drop to transient to W state for both SH surfaces at $0 \lesssim C_{\mathrm{S}} \lesssim 0.25$. In other words, the CB is metastable due to the free energy barrier at these concentrations (See Appendix B.4 for the derivation).

The predicted free energy barrier, $E_{max} - E_{CB} > 0$, for the higher-r S1 (■) is relatively higher when $C_{\mathrm{S}} \leq 0.25$, of the order of magnitude of $O(10^{-8} - 10^{-7}J)$ (shown in Fig. 3.5d), and is consistent with our experimental observations that all DDAB drops are in a CB state on S1 (revealed in 3.6a). The presence of the high energy barrier for S1 makes a CB state thermodynamically more favourable at these concentrations. In contrast, due to the lower energy barrier of $O(10^{-8}J)$ for low-r SH S2 (shown in Fig. 3.5d), some droplets were observed to be in a CB state while some at a Wenzel wetting state for C_{S} between 0 and 0.75 CMC. Fig. 3.6b shows the respective probability of a CB or W wetting state observed based on ten independent experiments. At high $C_{\mathrm{S}} = 1$ CMC, a W state was observed on both surfaces.

Apart from our two types of SH surfaces investigated, we provide a layout of optimal r and ϕ for designing robust SH surfaces with a stable CB state that has various beneficial applications such as self-cleaning. By equating $E_{CB} = E_W$ using eq. (C.2), one can arrive at the physical criterion of the critical modified Young's contact angle for a surfactant-laden droplet, θ^*_{Y}, which delineates the surface parameters for a stable CB *vs.* Wenzel state:

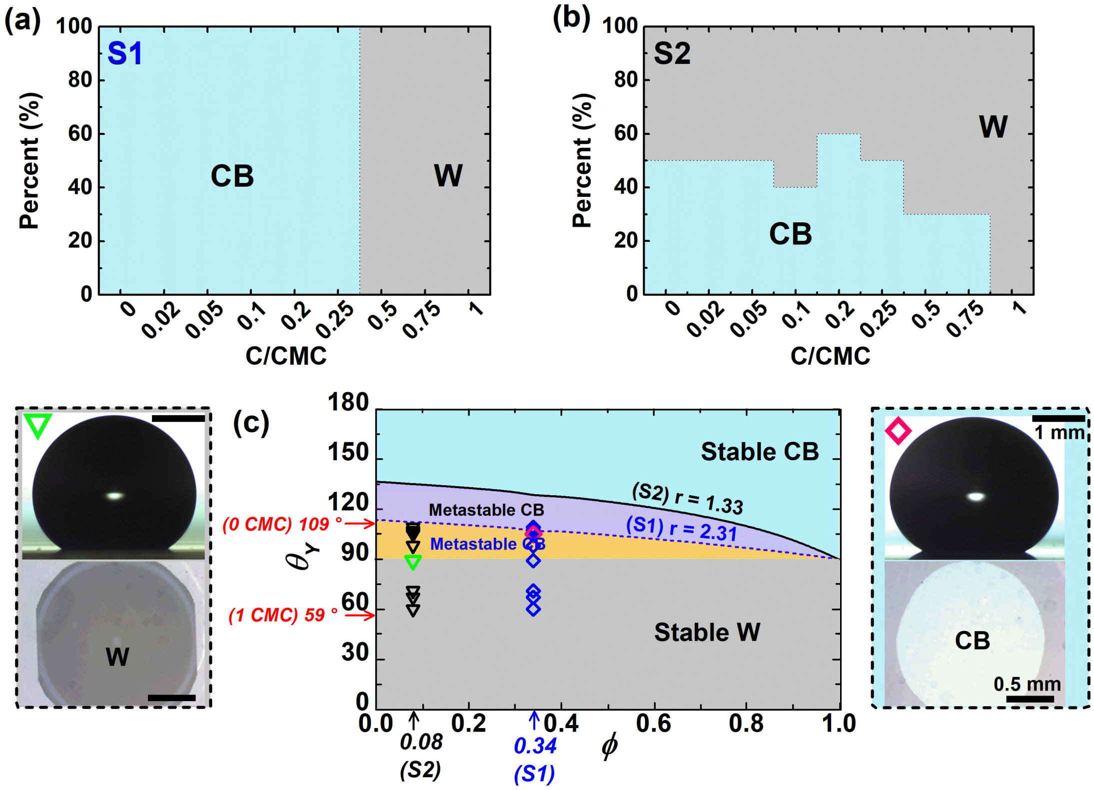

Figure 3.6. Percentage of experimental droplets in a Cassie-Baxter (CB) and Wenzel (W) state as a function of normalized surfactant concentration (C_{S}) for high-r S1 in (a) and low-r S2 in (b), based on an average of ten independent droplets for each DDAB surfactant concentration. (c) Phase diagram of CB and W wetting states based on the free energy analysis eq. (C.2) as a function of the solid-liquid fraction (ϕ) and the Young's modified contact angle on a Flat PDMS, $\theta_Y(C_{\mathrm{S}})$ for two different surface roughnesses (r). Symbols show the modeled CAs for the experimental parameters of r and ϕ for the SH S1 (◇) and S2 (▽) for C_{S} between 0 and 1 CMC, while $\theta_Y(C_{\mathrm{S}} = 0) = 109°$ and $\theta_Y(C_{\mathrm{S}} = 1) = 59°$ for DDAB-laden droplets. Side- and bottom-view snapshots showed a stable W (Left, ▽) and a metastable CB (Right, ◇) drops, respectively. In (c), the critical boundaries delineating the stable CB and Wenzel states are depicted by the lines for both S1 (- - -) and S2 (—), using the criteria derived, namely $\cos\theta^*_{\mathrm{Y}}(C_{\mathrm{S}}) = \left(\frac{\phi-1}{r-\phi}\right)$.

$\cos\theta^*_{\mathrm{Y}} = (\frac{\phi-1}{r-\phi})$ [14, 164, 165]. In the phase diagram shown in Fig. 3.6c, using this method we summarize the thermodynamic stability predictions of wetting states depending on C_{S}, θ_{Y}, ϕ, and r. A stable CB region is predicted for a large $\theta_{\mathrm{Y}} < \cos^{-1}\left(\frac{\phi-1}{r-\phi}\right)$, whereas a stable Wenzel state occurs for small θ_{Y} ($\leq 90°$) in Fig. 3.6c. The valid range of θ_{Y} to establish robust, stable CB state for our DDAB surfactant droplets is ranging from 109° to 135° for

S1 and S2, respectively, as shown in Fig. 3.6c. In comparison, this angle depends on both the type of surfactant used and the surface material, and some studies reported different ranges in the literature. Milne et al. [154] reported that the range of θ_{Y} of sodium dodecyl sulfate (SDS) on smooth Teflon is ranging between 112° and 93°. Shardt et al. did another recent study [91] using SDS surfactant on flat PDMS and showed a different range from 99° to 92°. In the case of Triton X-100 and CTAB surfactants, the contact angles on smooth PTFE surface are larger than that of SDS on flat PDMS (from 110° to 92° and from 110° to 95° of Triton X-100 and CTAB, respectively) [166].

To examine the occurrence of metastable CB state in our experiments, we used a theoretical criteria based on the differential of the free energy barrier with respect to f, i.e., $\partial E/\partial f|_{f=\phi} > 0$ [16, 91]. From Fig. 3.6c and using such criterion, we can conclude that for the metastable CB state to appear, θ_{Y} should be greater than 90°, while a Wenzel state is thermodynamically stable for all ϕ and r with a small $\theta_{\mathrm{Y}} \leq 90°$. In addition, the metastable CB region for S1 extends from $\theta_Y = 90°$ to the blue dashed line (orange area), while that for S2 expands from $\theta_Y = 90°$ to the black solid line and overlaps with the metastable CB region for S1. These are in agreement with our experimental observations, where W states appeared at higher C_{S} (i.e., low θ_Y) and metastable CB states observed for lower C_{S} (i.e., high θ_Y).

3.5 Conclusions

In summary, we experimentally measured the contact angles and wetting states of DDAB surfactant-laden drops for nine different concentrations on two types of superhydrophobic microstructures of different packing-fraction (ϕ) and surface roughness (r). A model considering surfactant adsorption at the LV and SL interfaces has been derived and compared to these experimental data. The experimental data and the theoretical predictions of the CB contact angles were in good agreement. However, the theoretical prediction using a modified W equation didn't predict well the Wenzel contact angles for both surfaces, likely due to the pinning effects of the wetting contact line. We further consider thermodynamic surface energies to predict the stability or metastability of the wetting states depending on C_S. We found that the Wenzel state is thermodynamically favorable for both SH surfaces at all DDAB concentrations, but there is a free energy barrier between the CB and W states for $C_\mathrm{S} \leq 0.25$ for our SH surfaces. This thermodynamic analysis implies that the CB state is metastable at these concentrations and, moreover, this metastable CB state becomes more stable on surfaces with greater ϕ and r. Based on the free energy barrier and the adsorption thermodynamics for surfactant-laden drops, we highlight the prediction of a stable and robust gas-trapping, CB state superhydrophobic microstructures beneficial for various applications of self-cleaning and low-friction, when meeting the following two criteria: first, a large Young contact angle of a surfactant-laden drop on the flat surface: $\theta_\mathrm{Y}(C_\mathrm{S}) > 90^\circ$ and, second, large values of r and ϕ which satisfy $\cos\theta_\mathrm{Y}(C_\mathrm{S}) < (\frac{\phi-1}{r-\phi})$.

Chapter 4

Fabrication of transparent and microstructured superhydrophobic substrates using additive manufacturing[1]

4.1 Introduction

Superhydrophobic (SH) surfaces consist of hydrophobic material with micro- and nano-scale roughness or structures, with a static water contact angle (CA) greater than 150° [11], and have attracted significant interest due to their importance in both scientific research and practical applications. Many natural living systems such as lotus leaves [25, 26, 27], ramee leaves [167], rice leaves [168], and butterfly wings [169] exhibit superhydrophobicity, giving rise to self-cleaning [35, 37, 170], water or oil repellency [51, 53], drag-reduction [42], anti-icing [44], anti-fouling [106], and many other appealing applications. These applications have inspired many researchers to develop artificial SH surfaces with biomimetic structures

---

[1] The material presented in this chapter is based on Aldhaleai, A. and Tsai, P.A., "Fabrication of transparent and microstructured superhydrophobic substrates using additive manufacturing", submitted to Additive Manufacturing, 2020.

of an ultrahigh CA, but ultralow water adhesion.

The wettability of SH surfaces strongly depends on both the surface geometry (e.g., surface roughness and structures) and chemical nature (e.g., surface free energy). Therefore, most studies have mainly focused on either altering the chemical composition of the material or creating efficient micro- or nanoscale structures to fabricate robust SH structures. The effect of micro- or nanoscale structures on surface wetting is commonly attributed to two wetting modes: first, homogeneous Wenzel (W) wetting state, where the liquid fills in the surface cavities and completely wets the surface textures [8] and, second, heterogeneous wetting of Cassie-Baxter (CB) mode, in which the liquid drop sits on the top of the hydrophobic texture with gas trapped beneath the drop [9]. The gas-trapping CB wetting state, contributing to a large contact angle and a low CA hysteresis, is critical to resilient superhydrophobicity, which is beneficial for various applications in surface engineering. However, the long-term stability of the preferred CB state on SH surfaces is still challenging and can be lost through an irreversible wetting transition to Wenzel state, when exposed to a high-temperature environment [171], droplet evaporation [13], or surfactant additives [91, 96].

In so far, numerous efforts have been made in fabricating artificial robust hydrophobic or SH surfaces using several micromachining technologies, including lithography [172], chemical etching [28], deep reactive-ion etching (DRIE) [29], polymer coating [30], replica molding [31], self-assembly [32, 33], electrospinning [34], and so forth. These techniques are able to fabricate mostly two-dimensional (2D) patterns or 3D random structures or random roughness, unless using costly or multiple masks with specific geometries or simple 3D structures [66, 67, 68]. Albeit some studies reported complex 3D structures, their fabrication process is rather complicated, time-consuming, and expensive [36, 69].

Additive manufacturing (or 3D-printing technology) has recently attracted much interest because it can produce 3D structures with well-defined geometries on both rigid and flexible substrates via a one-step process and also utilize a wide variety of resin materials [70, 173]. Although a few of studies have lately demonstrated that a 3D-printing technology is effective

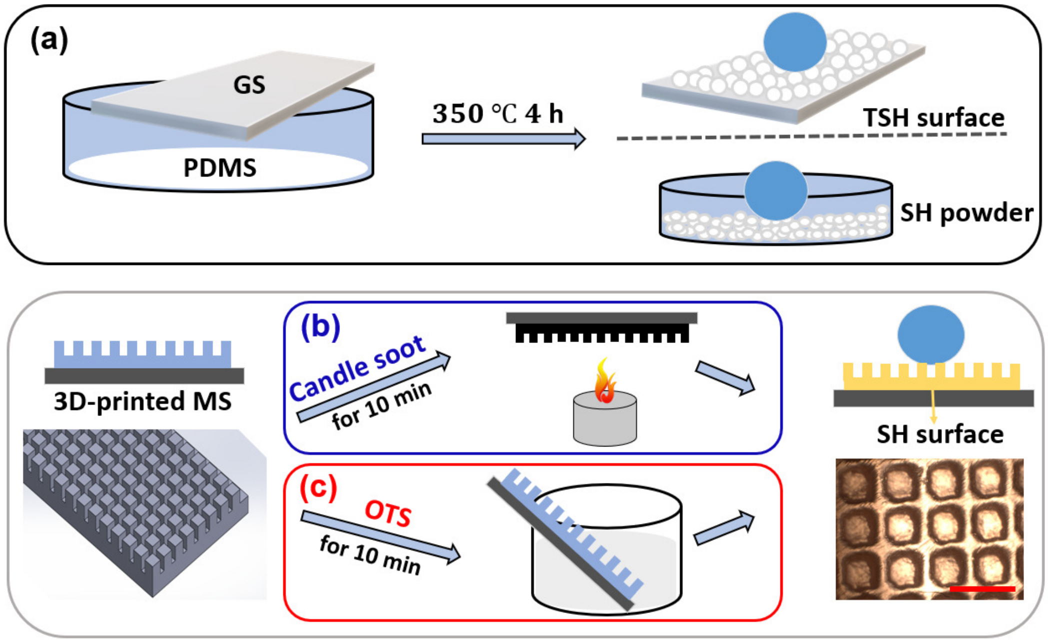

Figure 4.1. Schematic of the three processes for preparing superhydrophobic (SH) surfaces. In (a), transparent SH surface and SH powder were prepared using a one-step heating procedure of liquid PDMS at 350°C for four hours. When the liquid PDMS is heated, it decomposes and generates soot, depositing on a glass slide (GS) to form a transparent SH surface. The remaining silicon powder left in the pyrex also shows SH properties for water droplets. In (b) and (c), using two-step processes, we first 3D-printed microstructures (MS) and subsequently coated them with a hydrophobic coating with candle soot (top) or OTS solution (bottom) for 10 mins. The inset on the right shows the microscope (top-view) image of the 3D printed microstructures after a hydrophobic coating. The scale bar corresponds to 500 μm.

in manufacturing SH surfaces [22, 54, 55, 72, 73, 74, 75, 76, 174, 175, 176, 177, 178], there are still some challenges in the fabrication of resilient SH surfaces due to their short-term wetting stability or some additional complicated steps involved in the fabrication.

Here, we report facile and simple (one- and two-step) approaches to fabricate SH surfaces with a high CA and low roll-off angle (ROA) for self-cleaning and water-repellent applications (see Fig. 4.1). Using the one-step method, we are able to produce transparent superhydrophobic (TSH) surfaces with random roughness, to study the influence of random structures vs. regular patterns on the wetting properties and contact angles of water droplets on the SH surfaces fabricated. In the two-step process, we incorporate a 3D-printing technique with a hydrophobic coating to produce robust SH textures composed of regular square pillars, which are designed according to a thermodynamic theory for a stable gas-trapping CB state. Finally, our measurements of static and dynamic CAs of water droplets on all the prepared SH surfaces show high values and agree well with those predicted by using the Cassie–Baxter model [9].

4.2 Material and Methods

4.2.1 Chemicals and devices

Polydimethylsiloxane (PDMS) (Sylgard184, Part A) with a curing agent (methylhydrosiloxane with Pt catalyst, Part B) was supplied by (Dow Corning Corporation). Microscope glass slides (GS, 26 mm × 76 mm × 1 mm) were purchased from (Bio Nuclear Diagnostics Inc) for the fabrication of the transparent SH surfaces. A muffle furnace (Thermo scientific) was used for the heat treatment process. Pyrex was used as a container for the PDMS during the heat treatment. Octadecyltrichlorosilane (OTS), toluene, sulfuric acid, hydrogen peroxide, acetone, and ethanol were obtained from Sigma-Aldrich Canada. Commercial candles were used for the hydrophobic coating of candle soot. All of the reagents were used as received without any further treatment. The water used in this experiment was ultra-pure Milli-Q water (PURELAB Ultra, resistivity: 18.2 MΩ.cm). 3D microstructured substrates were 3D printed with a clear resin using a 3D printer (Formlabs, Form 2).

4.2.2 One-Step Fabrication of Transparent Superhydrophobic Surfaces

A glass slide (GS) was used as the solid substrate, which was repeatedly and ultrasonically cleaned with acetone, ethanol, and rinsed with Milli-Q water several times, and finally dried using a nitrogen gun. The substrates were subsequently placed in a freshly prepared "piranha" solution [14], a mixture of H_2SO_4/H_2O_2, 4:1 (v/v), for 1 h and rinsed several times with flowing Milli-Q water and finally dried with nitrogen. PDMS base and curing agent (at 10:1 mass ratio) were poured and mixed in a pyrex container for 10 mins. The mixture was then degassed in a vacuum desiccator until all the air bubbles were removed. The GS subsequently was placed upside down on the top of the pyrex, which contained the PDMS solution and was heated in a muffle furnace at 350° for 4 hours. The distance between the PDMS liquid and the GS, as shown in Fig. 4.1a, was about 1.5 cm. After the heat treatment (350° for 4 h), the liquid PDMS decomposed and generated soot, which in turn deposited on the upper GS, forming a transparent SH surface [179] (see Fig. 4.2a). The surface coated with PDMS soot had an average static water contact angle of $\theta \simeq 170 \pm 2°$, as shown by the side-view in Fig 4.2a. The remaining white silicon powder left in the pyrex also shows super-repellency against water.

4.2.3 Two-Step Fabrication Processes of 3D-printed Superhydrophobic microstructures

To obtain SH microtextures, we designed our surfaces to have regular micron-sized square pillars of width, D, height, h, and interspace, S, in a square lattice with a periodicity, $P = D + S$ (see Fig. 4.2b-c). The microstructures were characterized with two crucial geometrical parameters: solid-liquid packing fraction, ϕ, which is the ratio of the liquid-solid surface area (pillar-top area) to the total (liquid-solid and liquid-gas) areas, and surface roughness, r, corresponding to the ratio of the total surface area to the projected one (on a 2D plane). These parameters can be calculated using the following relations [181, 182]:

$$\phi = \frac{D^2}{P^2}, \tag{4.1}$$

$$r = \frac{P^2 + 4Dh}{P^2}. \tag{4.2}$$

Generally, r describes the relative change in the liquid/solid area for a rough surface compared to a flat surface in a Wenzel state [8]. ϕ describes the percentage of the liquid-solid contact area in a CB mode [9].

To design SH surfaces with a stable CB state, we use a model based on the comparison of the global surface energies, E_{CB} and E_{W}, for a CB and the Wenzel wetting droplet on

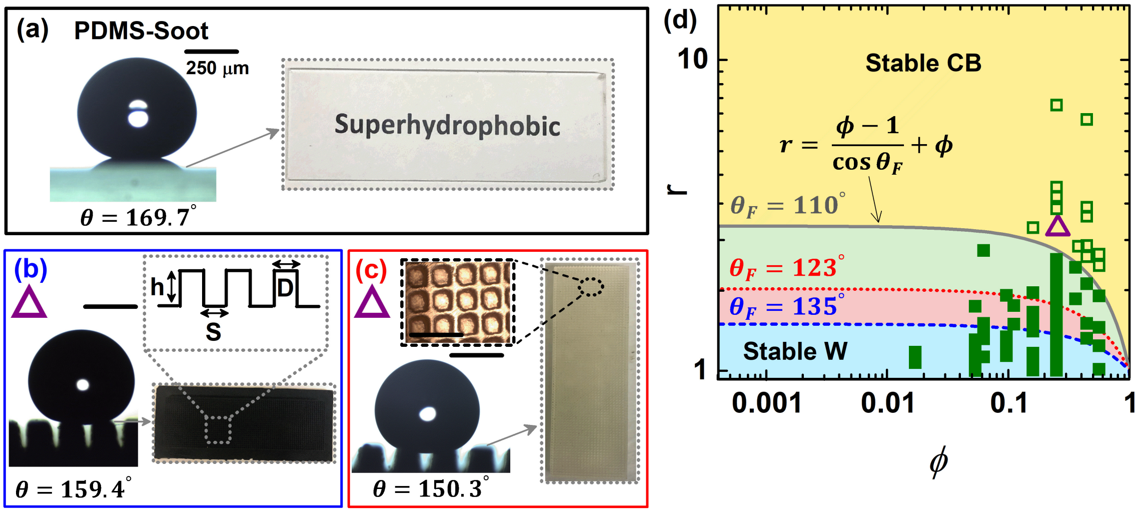

Figure 4.2. (a) Side-view of a water droplet deposited on the transparent PDMS-soot SH surface fabricated, revealing a Cassie-Baxter (CB) wetting state with an extremely high contact angle of $\theta = 169.7°$. Side-view of a water droplet deposited on the 3D-printed microstructures coated with candle soot (CS) in (b), while with OTS in (c). After the hydrophobic coating, the additive manufactured microtextures become superhydrophobic (SH) with a large contact angle ($\theta > 150°$), revealing a gas-trapping CB wetting state for a water droplet. The insets in (b) and (c) show the top-view of the SH micro-structures fabricated. The microtextures are 3D-printed with a square pillar pattern of pillar width (D), height (h), and separation distance (S), which are designed according to a thermodynamic theory to have a stable CB wetting state. Here, D, h, and S are of the order of magnitude of 10^{-4}m, yielding the surface roughness and packing fraction to be $r = 2.87$ and $\phi = 0.27$, respectively. The small inset in (c) shows an optical microscopic image of the top-view of the superhydrophobic surface coated with OTS (△). The scale bars in (b) and (c) correspond to 500 μm. (d) Phase diagram based on the energetic argument [14, 15, 180] can be divided into a stable CB state region (in the upper region, e.g., yellow) and a stable W phase (in the lower region, e.g., green, pink, and blue) for different Young's angles (θ_F). For a comparison, we also plot previous experimental data by Yeh and Chen using square-pillar microstructures [181] (with □, ■, denoting a CB and Wenzel state, respectively). The critical CB-W separation lines based on Eq. (4.3) are plotted for different Young's contact angles on flat surfaces, for Yeh and Chen's OTS-coated surface with $\theta_F = 110°$ [181] (—) as well as our surfaces coated with OTS of $\theta_F = 123°$ (······) and with CS of $\theta_F = 135°$ (- - -). At high surface roughness (r) and high solid-fraction (ϕ), the initial drop shape always exhibits CB states (denoted by the open symbols △ & □), whereas a Wenzel state (denoted by the filled symbols ■) is more likely observed experimentally at low r and ϕ.

the microstructures, respectively. The total surface energy E_{CB} or E_{W} is the magnitude of the total energies needed for creating interfaces when placing a CB or Wenzel drop onto the microstructures. According to thermodynamics, a stable CB occurs when E_{CB} has a lower energy compared to that of a W wetting mode, i.e., $E_{CB} < E_W$, by tuning the surface parameters of r and ϕ. One can arrive at the physical criterion of the critical contact angle θ^* that delineates the surface parameters for a stable CB vs. Wenzel state, by equating $E_{\mathrm{CB}} = E_{\mathrm{W}}$ [11, 13, 14, 15, 16]:

$$\cos\theta^* = \frac{\phi - 1}{r - \phi}. \tag{4.3}$$

This criterion is plotted in Fig. 4.2d, while the detailed derivation is given in the Appendix C.1. For the given important surface properties of r, ϕ, and θ_{F}, which is Young's contact angle of a water droplet on the flat surface of the same material, a stable CB state can occur on the hydrophobic micro-structures with a high roughness $r > (\phi - 1)/\cos\theta_{\mathrm{F}} + \phi$ (i.e., the upper (yellow) area in Fig.4.2 d). Based on the criterion above, we designed using SolidWorks and subsequently printed two microstructured substrates using a 3D printer (Form2). In our designs, considering the printing resolution of our 3D printer, the microstructures are printed in an area size of 66 mm × 20 mm, with micropillars of $h = 750$ μm, $D = 410$ μm, and $S = 400$ μm. The corresponding surface parameters, according to eqs. (4.1)–(4.2), are $r = 2.87$ and $\phi = 0.27$, indicated by the symbol (△) in Fig. 4.2 d, and theoretically a stable CB wetting is expected for a water droplet on the SH microstructured fabricated.

We experimentally measured the contact angles of a water droplet on the flat 3D-printed surfaces coated with candle soot and OTS to be 135° and 123°, respectively, so as to estimate θ_{F} for these materials. With these values of θ_{F} measured, using eq. (4.3), we plot the critical criteria for the different θ_{F}-values in Fig. 4.2d. Based on the thermodynamic model, a stable CB drop occurs in the upper region above the critical criterion (i.e., higher r), whereas a Wenzel state is more favorable for low-roughness surfaces (i.e., the grey, pink, and blue regions for different Young angles, θ_{F}) since $E_W < E_{CB}$. In a good agreement, we always observed a CB state of the initial drop on the SH substrates fabricated with 3D printing since our microstructure design has $r = 2.87$ and $\phi = 0.27$, shown as (△) in Fig. 4.2d, which is located in the upper (yellow) region of a stable CB state (above the critical criterion boundary for the Young angle of interest, e.g., $\theta_{\mathrm{F}} = 135°$ and $123°$).

From the two 3D-printed microstructures, one of the printed substrates was subsequently coated with candle soot [183, 184, 185, 186], while the other with an OTS solution [187, 188, 189] to achieve super-repellent properties with a high contact angle. The former 3D-printed microstructured substrate was brought horizontally over the center of the candle flame upside down and moved across back and forth for 10 mins until the substrate became black to obtain a uniform layer of soot deposition (see Fig. 4.1b for the schematic procedure). The distance between the candle soot flame and the 3D-printed microstructures, as shown in Fig. 4.1b, was about 1-2 cm. The substrate treated with candle soot, shown in Fig. 4.2b, had an average static water contact angle of $\theta \simeq 158 \pm 2°$.

The second microstructure was dipped into an OTS/toluene solution (0.2 ml of OTS into 100 ml of toluene, 0.2 vol%) for 10 mins to allow the OTS to uniformly deposit on the sample (see Fig. 4.1c for the illustration). Substrate modified with OTS was cleaned by sonication in toluene and by rinsing again with toluene, ethanol, and Milli-Q water several times, and finally dried with nitrogen. The surface treated with OTS, shown in Fig. 4.2c, had an average static water contact angle of $\theta \simeq 147 \pm 2°$.

4.3 Results and Discussion

4.3.1 Wetting State and Contact Angle Measurements

The wettability of both the TSH and the 3D-printed SH microstructures (shown in Fig. 4.2) is characterized using static water CA, dynamic CA (in terms of the advancing and receding CAs), and the ROA. The roll-off angle (ROA) or so-called "the angle of inclination" is the minimum tilting angle at which a water drop rolls off a tilted SH surface. The ROA is measured experimentally using a movable stage (Thorlabs TTR001), which allows for accurately tilting from its initial horizontal position to an inclined position. While still horizontal, a 10 μl Milli-Q water droplet was gently deposited on the testing surface, after which the stage was slowly tilted until this droplet began to roll over the surface. At this

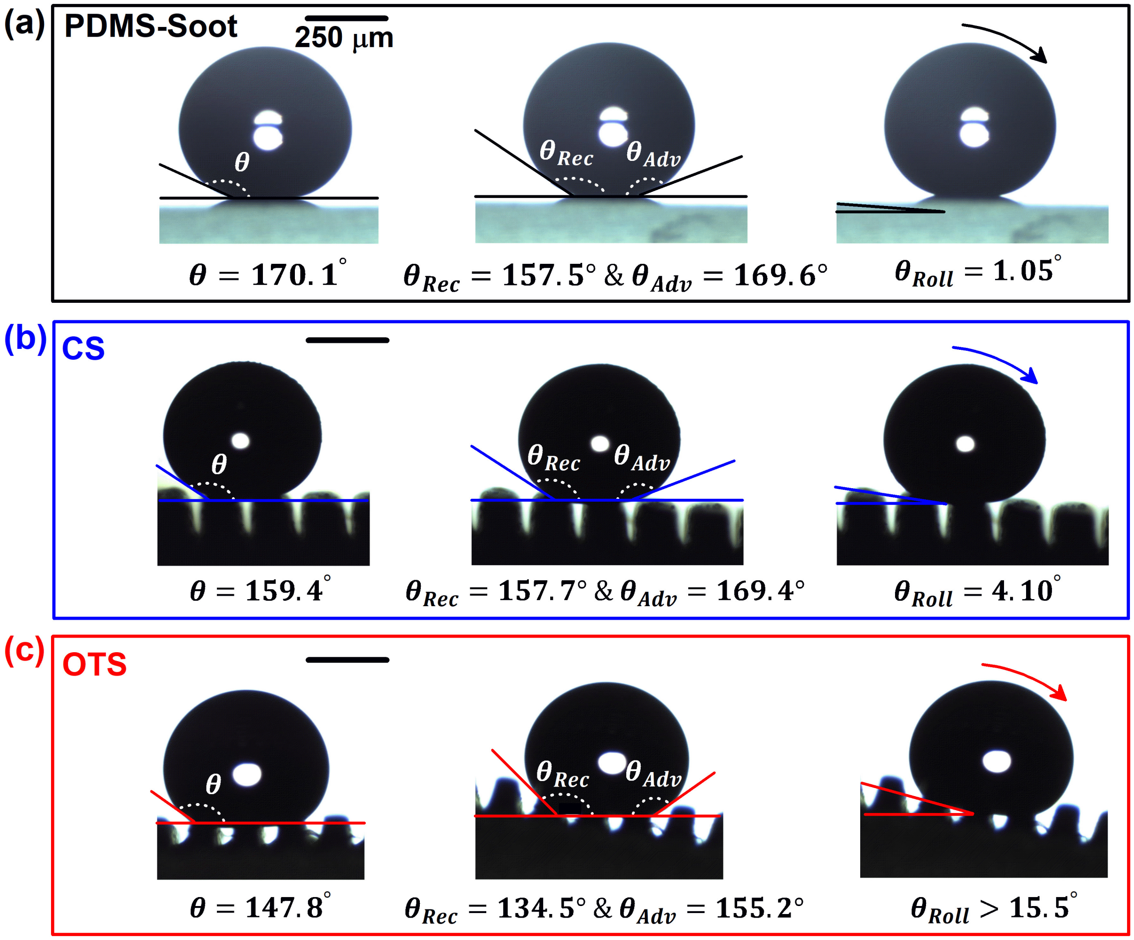

Figure 4.3. Comparison of water droplet static, dynamic (in terms of advancing and receding), and roll-off contact angles on (a) Glass substrate coated with PDMS-soot, (b) 3D-printed microstructures ($r = 2.87$, $\phi = 0.27$) coated with candle soot (CS), and (c) 3D-printed microstructures coated with OTS. Both the glass coated with PDMS-soot and the CS microstructured SH surfaces show a high static contact angle and a low roll-off angle, $\theta_{Roll} < 5°$.

point, the stage angle relative to horizontal was measured and recorded. This measurement was performed at least seven times for each sample, and all reported ROAs are averages of all measurements.

On the one hand, static water droplet CAs on the TSH surface with random roughness showed greater contact angle with $\theta \simeq 170 \pm 2°$. On the other, the static CA on the 3D-printed SH microstructures coated with CS and OTS were smaller, with $\theta \simeq 158 \pm 2°$ and

$\theta \simeq 147\pm2°$, respectively. All these fabricated substrates were superhydrophobic, i.e., $\theta \geq 150°$ as shown in Fig. 4.3. From Fig. 4.3a-b, we can clearly see the trapped air between the surface microstructures underneath the drop. Since both the 3D-printed microstructured SH surfaces have the same surface structure ($\phi = 0.27$ & $r = 2.87$) but have different static water droplet CA (by $\approx 10°$), revealing that not only the surface pattern but also the coating chemical composition can alter the SH CA on the surfaces. Two classical models have been used to describe surface wettability in terms of surface roughness r and solid-liquid contact area ϕ: Cassie-Baxter (CB) and Wenzel (W) models. In a CB state, the surface structure assumed to be partially wetted by the liquid. In this case, the liquid droplet is in contact with the top of the surface pattern, while a thin air layer is trapped beneath the drop. Surface texture, in the later, is assumed to be completely wetted with liquid in a W state. The contact angle for each model is formulated as follows [9, 8]:

$$\cos\theta_{\mathrm{CB}} = \phi\cos\theta_{\mathrm{F}} - (1-\phi), \tag{4.4}$$

$$\cos\theta_{\mathrm{W}} = r\cos\theta_{\mathrm{F}}, \tag{4.5}$$

where θ_{CB} is the CA of water droplets on a rough surface in a CB state, ϕ, as defined in eq.(4.1), is the solid-liquid area fraction to the projected area, θ_{F} is the Young CA of a water droplet on a smooth, flat, rigid, homogeneous, and chemically inert surface, θ_{W} is the CA of water droplets on a rough surface in a W state, and r is the surface roughness factor.

To compare with our experimental data, static water droplet CAs are then theoretically estimated using the CB equation (4.4) and the Young CAs on the flat GS as well as the flat 3D-printed surfaces coated with OTS and CS, i.e., $\theta_{\mathrm{F}} \approx 35°, 123°$ and $135°$, respectively. As shown in Fig. 4.4a, the experimental CAs agree well with the CAs modeled by the CB equation (4.4), revealing that all the studied surfaces wetted in a CB mode with air trapped beneath the drop. Since the valid range of the cosine function is between -1 and 1 and the multiplication of the terms ($r\cos\theta_{\mathrm{F}}$) is either $<$ -1 or $>$ 1, the Wenzel equation is not applicable in our case.

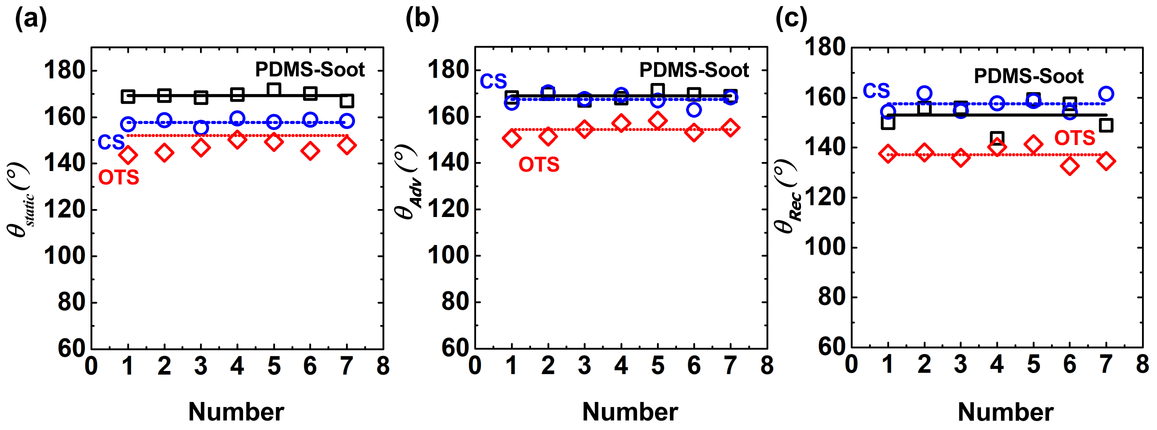

Figure 4.4. Comparison of measured static water droplet CA in (a) and dynamic CAs (in terms of advancing (b) and receding (c)) with Cassie-Baxter theoretical model on glass substrate coated with PDMS-soot (□,━━), 3D-printed microstructures ($r = 2.87$, $\phi = 0.27$) coated with candle soot (CS) (○,- - -), and 3D-printed microstructures coated with OTS (◇,⋯⋯).

In addition to the static water droplet CA, the dynamic CAs (i.e., advancing and receding CAs) and ROAs are measured to evaluate the surface adhesion. Fig. 4.4 b-c shows water droplet advancing and receding CAs on the three types of SH surfaces fabricated. The average advancing CA and the standard deviation of seven water droplets on the TSH surface was about $\theta_{\text{Adv}} \simeq 168.9\pm1.4^\circ$, which is close to that on the 3D-microstructured surface coated with CS, $\theta_{\text{Adv}} \simeq 167.4 \pm 2.5^\circ$. While the advancing CA on the 3D-microstructured surface coated with OTS was around $\theta_{\text{Adv}} \simeq 154.3 \pm 2.6^\circ$, which is lower than the former by approximately $\sim 13^\circ$. The average receding CAs were also measured to be large, as illustrated in Fig. 4.3 and Fig. 4.4c.

The measured advancing and receding CAs of water droplets on the studied surfaces were consistent with the theoretical prediction using the CB equation due to the presence of air pockets between water droplets and surface cavities. Furthermore, the ROAs of both the 3D-printed microstructured surface coated with CS and the GS surface coated with PDMS-soot were extremely low, $\theta_{Roll} \lesssim 5^\circ$, which makes them great candidates for self-cleaning and water repellent applications. The 3D-printed microstructures coated with OTS, however, showed a higher ROA approximately $\theta_{Roll} > 15^\circ$, which makes the droplet adhere more to the surface.

4.3.2 Method Reproducibility for Mass Production

For the tests of reproducibility and mass production, six more samples were fabricated and evaluated by measuring the static, dynamic (in terms of the advancing and receding) CAs, and ROAs (the static CA showed in Fig. 4.5). All the samples showed superhydrophobic behavior with a large CA and a low ROA, and the results agree well with the previous ones. From the agreeable results of the seven samples, we confirmed the reproducibility of these methods to obtain robust SH surfaces that can be mass production using a 3D printing technology. These superhydrophobic surfaces fabricated enable a stable CB wetting for a water droplet and can benefit various applications such as self-cleaning and drag-reduction.

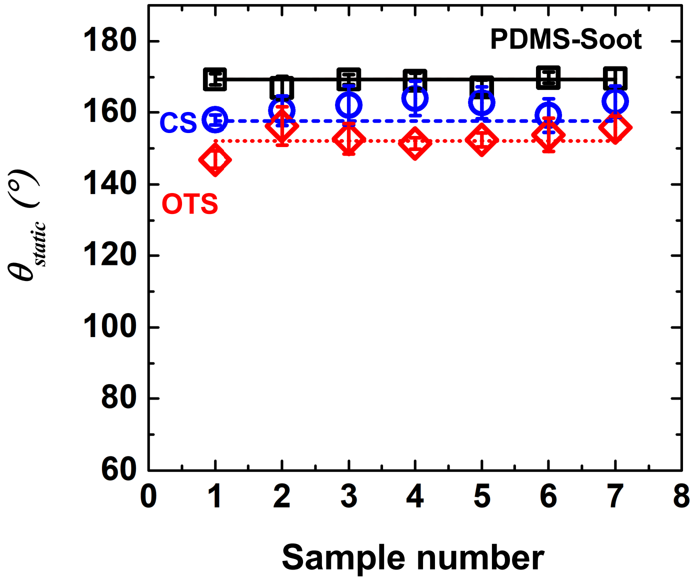

Figure 4.5. Comparison of the measured static water droplet CA and Cassie-Baxter theoretical model on glass substrate coated with PDMS-soot (□,▬), 3D-printed microstructures ($r = 2.87$, $\phi = 0.27$) coated with candle soot (CS) (○,- - -), and 3D-printed microstructures coated with OTS (◇,⋯⋯) for seven different samples. The error bar represents the standard deviation of seven droplets on each surface.

4.4 Conclusions

In summary, superhydrophobic surfaces are facilely obtained using simple one and two-step fabricating processes. For the former, a transparent SH surface was created via an only single heating process of PDMS at 350° for 4 h, by depositing PDMS-soot on the GS. The surface obtained using this method showed great superhydrophobicity and super-repellency properties with an ultrahigh CA and ultra-low ROA. The latter, two-step method was composed of, first, 3D-printed microstructured surface and, second, a hydrophobic coating using either CS or OTS. The 3D-printed microstructures coated with CS showed better superhydrophobic properties with a high static water CA and low ROA, compared to those with OTS coating. This reveals that additional nano-roughness from the candle shoot (on top of hydrophobic MS) enhances the non-wetting property or superhydrophobicity greatly. In terms of applications, a water droplet exhibits a spherical shape on the GS coated with PDMS-soot and 3D-printed CS surfaces, which can be easily rolled-off by incline the surface few degrees to remove dirt or contaminants in their way. Finally, we provide here promising facile, cost-effective, and highly efficient fabrication strategies for preparing transparent super-repellent and superhydrophobic surfaces using a 3D-printing technique by incorporating a thermodynamic model. The method provided is capable of a large-scale production and can be applied widely in the applications of self-cleaning and super-repellent materials in the fields of surface engineering and material.

Chapter 5

Conclusions and Outlook

In this work, the wetting and evaporation of pure water and aqueous surfactant solutions have been investigated on superhydrophobic surfaces of a variety of geometric parameters and structures.

The wetting state, evaporation dynamics, and contact line movement of evaporating water droplets on SH nanograss surfaces with an extremely low $\phi \approx 5\%$ were experimentally elucidated. Different from that evaporating drops can form either CB or Wenzel state, depending on r and ϕ, on more regular SH micro- or nano-structured pillars, all small droplets on SH NG surfaces formed a gas-trapping CB wetting state and evaporated in a constant contact angle mode for most of the droplet lifetime. Besides, beneficial to various applications, the SH nanograss surfaces delay the CB to Wenzel Wetting transition to a later time at $0.9t_f$. In contrast to smaller drops, stick-slip motions of the contact line were observed for the first time, for large droplets of initial drop size of $D_0 \approx 4.2$ mm on SH nanograss surfaces. This jumping motion is attributed to the excess free energy (of $O(10^{-8}Jm^{-1})$) available in the system, due to the change in the droplet shape and contact angle, and hence the contact line movement when θ reaches θ_r. Finally, the classical vapor-diffusion model slightly overpredicts the water evaporation rate on SH nanograss surfaces with a low CAH and smaller contact area, while the evaporative cooling effect could better predict the evaporation rate.

A possible extension of this work could be, experiments with water and nanoparticle droplets of different sizes and materials on nanograss SH surfaces of different ϕ and r and analyze the contact line movement or mobility during the evaporation process. Also, it is of interest to investigate the mechanism leading to the stick-slip motion of the contact line of large droplets in comparison to small droplets depending on the change of ϕ and r.

We experimentally measured the contact angles and wetting states of DDAB surfactant-laden drops for nine different concentrations on two superhydrophobic microstructures of different packing-fraction (ϕ) and surface roughness (r). A model considering surfactant adsorption at the LV and SL interfaces has been derived and compared to these experimental data. The experimental data and the theoretical predictions of the CB contact angles were in good agreement. However, the theoretical prediction using a modified W equation didn't predict well the Wenzel contact angles for both surfaces, likely due to the pinning effects of the wetting contact line. We further consider thermodynamic surface energies to predict the stability or metastability of the wetting states depending on C_{S}. We found that the Wenzel state is thermodynamically favorable for both SH surfaces at all DDAB concentrations, but there is a free energy barrier between the CB and W states for $C_{\mathrm{S}} \leq 0.25$ for our SH surfaces. This thermodynamic analysis implies that the CB state is metastable at these concentrations, and this metastable CB state becomes more stable on surfaces with greater ϕ and r. Based on the free energy barrier and the adsorption thermodynamics for surfactant-laden drops, we highlight the prediction of a stable and robust gas-trapping, CB state superhydrophobic microstructures beneficial for various applications of self-cleaning and low-friction, when meeting the following two criteria: first, a large Young contact angle of a surfactant-laden drop on the flat surface: $\theta_{\mathrm{Y}}(C_{\mathrm{S}}) > 90°$ and, second, large values of r and ϕ which satisfy $\cos\theta_{\mathrm{Y}}(C_{\mathrm{S}}) < (\frac{\phi-1}{r-\phi})$.

For the future investigation, it is very interesting to develop a theory explaining the contact angle and wetting state for Wenzel droplets with respect to surfactant concentration C_{S} in terms of ϕ and r by including the pinning effect of the contact line. Also, the critical concentration after which the wetting state is switching from CB to Wenzel during droplet evaporation can be investigated for different types of surfactants.

Finally, superhydrophobic surfaces facilely obtained using simple one and two-step fabricating processes. For the former, a transparent SH surface was created via an only single heating process of PDMS at 350° for 4 h while partially depositing the PDMS-soot on the GS. The surface obtained using this method showed great superhydrophobicity and super-repellency properties with an ultrahigh CA and ultra-low ROA. While the latter two-step method was composed of first 3D-printed of the microstructured surface, before being coated with either CS or OTS hydrophobic coating. Both the prepared 3D-printed microstructures coated with CS showed superhydrophobic properties with high static water CA and low ROA. While the 3D-printed microstructure coated with OTS solution showed a lower static CA and a higher ROA of $\theta_{Roll} > 15°$, reveals that the prepared surface modified using OTS solution is more sticky. The water droplets exhibited spherical shape on the GS coated with PDMS-soot and 3D-printed CS surfaces, which can be easily rolled-off by incline the surface few degrees to remove any dirt or contaminants in their way. All these methods are simple, cost-effective, and highly efficient processes. The processes, design principle, and contact angle measurements presented here are useful for preparing transparent and superhydrophobic surfaces with additive manufacturing, which enables large-scale production and promisingly expands the application scope of utilizing self-cleaning superhydrophobic materials.

A possible extension of this work could be 3D-print surfaces of various geometric arrangements using high-temperature resistant resin, which is useful to generate Leidenfrost droplets for drop impact experiments. Moreover, it is of interest to investigate the mechanism leading to the formation of a thin-air layer beneath the spherical drops in terms of the surface structure, resin material, and the liquid material.

Also, it is of interest to use the thermodynamic theory to design robust superhydrophobic substrates of different geometric arrangements such as mushroom-shaped microstructures with overhanging caps and subsequently printing them using 3D-printing techniques and study their stability by applying mechanical stress, such as shear stress. Since many studies reported Cassie-Baxter to Wenzel transition, it is of interest to develop new methods for investigating Wenzel to Cassie-Baxter transition on these surfaces.

Another topic of interest is to coat the superhydrophobic surfaces fabricated here with an infused lubricant such as Krytox, which has low surface energy as well as low working temperature and to investigate the wetting properties, evaporation, and drop impact dynamics on these surfaces. Also, the test of the repellent-properties of these lubricant infused surfaces could be expanded to all liquids (organic or inorganic, polar or nonpolar, Newtonian or non-Newtonian).

References

[1] Robert D Deegan, Olgica Bakajin, Todd F Dupont, Greg Huber, Sidney R Nagel, and Thomas A Witten. Contact line deposits in an evaporating drop. *Phys. Rev. E*, 62(1):756, 2000.

[2] Suk Tai Chang and Orlin D Velev. Evaporation-induced particle microseparations inside droplets floating on a chip. *Langmuir*, 22(4):1459–1468, 2006.

[3] G. Ciasca, L. Businaro, M. Papi, A. Notargiacomo, M. Chiarpotto, A. De Ninno, V. Palmieri, S. Carta, E. Giovine, A. Gerardino, and M. De Spirito. Self-assembling of large ordered dna arrays using superhydrophobic patterned surfaces. *Nanotechnology*, 24(49):495302, 2013.

[4] Paul Calvert. Inkjet printing for materials and devices. *Chem. Mater.*, 13(10):3299–3305, 2001.

[5] JungAh Lim, WiHyoung Lee, Donghoon Kwak, and Kilwon Cho. Evaporation-induced self-organization of inkjet-printed organic semiconductors on surface-modified dielectrics for high-performance organic transistors. *Langmuir*, 25(9):5404–5410, 2009.

[6] Enrico Sowade, Thomas Blaudeck, and Reinhard R Baumann. Self-assembly of spherical colloidal photonic crystals inside inkjet-printed droplets. *Cryst. Growth Des.*, 16(2):1017–1026, 2016.

[7] Thomas Young. An essay on the cohesion of fluids. *Philos. Trans. Royal Soc.*, 95:65–87, 1805.

[8] Robert N Wenzel. Resistance of solid surfaces to wetting by water. *Ind. Eng. Chem.*, 28(8):988–994, 1936.

[9] ABD Cassie and S Baxter. Wettability of porous surfaces. *J. Chem. Soc. Faraday Trans.*, 40:546–551, 1944.

[10] Charles W Extrand and Y Kumagai. Liquid drops on an inclined plane: the relation between contact angles, drop shape, and retentive force. *Journal of colloid and interface science*, 170(2):515–521, 1995.

[11] David Quéré. Non-sticking drops. *Reports Prog. Phys.*, 68(11):2495, 2005.

[12] Neil J Shirtcliffe, Sanaa Aqil, Carl Evans, Glen McHale, Michael I Newton, Carole C Perry, and Paul Roach. The use of high aspect ratio photoresist (su-8) for super-hydrophobic pattern prototyping. *J. Micromech. Microeng.*, 14(10):1384, 2004.

[13] Peichun Tsai, Rob GH Lammertink, Matthias Wessling, and Detlef Lohse. Evaporation-triggered wetting transition for water droplets upon hydrophobic microstructures. *Phys. Rev. Lett.*, 104(11):116102, 2010.

[14] Adrien Bussonniére, Masoud B Bigdeli, Di-Yen Chueh, Qingxia Liu, Peilin Chen, and Peichun Amy Tsai. Universal wetting transition of an evaporating water droplet on hydrophobic micro-and nano-structures. *Soft matter*, 13(5):978–984, 2017.

[15] Chieko Ishino, Ko Okumura, and David Quéré. Wetting transitions on rough surfaces. *EPL*, 68(3):419–425, 2004.

[16] Wei Gong, Yingqing Zu, Sheng Chen, and Yuying Yan. Wetting transition energy curves for a droplet on a square-post patterned surface. *Sci. Bull.*, 62(2):136 – 142, 2017.

[17] Choongyeop Lee and Chang-Jin Kim. Underwater restoration and retention of gases on superhydrophobic surfaces for drag reduction. *Phys. Rev. Lett.*, 106(1):014502, 2011.

[18] Rosa Poetes, Kathrin Holtzmann, Kristian Franze, and Ullrich Steiner. Metastable underwater superhydrophobicity. *Phys. Rev. Lett.*, 105(16):166104, 2010.

[19] Aurélie Lafuma and David Quéré. Superhydrophobic states. *Nat. Mater.*, 2(7):457–460, 2003.

[20] CW Extrand and Y Kumagai. An experimental study of contact angle hysteresis. *J.*

Colloid Interface Sci., 191(2):378–383, 1997.

[21] Anandi Krishnan, Yi-Hsiu Liu, Paul Cha, Roger Woodward, David Allara, Erwin A Vogler, et al. An evaluation of methods for contact angle measurement. *Colloids Surf. B*, 43(2):95–98, 2005.

[22] Yang Lin, Ran Zhou, and Jie Xu. Superhydrophobic surfaces based on fractal and hierarchical microstructures using two-photon polymerization: toward flexible superhydrophobic films. *Adv. Mater. Interfaces*, 5(21):1801126, 2018.

[23] Xi Zhang, Feng Shi, Jia Niu, Yugui Jiang, and Zhiqiang Wang. Superhydrophobic surfaces: from structural control to functional application. *J. Mater. Chem.*, 18(6):621–633, 2008.

[24] Tomohiro Onda, Satoshi Shibuichi, Naoki Satoh, and Kaoru Tsujii. Super-water-repellent fractal surfaces. *Langmuir*, 12(9):2125–2127, 1996.

[25] Lei Jiang, Yong Zhao, and Jin Zhai. A lotus-leaf-like superhydrophobic surface: a porous microsphere/nanofiber composite film prepared by electrohydrodynamics. *Angew.Chem.Int.Ed.*, 43(33):4338–4341, 2004.

[26] Zhiqing Yuan, Hong Chen, and Jide Zhang. Facile method to prepare lotus-leaf-like super-hydrophobic poly (vinyl chloride) film. *Appl. Surf. Sci.*, 254(6):1593–1598, 2008.

[27] Vassilia Zorba, Emmanuel Stratakis, Marios Barberoglou, Emmanuel Spanakis, Panagiotis Tzanetakis, Spiros H Anastasiadis, and Costas Fotakis. Biomimetic artificial surfaces quantitatively reproduce the water repellency of a lotus leaf. *Adv. Mater.*, 20(21):4049–4054, 2008.

[28] Yonghao Xiu, Yan Liu, Dennis W Hess, and CP Wong. Mechanically robust superhydrophobicity on hierarchically structured si surfaces. *Nanotechnology*, 21(15):155705, 2010.

[29] Yongjoo Kwon, Neelesh Patankar, Junkyu Choi, and Junghoon Lee. Design of surface hierarchy for extreme hydrophobicity. *Langmuir*, 25(11):6129–6136, 2009.

[30] Pavel A Levkin, Frantisek Svec, and Jean MJ Fréchet. Porous polymer coatings: a versatile approach to superhydrophobic surfaces. *Adv. Funct. Mater.*, 19(12):1993–

1998, 2009.

[31] Se-Jin Choi and Sung-Yoon Huh. Direct structuring of a biomimetic anti-reflective, self-cleaning surface for light harvesting in organic solar cells. *Macromol. Rapid Commun.*, 31(6):539–544, 2010.

[32] Xiaoyan Song, Jin Zhai, Yilin Wang, and Lei Jiang. Fabrication of superhydrophobic surfaces by self-assembly and their water-adhesion properties. *J. Phys. Chem. B*, 109(9):4048–4052, 2005.

[33] Boaz Pokroy, Sung H Kang, L Mahadevan, and Joanna Aizenberg. Self-organization of a mesoscale bristle into ordered, hierarchical helical assemblies. *Science*, 323(5911):237–240, 2009.

[34] Iurii Sas, Russell E Gorga, Jeff A Joines, and Kristin A Thoney. Literature review on superhydrophobic self-cleaning surfaces produced by electrospinning. *J Polym Sci B Polym Phys*, 50(12):824–845, 2012.

[35] H Bagheri, M Aliofkhazraei, H Mojiri Forooshani, and A Sabour Rouhaghdam. Electrodeposition of the hierarchical dual structured (hds) nanocrystalline ni surface with high water repellency and self-cleaning properties. *J. Taiwan Inst. Chem. Eng.*, 80:883–893, 2017.

[36] Yan Liu, Arnab Das, Ziyin Lin, Ian B Cooper, Ajeet Rohatgi, and CP Wong. Hierarchical robust textured structures for large scale self-cleaning black silicon solar cells. *Nano Energy*, 3:127–133, 2014.

[37] Yuekun Lai, Yuxin Tang, Jiaojiao Gong, Dangguo Gong, Lifeng Chi, Changjian Lin, and Zhong Chen. Transparent superhydrophobic/superhydrophilic tio 2-based coatings for self-cleaning and anti-fogging. *J. Mater. Chem.*, 22(15):7420–7426, 2012.

[38] J Lomga, P Varshney, D Nanda, M Satapathy, SS Mohapatra, and A Kumar. Fabrication of durable and regenerable superhydrophobic coatings with excellent self-cleaning and anti-fogging properties for aluminium surfaces. *J Alloys Compd*, 702:161–170, 2017.

[39] Adel MA Mohamed, Aboubakr M Abdullah, and Nathalie A Younan. Corrosion

behavior of superhydrophobic surfaces: A review. *Arab. J. Chem.*, 8(6):749–765, 2015.

[40] S S Farhadi, M Aliofkhazraei, G h Barati Darband, A Abolhasani, and A Sabour Rouhaghdam. Corrosion and wettability of peo coatings on magnesium by addition of potassium stearate. *J. Magnes. Alloy.*, 5(2):210–216, 2017.

[41] Hongyu Dong, Mengjiao Cheng, Yajun Zhang, Hao Wei, and Feng Shi. Extraordinary drag-reducing effect of a superhydrophobic coating on a macroscopic model ship at high speed. *J. Mater. Chem. A*, 1(19):5886–5891, 2013.

[42] Robert J Daniello, Nicholas E Waterhouse, and Jonathan P Rothstein. Drag reduction in turbulent flows over superhydrophobic surfaces. *Phys. Fluids*, 21(8):085103, 2009.

[43] Liangliang Cao, Andrew K Jones, Vinod K Sikka, Jianzhong Wu, and Di Gao. Anti-icing superhydrophobic coatings. *Langmuir*, 25(21):12444–12448, 2009.

[44] Michael J Kreder, Jack Alvarenga, Philseok Kim, and Joanna Aizenberg. Design of anti-icing surfaces: smooth, textured or slippery? *Nat. Rev. Mater.*, 1(1):15003, 2016.

[45] Alexander Otten and Stephan Herminghaus. How plants keep dry: a physicist's point of view. *Langmuir*, 20(6):2405–2408, 2004.

[46] Gregory D Bixler and Bharat Bhushan. Bioinspired rice leaf and butterfly wing surface structures combining shark skin and lotus effects. *Soft matter*, 8(44):11271–11284, 2012.

[47] Jonathan P Rothstein. Slip on superhydrophobic surfaces. *Annu. Rev. Fluid Mech.*, 42:89–109, 2010.

[48] Lydéric Bocquet and Eric Lauga. A smooth future? *Nat. Mater.*, 10(5):334, 2011.

[49] Elif Karatay, A Sander Haase, Claas Willem Visser, Chao Sun, Detlef Lohse, Pei-chun Amy Tsai, and Rob GH Lammertink. Control of slippage with tunable bubble mattresses. *PNAS*, 110(21):8422–8426, 2013.

[50] Lei Wu, Junping Zhang, Bucheng Li, and Aiqin Wang. Mechanical-and oil-durable superhydrophobic polyester materials for selective oil absorption and oil/water separation. *J. Colloid Interface Sci.*, 413:112–117, 2014.

[51] Liangliang Cao, Tyler P Price, Michael Weiss, and Di Gao. Super water-and oil-

repellent surfaces on intrinsically hydrophilic and oleophilic porous silicon films. *Langmuir*, 24(5):1640–1643, 2008.

[52] Lin Feng, Zhongyi Zhang, Zhenhong Mai, Yongmei Ma, Biqian Liu, Lei Jiang, and Daoben Zhu. A super-hydrophobic and super-oleophilic coating mesh film for the separation of oil and water. *Angew. Chem. Int. Ed.*, 43(15):2012–2014, 2004.

[53] Wenbin Zhang, Zhun Shi, Feng Zhang, Xia Liu, Jian Jin, and Lei Jiang. Superhydrophobic and superoleophilic pvdf membranes for effective separation of water-in-oil emulsions with high flux. *Adv. Mater.*, 25(14):2071–2076, 2013.

[54] J Justin Koh, Gwendolyn JH Lim, Xin Zhou, Xiwen Zhang, Jun Ding, and Chaobin He. 3d-printed anti-fouling cellulose mesh for highly efficient oil/water separation applications. *ACS Appl. Mater. Interfaces*, 11(14):13787–13795, 2019.

[55] Juan Lv, Zhengjun Gong, Zhoukun He, Jian Yang, Yanqiu Chen, Changyu Tang, Yu Liu, Meikun Fan, and Woon-Ming Lau. 3d printing of a mechanically durable superhydrophobic porous membrane for oil–water separation. *J. Mater. Chem. A*, 5(24):12435–12444, 2017.

[56] Mohammad Amin Sarshar, Christopher Swarctz, Scott Hunter, John Simpson, and Chang-Hwan Choi. Effects of contact angle hysteresis on ice adhesion and growth on superhydrophobic surfaces under dynamic flow conditions. *Colloid Polym. Sci.*, 291(2):427–435, 2013.

[57] Yang He, Chengyu Jiang, Hengxu Yin, and Weizheng Yuan. Tailoring the wettability of patterned silicon surfaces with dual-scale pillars: from hydrophilicity to superhydrophobicity. *Appl. Surf. Sci.*, 257(17):7689–7692, 2011.

[58] Michaël Lejeune, Lise Marie Lacroix, Frédéric Brétagnol, Andrea Valsesia, Pascal Colpo, and François Rossi. Plasma-based processes for surface wettability modification. *Langmuir*, 22(7):3057–3061, 2006.

[59] Christian Dorrer and Jüergen Rüehe. Wetting of silicon nanograss: from superhydrophilic to superhydrophobic surfaces. *Adv. Mater.*, 20(1):159–163, 2008.

[60] José Bico, Christian Marzolin, and David Quéré. Pearl drops. *EPL*, 47(2):220, 1999.

[61] Yue Wang, Hong Hu, Jinyou Shao, and Yucheng Ding. Fabrication of well-defined mushroom-shaped structures for biomimetic dry adhesive by conventional photolithography and molding. *ACS Appl. Mater. Interfaces*, 6(4):2213–2218, 2014.

[62] Su Yeon Lee, Yudi Rahmawan, and Shu Yang. Transparent and superamphiphobic surfaces from mushroom-like micropillar arrays. *ACS Appl. Mater. Interfaces*, 7(43):24197–24203, 2015.

[63] Hong Hu, Jinyou Shao, Hongmiao Tian, Xiangming Li, and Chengbao Jiang. Mushroom-shaped micropillars for robust nonwetting surface by electrohydrodynamic structuring technique. *IEEE Trans Nanotechnol*, 15(2):237–242, 2016.

[64] Alberto Baldelli, Ben Bshaden, Alidad Amirfazli, and Dan Sameoto. Reproducibility of superhydrophobic and oleophobic polymeric micro surface topographies. *Surf Topogr-Metrol*, 2020.

[65] Minglin Ma and Randal M Hill. Superhydrophobic surfaces. *Curr. Opin. Colloid Interface Sci.*, 11(4):193–202, 2006.

[66] Dongshi Zhang, Feng Chen, Qing Yang, Jinhai Si, and Xun Hou. Mutual wetting transition between isotropic and anisotropic on directional structures fabricated by femotosecond laser. *Soft Matter*, 7(18):8337–8342, 2011.

[67] Zhonghai Zhang, Yanjie Yu, and Peng Wang. Hierarchical top-porous/bottom-tubular tio2 nanostructures decorated with pd nanoparticles for efficient photoelectrocatalytic decomposition of synergistic pollutants. *ACS Appl. Mater. Interfaces*, 4(2):990–996, 2012.

[68] Jiansheng Feng, Mark T Tuominen, and Jonathan P Rothstein. Hierarchical superhydrophobic surfaces fabricated by dual-scale electron-beam-lithography with well-ordered secondary nanostructures. *Adv. Funct. Mater.*, 21(19):3715–3722, 2011.

[69] Jiale Yong, Qing Yang, Feng Chen, Dongshi Zhang, Guangqing Du, Hao Bian, Jinhai Si, Feng Yun, and Xun Hou. Superhydrophobic pdms surfaces with three-dimensional (3d) pattern-dependent controllable adhesion. *Appl. Surf. Sci.*, 288:579–583, 2014.

[70] Trevor J Snyder, Mike Andrews, Mark Weislogel, Peter Moeck, Jennifer Stone-

Sundberg, Derek Birkes, Madeline Paige Hoffert, Adam Lindeman, Jeff Morrill, Ondrej Fercak, et al. 3d systems' technology overview and new applications in manufacturing, engineering, science, and education. *3D Print Addit Manuf*, 1(3):169–176, 2014.

[71] Lishi Jiao, Zhong Chua, Seung Moon, Jie Song, Guijun Bi, and Hongyu Zheng. Femtosecond laser produced hydrophobic hierarchical structures on additive manufacturing parts. *Nanomaterials*, 8(8):601, 2018.

[72] Xiaolong Wang, Xiaobing Cai, Qiuquan Guo, Tengyuan Zhang, Brad Kobe, and Jun Yang. i3dp, a robust 3d printing approach enabling genetic post-printing surface modification. *ChemComm*, 49(86):10064–10066, 2013.

[73] A Milionis, C Noyes, E Loth, IS Bayer, AW Lichtenberger, VN Stathopoulos, and N Vourdas. Water-repellent approaches for 3-d printed internal passages. *Mater. Manuf. Processes*, 31(9):1162–1170, 2016.

[74] Guijun Li, Xiaoyong Mo, Yilin Wang, Ching-Yuen Chan, and Kang Cheung Chan. All 3d-printed superhydrophobic/oleophilic membrane for robotic oil recycling. *Adv. Mater. Interfaces*, 6(18):1900874, 2019.

[75] Shushan Yuan, Junyong Zhu, Yi Li, Yan Zhao, Jian Li, Peter Van Puyvelde, and Bart Van der Bruggen. Structure architecture of micro/nanoscale zif-l on a 3d printed membrane for a superhydrophobic and underwater superoleophobic surface. *J. Mater. Chem. A*, 7(6):2723–2729, 2019.

[76] Hae-Sung Yoon, Hyun-Taek Lee, Eun-Seob Kim, and Sung-Hoon Ahn. Direct printing of anisotropic wetting patterns using aerodynamically focused nanoparticle (afn) printing. *Appl. Surf. Sci.*, 396:1450–1457, 2017.

[77] Hanneke Gelderblom, Alvaro G Marin, Hrudya Nair, Arie Van Houselt, Leon Lefferts, Jacco H Snoeijer, and Detlef Lohse. How water droplets evaporate on a superhydrophobic substrate. *Phys. Rev. E*, 83(2):026306, 2011.

[78] Moonchan Lee, Wuseok Kim, Sanghee Lee, Seunghyeon Baek, Kijung Yong, and Sangmin Jeon. Water droplet evaporation from sticky superhydrophobic surfaces. *Applied Physics Letters*, 111(2):021603, 2017.

[79] Wei Xu, Rajesh Leeladhar, Yong Tae Kang, and Chang-Hwan Choi. Evaporation kinetics of sessile water droplets on micropillared superhydrophobic surfaces. *Langmuir*, 29(20):6032–6041, 2013.

[80] Rodney Marcelo do Nascimento, Cecile Cottin-Bizonne, Christophe Pirat, and Stella MM Ramos. Water drop evaporation on mushroom-like superhydrophobic surfaces: temperature effects. *Langmuir*, 32(8):2005–2009, 2016.

[81] S Moulinet and D Bartolo. Life and death of a fakir droplet: Impalement transitions on superhydrophobic surfaces. *Eur. Phys. J. E*, 24(3):251–260, 2007.

[82] Daiki Murakami, Hiroshi Jinnai, and Atsushi Takahara. Wetting transition from the cassie–baxter state to the wenzel state on textured polymer surfaces. *Langmuir*, 30(8):2061–2067, 2014.

[83] Zhenhai Pan, Susmita Dash, Justin A Weibel, and Suresh V Garimella. Assessment of water droplet evaporation mechanisms on hydrophobic and superhydrophobic substrates. *Langmuir*, 29(51):15831–15841, 2013.

[84] Susmita Dash and Suresh V Garimella. Droplet evaporation on heated hydrophobic and superhydrophobic surfaces. *Phys. Rev. E*, 89(4):042402, 2014.

[85] Zhenhai Pan, Justin A Weibel, and Suresh V Garimella. Influence of surface wettability on transport mechanisms governing water droplet evaporation. *Langmuir*, 30(32):9726–9730, 2014.

[86] Michele Ferrari and Francesca Ravera. Surfactants and wetting at superhydrophobic surfaces: Water solutions and non aqueous liquids. *Adv. Colloid Interface Sci.*, 161(1-2):22–28, 2010.

[87] Neil J Shirtcliffe, Glen McHale, and Michael I Newton. Wet adhesion and adhesive locomotion of snails on anti-adhesive non-wetting surfaces. *PloS One*, 7(5):e36983, 2012.

[88] AJB Milne, JAW Elliott, and A Amirfazli. Contact angles of surfactant solutions on heterogeneous surfaces. *Phys. Chem. Chem. Phys.*, 17(8):5574–5585, 2015.

[89] Yanqiu Zhu, Yuxia Gao, Chenhui Zhang, Xin Zhao, Yue Ma, and Fengpei Du. Static

and dynamic wetting behavior of tx-100 solution on super-hydrophobic rice (oryza sativa.) leaf surfaces. *Colloids Surf. A Physicochem. Eng. Asp.*, 547:148–156, 2018.

[90] Chenhui Zhang, Xin Zhao, Jinmei Lei, Yue Ma, and Fengpei Du. The wetting behavior of aqueous surfactant solutions on wheat (triticum aestivum) leaf surfaces. *Soft Matter*, 13(2):503–513, 2017.

[91] Nadia Shardt, Masoud Bozorg Bigdeli, Janet AW Elliott, and Peichun Amy Tsai. How surfactants affect droplet wetting on hydrophobic microstructures. *J. Phys. Chem. Lett.*, 10:7510–7515, 2019.

[92] Uwe Thiele, Jacco H Snoeijer, Sarah Trinschek, and Karin John. Equilibrium contact angle and adsorption layer properties with surfactants. *Langmuir*, 34(24):7210–7221, 2018.

[93] Michele Ferrari, Francesca Ravera, Silvia Rao, and Libero Liggieri. Surfactant adsorption at superhydrophobic surfaces. *Appl. Phys. Lett.*, 89(5):053104, 2006.

[94] Michele Ferrari, Francesca Ravera, and Libero Liggieri. Wetting of single and mixed surfactant solutions on superhydrophobic surfaces. *J Adhes Sci Technol*, 23(3):483–492, 2009.

[95] R Mohammadi, J Wassink, and A Amirfazli. Effect of surfactants on wetting of superhydrophobic surfaces. *Langmuir*, 20(22):9657–9662, 2004.

[96] Feng-Ming Chang, Yu-Jane Sheng, Hui Chen, and Heng-Kwong Tsao. From superhydrophobic to superhydrophilic surfaces tuned by surfactant solutions. *Appl. Phys. Lett.*, 91(9):094108, 2007.

[97] Milton J Rosen and Joy T Kunjappu. *Surfactants and interfacial phenomena*. John Wiley & Sons, 2012.

[98] Tharwat F Tadros. *An introduction to surfactants*. Walter de Gruyter, 2014.

[99] Nihar Ranjan Biswal and Santanu Paria. Wetting of ptfe and glass surfaces by aqueous solutions of cationic and anionic double-chain surfactants. *Ind. Eng. Chem. Res.*, 51(30):10172–10178, 2012.

[100] Nihar Ranjan Biswal and Santanu Paria. Interfacial and wetting behavior of natural–

synthetic mixed surfactant systems. *RSC Advances*, 4(18):9182–9188, 2014.

[101] Jason G Kralj, Martin A Schmidt, and Klavs F Jensen. Surfactant-enhanced liquid–liquid extraction in microfluidic channels with inline electric-field enhanced coalescence. *Lab Chip*, 5(5):531–535, 2005.

[102] JH Xu, SW Li, J Tan, YJ Wang, and GS Luo. Controllable preparation of monodisperse o/w and w/o emulsions in the same microfluidic device. *Langmuir*, 22(19):7943–7946, 2006.

[103] JH Xu, GS Luo, SW Li, and GG Chen. Shear force induced monodisperse droplet formation in a microfluidic device by controlling wetting properties. *Lab Chip*, 6(1):131–136, 2006.

[104] Jean-Christophe Baret. Surfactants in droplet-based microfluidics. *Lab Chip*, 12(3):422–433, 2012.

[105] JH Xu, PF Dong, H Zhao, CP Tostado, and GS Luo. The dynamic effects of surfactants on droplet formation in coaxial microfluidic devices. *Langmuir*, 28(25):9250–9258, 2012.

[106] Chao-Hua Xue, Xiao-Jing Guo, Jian-Zhong Ma, and Shun-Tian Jia. Fabrication of robust and antifouling superhydrophobic surfaces via surface-initiated atom transfer radical polymerization. *ACS Appl. Mater. Interfaces*, 7(15):8251–8259, 2015.

[107] SA Kulinich, S Farhadi, K Nose, and XW Du. Superhydrophobic surfaces: are they really ice-repellent? *Langmuir*, 27(1):25–29, 2010.

[108] Jaroslaw Drelich, Emil Chibowski, Dennis Desheng Meng, and Konrad Terpilowski. Hydrophilic and superhydrophilic surfaces and materials. *Soft Matter*, 7(21):9804–9828, 2011.

[109] A Syed, L Mangano, P Mao, J Han, and Y-A Song. Creating sub-50 nm nanofluidic junctions in a pdms microchip via self-assembly process of colloidal silica beads for electrokinetic concentration of biomolecules. *Lab Chip*, 14(23):4455–4460, 2014.

[110] Yuanjin Zhao, Luoran Shang, Yao Cheng, and Zhongze Gu. Spherical colloidal photonic crystals. *Acc. Chem. Res.*, 47(12):3632–3642, 2014.

[111] Manas Ojha, Arya Chatterjee, Frank Mont, EF Schubert, Peter C Wayner Jr, and Joel L Plawsky. The role of solid surface structure on dropwise phase change processes. *Int. J. Heat Mass Transf.*, 53(5-6):910–922, 2010.

[112] Tuan A Nguyen, Marc A Hampton, and Anh V Nguyen. Evaporation of nanoparticle droplets on smooth hydrophobic surfaces: the inner coffee ring deposits. *J. Phys. Chem. C*, 117(9):4707–4716, 2013.

[113] Guangfen Li, Susana Moreno Flores, Chandrasekhar Vavilala, Michael Schmittel, and Karlheinz Graf. Evaporation dynamics of microdroplets on self-assembled monolayers of dialkyl disulfides. *Langmuir*, 25(23):13438–13447, 2009.

[114] Cheng-Yen Lin, Kun-Yi Andrew Lin, Ting-Wei Yang, Ying-Chu Chen, and Hongta Yang. Self-assembled hemispherical nanowell arrays for superhydrophobic antireflection coatings. *J. Colloid Interface Sci.*, 490:174–180, 2017.

[115] Yudi Rahmawan, Lebo Xu, and Shu Yang. Self-assembly of nanostructures towards transparent, superhydrophobic surfaces. *J. Mater. Chem. A*, 1(9):2955–2969, 2013.

[116] Takahiro Koishi, Kenji Yasuoka, Shigenori Fujikawa, Toshikazu Ebisuzaki, and Xiao Cheng Zeng. Coexistence and transition between cassie and wenzel state on pillared hydrophobic surface. *Proc. Natl. Acad. Sci.*, 106(21):8435–8440, 2009.

[117] Peng Cai, Ningning Bai, Lan Xu, Cui Tan, and Qing Li. Fabrication of superhydrophobic wood surface with enhanced environmental adaptability through a solution-immersion process. *Surf. Coatings Technol.*, 277:262–269, 2015.

[118] Ping Guo, Shangru Zhai, Zuoyi Xiao, and Qingda An. One-step fabrication of highly stable, superhydrophobic composites from controllable and low-cost pmhs/teos sols for efficient oil cleanup. *J. Colloid Interface Sci.*, 446:155–162, 2015.

[119] Saara Heinonen, Elina Huttunen-Saarivirta, Juha-Pekka Nikkanen, Mari Raulio, Outi Priha, Jarmo Laakso, Erna Storgårds, and Erkki Levänen. Antibacterial properties and chemical stability of superhydrophobic silver-containing surface produced by sol–gel route. *Colloids Surfaces A Physicochem. Eng. Asp.*, 453:149–161, 2014.

[120] Yong Chae Jung and Bharat Bhushan. Wetting transition of water droplets on super-

hydrophobic patterned surfaces. *Scr. Mater.*, 57(12):1057–1060, 2007.

[121] Bharat Bhushan, Kerstin Koch, and Yong Chae Jung. Nanostructures for superhydrophobicity and low adhesion. *Soft Matter*, 4(9):1799–1804, 2008.

[122] M Reyssat, JM Yeomans, and D Quéré. Impalement of fakir drops. *EPL*, 81(2):26006, 2007.

[123] Carlo Antonini, Jae Bong Lee, Tanmoy Maitra, Sarah Irvine, Dominique Derome, Manish K Tiwari, J Carmeliet, and Dimos Poulikakos. Unraveling wetting transition through surface textures with x-rays: Liquid meniscus penetration phenomena. *Sci. Rep.*, 4:4055, 2014.

[124] Jia Lee, Sung-Hwan Hwang, Sung-Soo Yoon, and Dahl-Young Khang. Evaporation characteristics of water droplets in cassie, wenzel, and mixed states on superhydrophobic pillared si surface. *Colloids Surfaces A Physicochem. Eng. Asp.*, 562:304–309, 2019.

[125] Susmita Dash and Suresh V Garimella. Droplet evaporation dynamics on a superhydrophobic surface with negligible hysteresis. *Langmuir*, 29(34):10785–10795, 2013.

[126] Li Xu, Zhigang Li, and Shuhuai Yao. Directional motion of evaporating droplets on gradient surfaces. *Appl. Phys. Lett.*, 101(6):064101, 2012.

[127] Glen McHale, Sanaa Aqil, NJ Shirtcliffe, MI Newton, and H Yildirim Erbil. Analysis of droplet evaporation on a superhydrophobic surface. *Langmuir*, 21(24):11053–11060, 2005.

[128] Xuemei Chen, Ruiyuan Ma, Jintao Li, Chonglei Hao, Wei Guo, Bing Lam Luk, Shuai Cheng Li, Shuhuai Yao, and Zuankai Wang. Evaporation of droplets on superhydrophobic surfaces: Surface roughness and small droplet size effects. *Physical review letters*, 109(11):116101, 2012.

[129] FengChao Wang and HengAn Wu. Molecular origin of contact line stick-slip motion during droplet evaporation. *Sci. Rep.*, 5:17521, 2015.

[130] Álvaro G Marín, Hanneke Gelderblom, Arturo Susarrey-Arce, Arie van Houselt, Leon Lefferts, Johannes GE Gardeniers, Detlef Lohse, and Jacco H Snoeijer. Building microscopic soccer balls with evaporating colloidal fakir drops. *Proc. Natl. Acad. Sci.*

U.S.A., 109(41):16455–16458, 2012.

[131] Li Zhao, Congcong Hong, Liangxu Lin, Huaping Wu, Yewang Su, Xiaobo Zhang, and Aiping Liu. Controllable nanoscale engineering of vertically aligned mos2 ultrathin nanosheets by nitrogen doping of 3d graphene hydrogel for improved electrocatalytic hydrogen evolution. *Carbon N. Y.*, 116:223–231, 2017.

[132] Vitaliy Kondrashov and Jürgen Rühe. Microcones and nanograss: toward mechanically robust superhydrophobic surfaces. *Langmuir*, 30(15):4342–4350, 2014.

[133] Ville Jokinen, Lauri Sainiemi, and Sami Franssila. Complex droplets on chemically modified silicon nanograss. *Adv. Mater.*, 20(18):3453–3456, 2008.

[134] Kjetil Gjerde, RT Rajendra Kumar, Karin Nordstrøm Andersen, Jakob Kjelstrup-Hansen, Ken BK Teo, William I Milne, Christer Persson, Kristian Mølhave, Horst-Günther Rubahn, and Peter Bøggild. On the suitability of carbon nanotube forests as non-stick surfaces for nanomanipulation. *Soft Matter*, 4(3):392–399, 2008.

[135] Caroline A Schneider, Wayne S Rasband, and Kevin W Eliceiri. Nih image to imagej: 25 years of image analysis. *Nat. Methods*, 9(7):671, 2012.

[136] OI Del Río and AW Neumann. Axisymmetric drop shape analysis: computational methods for the measurement of interfacial properties from the shape and dimensions of pendant and sessile drops. *J. Colloid Interface Sci.*, 196(2):136–147, 1997.

[137] Hartmut Alexander Wege, Juan Antonio Holgado-Terriza, Juan Ignacio Rosales-Leal, Raquel Osorio, Manuel Toledano, and Miguel Ángel Cabrerizo-Vilchez. Contact angle hysteresis on dentin surfaces measured with adsa on drops and bubbles. *Colloids Surfaces A Physicochem. Eng. Asp.*, 206(1-3):469–483, 2002.

[138] M Hoorfar and AW Neumann. Axisymmetric drop shape analysis (adsa) for the determination of surface tension and contact angle. *J. Adhes.*, 80(8):727–743, 2004.

[139] SA Kulinich and M Farzaneh. Effect of contact angle hysteresis on water droplet evaporation from super-hydrophobic surfaces. *Appl. Surf. Sci.*, 255(7):4056–4060, 2009.

[140] Martin ER Shanahan. Simple theory of" stick-slip" wetting hysteresis. *Langmuir*, 11(3):1041–1043, 1995.

[141] CW Extrand and AN Gent. Retention of liquid drops by solid surfaces. *Journal of Colloid and Interface Science*, 138(2):431–442, 1990.

[142] DW Pilat, P Papadopoulos, D Schaffel, Doris Vollmer, Rüdiger Berger, and H-J Butt. Dynamic measurement of the force required to move a liquid drop on a solid surface. *Langmuir*, 28(49):16812–16820, 2012.

[143] E Bormashenko, A Musin, G Whyman, and M Zinigrad. Wetting transitions and depinning of the triple line. *Langmuir*, 28(7):3460–3464, 2012.

[144] MER Shanahan and K Sefiane. Kinetics of triple line motion during evaporation. *Contact angle, wettability and adhesion*, 6:19–31, 2009.

[145] SMM Ramos, JF Dias, and Bruno Canut. Drop evaporation on superhydrophobic ptfe surfaces driven by contact line dynamics. *J. Colloid Interface Sci.*, 440:133–139, 2015.

[146] Yuri O Popov. Evaporative deposition patterns: spatial dimensions of the deposit. *Phys. Rev. E*, 71(3):036313, 2005.

[147] Tuan AH Nguyen, Anh V Nguyen, Marc A Hampton, Zhi Ping Xu, Longbin Huang, and Victor Rudolph. Theoretical and experimental analysis of droplet evaporation on solid surfaces. *Chem. Eng. Sci.*, 69(1):522–529, 2012.

[148] Sam Dehaeck, Alexey Rednikov, and Pierre Colinet. Vapor-based interferometric measurement of local evaporation rate and interfacial temperature of evaporating droplets. *Langmuir*, 30(8):2002–2008, 2014.

[149] Florian Carle, Benjamin Sobac, and David Brutin. Experimental evidence of the atmospheric convective transport contribution to sessile droplet evaporation. *Appl. Phys. Lett.*, 102(6):061603, 2013.

[150] Jang Ung Park, Matt Hardy, Seong Jun Kang, Kira Barton, Kurt Adair, Deep Kishore Mukhopadhyay, Chang Young Lee, Michael S. Strano, Andrew G. Alleyne, John G. Georgiadis, Placid M. Ferreira, and John A. Rogers. High-resolution electrohydrodynamic jet printing. *Nat. Mater.*, 6(10):782, 2007.

[151] Lu Tie, Zhiguang Guo, Yongmin Liang, and Weimin Liu. Water super-repellent behavior of semicircular micro/nanostructured surfaces. *Nanoscale*, 11(8):3725–3732,

2019.

[152] Huaping Wu, Kunpeng Jiang, Zhenxiong Xu, Sihang Yu, Xiang Peng, Zheng Zhang, Hao Bai, Aiping Liu, and Guozhong Chai. Theoretical and experimental studies on the controllable pancake bouncing behavior of droplets. *Langmuir*, 35(52):17000–17008, 2019.

[153] Ying-Song Yu, Xianfu Huang, Li Sun, Jin-Zhi Zhou, and An Zhou. Evaporation of ethanol/water mixture droplets on micro-patterned pdms surfaces. *Int. J. Heat Mass Transf.*, 144:118708, 2019.

[154] AJB Milne, JAW Elliott, Parham Zabeti, Jiyan Zhou, and A Amirfazli. Model and experimental studies for contact angles of surfactant solutions on rough and smooth hydrophobic surfaces. *Phys. Chem. Chem. Phys.*, 13(36):16208–16219, 2011.

[155] Bu-Yao Zhu and Tiren Gu. General isotherm equation for adsorption of surfactants at solid/liquid interfaces. part 1. theoretical. *J. Chem. Soc., Faraday Trans. 1*, 85(11):3813–3817, 1989.

[156] E Pierce, FJ Carmona, and A Amirfazli. Understanding of sliding and contact angle results in tilted plate experiments. *Colloids Surf. A Physicochem. Eng. Asp.*, 323(1-3):73–82, 2008.

[157] Brendan ML Koch, A Amirfazli, and Janet AW Elliott. Wetting of rough surfaces by a low surface tension liquid. *J. Phys. Chem. C*, 118(41):23777–23782, 2014.

[158] Brendan ML Koch, A Amirfazli, and Janet AW Elliott. Modeling and measurement of contact angle hysteresis on textured high-contact-angle surfaces. *J. Phys. Chem. C*, 118(32):18554–18563, 2014.

[159] Josiah Willard Gibbs. On the equilibrium of heterogeneous substances. *Am. J. Sci.*, 16(96):441–458, 1878.

[160] CA Ward and Eugene Levart. Conditions for stability of bubble nuclei in solid surfaces contacting a liquid-gas solution. *J. Appl. Phys.*, 56(2):491–500, 1984.

[161] Janet AW Elliott and Ovidiu Voitcu. On the thermodynamic stability of liquid capillary bridges. *Can. J. Chem. Eng.*, 85(5):692–700, 2007.

[162] Fatemeh Eslami and Janet AW Elliott. Thermodynamic investigation of the barrier for heterogeneous nucleation on a fluid surface in comparison with a rigid surface. *J. Phys. Chem. B*, 115(36):10646–10653, 2011.

[163] Leila Zargarzadeh and Janet AW Elliott. Comparative surface thermodynamic analysis of new fluid phase formation between a sphere and a flat plate. *Langmuir*, 29(11):3610–3627, 2013.

[164] José Bico, Uwe Thiele, and David Quéré. Wetting of textured surfaces. *Colloids Surf. A Physicochem. Eng. Asp.*, 206(1-3):41–46, 2002.

[165] AJB Milne and A Amirfazli. The cassie equation: How it is meant to be used. *Adv. Colloid Interface Sci.*, 170(1-2):48–55, 2012.

[166] Katarzyna Szymczyk, Anna Zdziennicka, Joanna Krawczyk, and Bronisław Jańczuk. Wettability, adhesion, adsorption and interface tension in the polymer/surfactant aqueous solution system. i. critical surface tension of polymer wetting and its surface tension. *Colloids Surf. A Physicochem. Eng. Asp.*, 402:132–138, 2012.

[167] Minglin Ma, Malancha Gupta, Zhi Li, Lei Zhai, Karen K Gleason, Robert E Cohen, Michael F Rubner, and Gregory C Rutledge. Decorated electrospun fibers exhibiting superhydrophobicity. *Adv. Mater.*, 19(2):255–259, 2007.

[168] Lin Feng, Shuhong Li, Yingshun Li, Huanjun Li, Lingjuan Zhang, Jin Zhai, Yanlin Song, Biqian Liu, Lei Jiang, and Daoben Zhu. Super-hydrophobic surfaces: from natural to artificial. *Adv. Mater.*, 14(24):1857–1860, 2002.

[169] Yongmei Zheng, Xuefeng Gao, and Lei Jiang. Directional adhesion of superhydrophobic butterfly wings. *Soft Matter*, 3(2):178–182, 2007.

[170] Yiming Liu, Jingwei Chen, Dawei Guo, Moyuan Cao, and Lei Jiang. Floatable, self-cleaning, and carbon-black-based superhydrophobic gauze for the solar evaporation enhancement at the air–water interface. *ACS Appl. Mater. Interfaces*, 7(24):13645–13652, 2015.

[171] Neil J Shirtcliffe, Glen McHale, Michael I Newton, Carole C Perry, and Paul Roach. Superhydrophobic to superhydrophilic transitions of sol–gel films for temperature,

alcohol or surfactant measurement. *Mater. Chem. Phys.*, 103(1):112–117, 2007.

[172] Yung-Lang Yang, Chin-Chi Hsu, Tien-Li Chang, Long-Sheng Kuo, and Ping-Hei Chen. Study on wetting properties of periodical nanopatterns by a combinative technique of photolithography and laser interference lithography. *Appl. Surf. Sci.*, 256(11):3683–3687, 2010.

[173] Tuan D Ngo, Alireza Kashani, Gabriele Imbalzano, Kate TQ Nguyen, and David Hui. Additive manufacturing (3d printing): A review of materials, methods, applications and challenges. *Compos. B. Eng.*, 143:172–196, 2018.

[174] Gustav Graeber, Oskar B Martin Kieliger, Thomas M Schutzius, and Dimos Poulikakos. 3d-printed surface architecture enhancing superhydrophobicity and viscous droplet repellency. *ACS Appl. Mater. Interfaces*, 10(49):43275–43281, 2018.

[175] Yang Yang, Xiangjia Li, Xuan Zheng, Zeyu Chen, Qifa Zhou, and Yong Chen. 3d-printed biomimetic super-hydrophobic structure for microdroplet manipulation and oil/water separation. *Adv. Mater.*, 30(9):1704912, 2018.

[176] Kyong-Min Lee, Hani Park, Jihun Kim, and Doo-Man Chun. Fabrication of a superhydrophobic surface using a fused deposition modeling (fdm) 3d printer with poly lactic acid (pla) filament and dip coating with silica nanoparticles. *Appl. Surf. Sci.*, 467:979–991, 2019.

[177] Shushan Yuan, Dieter Strobbe, Jean-Pierre Kruth, Peter Van Puyvelde, and Bart Van der Bruggen. Super-hydrophobic 3d printed polysulfone membranes with a switchable wettability by self-assembled candle soot for efficient gravity-driven oil/water separation. *J. Mater. Chem. A*, 5(48):25401–25409, 2017.

[178] Zhoukun He, Yanqiu Chen, Jian Yang, Changyu Tang, Juan Lv, Yu Liu, Jun Mei, Woon-ming Lau, and David Hui. Fabrication of polydimethylsiloxane films with special surface wettability by 3d printing. *Compos. B. Eng.*, 129:58–65, 2017.

[179] Mengying Long, Shan Peng, Xiaojun Yang, Wanshun Deng, Ni Wen, Kai Miao, Gongyun Chen, Xinrui Miao, and Wenli Deng. One-step fabrication of non-fluorinated transparent super-repellent surfaces with tunable wettability functioning in both air

and oil. *ACS Appl. Mater. Interfaces*, 9(18):15857–15867, 2017.

[180] J Bico, C Tordeux, and D Quéré. Rough wetting. *EPL*, 55(2):214–220, 2001.

[181] Kuan-Yu Yeh, Li-Jen Chen, and Jeng-Yang Chang. Contact angle hysteresis on regular pillar-like hydrophobic surfaces. *Langmuir*, 24(1):245–251, 2008.

[182] H Yildirim Erbil and C Elif Cansoy. Range of applicability of the wenzel and cassie-baxter equations for superhydrophobic surfaces. *Langmuir*, 25(24):14135–14145, 2009.

[183] B Majhy, R Iqbal, and AK Sen. Facile fabrication and mechanistic understanding of a transparent reversible superhydrophobic–superhydrophilic surface. *Sci. Rep.*, 8(1):1–11, 2018.

[184] Feng Zhang, Zhenwu Shi, Yingjie Jiang, Chengyun Xu, Zhuhui Wu, Yanyan Wang, and Changsi Peng. Fabrication of transparent superhydrophobic glass with fibered-silica network. *Appl. Surf. Sci.*, 407:526–531, 2017.

[185] Liji Xiao, Weiguo Zeng, Guangfu Liao, Changfeng Yi, and Zushun Xu. Thermally and chemically stable candle soot superhydrophobic surface with excellent self-cleaning properties in air and oil. *ACS Appl. Nano Mater.*, 1(3):1204–1211, 2018.

[186] R Iqbal, B Majhy, and AK Sen. Facile fabrication and characterization of a pdms-derived candle soot coated stable biocompatible superhydrophobic and superhemophobic surface. *ACS Appl. Mater. Interfaces*, 9(36):31170–31180, 2017.

[187] Li-Yu Lin, Hyun-Joon Kim, and Dae-Eun Kim. Wetting characteristics of zno smooth film and nanowire structure with and without ots coating. *Appl. Surf. Sci.*, 254(22):7370–7376, 2008.

[188] Y Song, R Premachandran Nair, M Zou, and YA Wang. Adhesion and friction properties of micro/nano-engineered superhydrophobic/hydrophobic surfaces. *Thin Solid Films*, 518(14):3801–3807, 2010.

[189] Hosung Yang, Kwanwoo Shin, Giyoong Tae, and Sushil K Satija. Structure of a monolayer of poly (ethylene glycol) end-capped with a fluoroalkyl group and its relationship with protein adsorption at the aqueous interface. *Soft matter*, 5(14):2731–2737, 2009.

[190] Pierre-Gilles De Gennes, Françoise Brochard-Wyart, and David Quéré. *Capillarity*

and wetting phenomena: drops, bubbles, pearls, waves. Springer Science & Business Media, 2013.

[191] Ansys Fluent et al. Ansys fluent 12.0 user's guide. *Ansys Inc*, 15317:1–2498, 2009.

[192] Rulon E Johnson and Robert H Dettre. Contact angle hysteresis: I. study of an idealized rough surface. *Adv. Chem.*, 43:112–135, 1964.

[193] Weiqing Ren. Wetting transition on patterned surfaces: transition states and energy barriers. *Langmuir*, 30(10):2879–2885, 2014.

[194] Pierre-Gilles De Gennes. Wetting: statics and dynamics. *Rev. Mod. Phys.*, 57(3):827, 1985.

Appendix A

Additional data and analysis for "Evaporation Dynamics of Water Droplets on Superhydrophobic Nanograss Surfaces"

A.1 SEM images of the Superhydrophobic nanograss surfaces

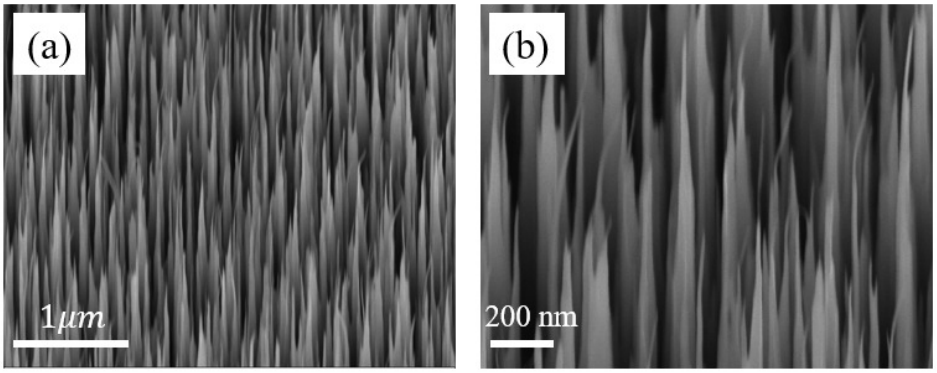

Figure A.1. SEM Image of superhydrophobic nanograss (NG) surface using different magnifications. The length bars here are 1 μm and 200 nm in (a) and (b), respectively.

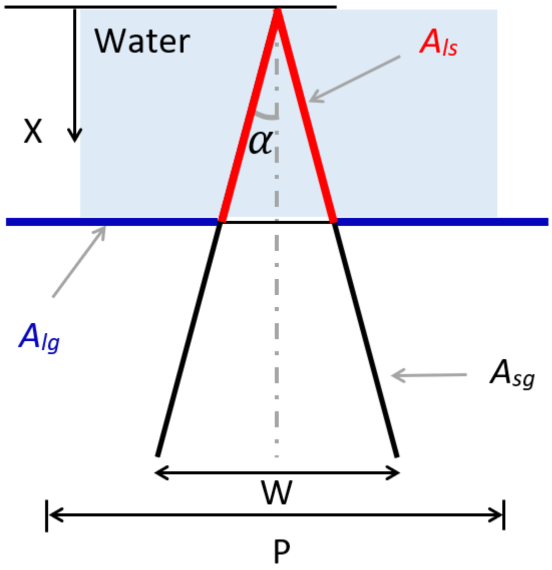

Figure A.2. Side-view of one nanograss unit cell. Here, α is the half cone angle and w is the grass width, P is the unit cell width of the unit cell, and x is the penetration depth of the liquid phase. Figure inspired from Ref. [59].

Figure A.1 shows scanning electron microscope (SEM) images of the SH nanograss surfaces used, with different magnifications. By image analysis of the SEM images, we measured the average cone angle (2α) of a nanograss to be $= 16°$ and estimated the width of single nanograss, w, and the period of the unit cell of a nano-cone, P (see Fig. A.2) to obtain consistent values for the nanograss surface parameters. More specifically, we estimated the solid fraction, ϕ, and the surface roughness, r, for nanograss SH surfaces, using the model proposed by Dorrer et al. (2008) [59], described below.

For regular micro/nano-pillars one can calculate ϕ and r using their conventional definitions with well-defined values of P, w, and H (pillar height). For nanograss-shaped surfaces, however, since the drops can easily impale between the nano-cone, one needs to estimate the water penetration depth, x, first. We estimated the solid fraction, ϕ, and the surface roughness, r, for nanograss SH surfaces, using the model proposed by Dorrer et al. (2008) [59]. This model approximates the nanograss structures with nano-cones, and the geometry of a single cone is shown in Fig. A.2. The nanocone/nanograss geometry is characterized by a half cone angle, α, the width of single nanocone/nanograss, w, and width of the unit cell,

P. The model is based on the change in the interfacial energy of the system to compute the penetration depth, x, of the liquid inside the nanograss-liked structure.

To estimate the penetration depth (x) of water drops inside the surface roughness, they first computed the change in the interfacial energy of the system, dG, with an incremental water penetration, dx:

$$dG(x) = \gamma_{lg} dA_{lg}(x) + \gamma_{ls} dA_{ls}(x) + \gamma_{sg} dA_{sg}(x), \tag{A.1}$$

where $\gamma_{lg}, \gamma_{ls}, \gamma_{sg}$ are the surface tensions at the liquid-gas, liquid-solid, and solid-gas interfaces, respectively; $dA_{lg}(x), dA_{ls}(x), dA_{sg}(x)$ are the change in the liquid-gas, liquid-solid, and solid-gas interfacial areas with respect to the change in x, respectively. By using the Young's equation [7] based on a force balance: $\gamma_{sg} = \gamma_{sl} + \gamma_{lg} \cos\theta$, eq. (A.1) reduces to:

$$dG(x) = \gamma_{lg} dA_{lg}(x) - \gamma_{lg} \cos\theta dA_{ls}(x). \tag{A.2}$$

The interfacial areas of A_{lg} and A_{ls}, described in eq. (A.6)–(A.7) below, are a function of x, and so are dA_{lg} and dA_{lg}.

The penetration of the drop into the nanocones is appropriately assumed to be driven by the Laplace pressure across the liquid-air interface [190]: $\Delta P_L = \frac{2\gamma_{lg}}{R}$ since the effect of gravity on the impalement can be neglected. The negligible effect of gravity is justified based on the following estimation: for a drop with a radius of 1 mm and $\gamma_{lg} = 72\ mN/m$, $\Delta P_L = 144$ Pa. Whereas, the hydrostatic pressure (ΔP_h) exerted by a liquid drop with a 2 mm in height is computed to be $\Delta P_h = 19.6$ Pa, which is smaller than the Laplace pressure by one order of magnitude approximately so it is plausible to neglect the gravity effect. Therefore, the penetration of water drop into the nanocone/nanograss surface can be primarily attributed to the Laplace pressure inside the drop, and it can be estimated using a force balance resulting in a change of interfacial energy due to an incremental change of x:

$$\frac{dG(x)}{dx} = \Delta P A_{lg}(x). \tag{A.3}$$

By solving eq. (A.3), the penetration depth, x, can be computed as [59]:

$$-2\pi x \gamma_{lg} \left(\frac{\cos\theta \tan\alpha}{\cos\alpha} - \tan^2\alpha \right) = \frac{2\gamma_{lg}}{R} (P^2 - \pi \tan^2\ \alpha x^2), \tag{A.4}$$

where x is the penetration depth, γ_{lg} is the liquid-gas surface tension, α is the half of the cone angle, R is the radii of curvature, w is the cell width, and θ is the advancing angle on the flat SH coating since the meniscus is moving down into the nanograss structure and assumed to be $\theta = 107°$, which is an average value of common hydrophobic coating, such as flat PDMS and saline coating.

Once penetration depth (x) is calculated, the solid fraction of the drop on nanograss-liked SH surfaces can be estimated using the following conventional definition:

$$\phi = \frac{A_{ls}}{A_{ls} + A_{lg}}, \tag{A.5}$$

where A_{ls} and A_{lg} are the surface area of the liquid-solid and liquid-air interfaces, respectively. Both areas are related to the penetration depth by which the meniscus advances into the nanograss surface, x, via the following equations based on geometric relations for a nano-cone:

$$A_{ls}(x) = \pi \frac{\tan\alpha}{\cos\alpha} x^2, \tag{A.6}$$

and

$$A_{lg}(x) = P^2 - \pi \tan^2 \alpha x^2. \tag{A.7}$$

By using the surface roughness (r) definition, which equals the total surface area (A_T) divided by the projected surface area on 2D plane (A_P) (i.e., the 2D unit-cell area) of the rough surface, we can estimate the roughness of nanograss-SH surfaces, as follows:

$$r = \frac{A_T}{A_P} = \frac{\pi \frac{\tan\alpha}{\cos\alpha} x^2 + P^2 - \frac{\pi w^2}{4}}{P^2}, \tag{A.8}$$

where w is the nano-cone width. In our calculation, we used $R = 1$ mm, $\gamma_{lg} = 72$ mN/m, $\alpha = 8°$, $w = 2$ μm, and $P = 62.5 \pm 6.5$ μm. The latter values of w and P are estimated from the SEM image analysis and by obtaining a consistent value for the critical contact angle at the CB to W wetting transition, θ_c, which is theoretically predicted as $\theta_c = 165.6° \pm 1.4°$, theoretically modelled with $\cos\theta_c = \frac{\phi - 1}{r - \phi}$ [14] and experimentally measured to be $\theta_c = 166° \pm 1.5°$ in the current study. With these parameters, our estimated values are $x = 20.3 \pm 4.2$ μm for penetration depth, $\phi = 0.05 \pm 0.01$ for the solid fraction, and $r = 1.05 \pm 0.01$ for nanograss surface roughness.

A.2 Critical Contact Angle and Contact Diameter at the CB to W transition

During droplet evaporation, the transition from a Cassie-Baxter to Wenzel wetting state was observed at the near end of the droplet lifetime, i.e., $t \approx 0.94\ t_f$. This transition is accompanied by a slight increase in the contact base-diameter (D_b), as shown in Fig. 2 b in the main paper for four independent droplets. The Laplace pressure is calculated using the Young-Laplace [190] for water drop: $\Delta P = \frac{2\gamma}{R_c}$, where γ is the surface tension at the liquid-air interface, and R_c is the radii of curvature. The corresponding time (t/t_f), critical angle (θ_{CB-W}), and base diameter for the CB to W transition are measured and reported in Table A.1.

Table A.1

Experimental data of water droplet sizes at the critical CB to W wetting transition (reported in Fig. 2b in the main paper), with the initial contact angle (θ_0), initial free drop diameter (D_0), initial base diameter (D_b), and the Laplace pressure (ΔP_0) corresponding to the initial (0) state. While reported in the second half of the table are the dimensionless evaporation time (t/t_f) divided by the final time, t_f, CB-W contact angle (θ_{CB-W}), CB-W free drop diameter (D_{CB-W}), CB-W base diameter ($D_{b_{CB-W}}$), and the Laplace pressure (ΔP_{CB-W}) corresponding to CB-Wenzel (CB-W) transition states of water droplets on SH nanograss surfaces.

Data	θ_0 (°)	D_0 (mm)	D_{b_0} (mm)	ΔP_0 (Pa)	t/t_f	θ_{CB-W} (°)	D_{CB-W} (mm)	$D_{b_{CB-W}}$ (mm)	ΔP_{CB-W} (Pa)
Black (■)	165.4	2.85	1.58	101.5	0.89	155.6	0.95	0.44	305.3
Blue (▲)	164.3	2.49	1.27	116.1	0.91	153.4	0.76	0.37	382.6
Red (•)	165.2	2.57	1.35	112.6	0.96	131.9	0.62	0.49	469.4
Purple (▼)	167.9	2.51	1.23	115.3	0.98	114.4	0.49	0.49	591.4

Table A.2

Change in the excess free energy per unit length of contact line for five slips during the evaporation of four independent large water droplets of $D_0 \approx 4.2$ mm on SH Nanograss surface, as shown in Fig.3 a-b in the main paper.

Line	θ_0 $(^\circ)$	θ_B $(^\circ)$	θ_A $(^\circ)$	$\delta\theta$ $(^\circ)$	r_B (mm)	r_A (mm)	δr (mm)	$\delta\tilde{G}$ $(J\ m^{-1})$
Black (■)	166	153	162.8	9.8	1.14	1.025	0.114	2.6×10^{-8}
	166	144	158.1	14.1	0.85	0.68	0.170	7.9×10^{-8}
Red (●)	160	146	158.4	12.4	0.83	0.69	0.143	5.2×10^{-8}
Blue (▲)	164	151	162.2	11.2	1.35	1.19	0.159	8.6×10^{-8}
Pink (◂)	166	156	168.4	12.4	0.48	0.41	0.070	2.9×10^{-8}

A.3 Stick-Slip motion of the contact line for larger droplets

For large droplets, stick-slip motions of the three phase contact line were observed and the excess free energy cause this motion is calculated using the model proposed by Shanahan [140], $\delta\tilde{G}$:

$$\delta\tilde{G} \approx \frac{\gamma \sin^2\theta_0 (2 + \cos\theta_0)(\delta r)^2}{2r}, \tag{A.9}$$

where γ is the surface tension at the liquid-air interface, θ_0 is the initial equilibrium contact angle of the surface, δr is the slipped distance local to the stick-slip event, and r is local pinned contact radius before the triple line slips. In our calculation, we have used $\gamma = 72$ mN/m, and all the symbols in Table S2 are defined as follows: θ_B is the contact angle before each slip, θ_A is the contact angle after each slip, which is close to the initial contact angle (θ_0), $\delta\theta$ is the change in the contact angle before and after the slip, r_B is the base radius before each slip, r_A is the base radius after each slip, δr is the slipped distance local to the stick-slip event, and $\delta\tilde{G}$ is excess free energy per unit length associated with the contact line movement. The receding contact angle for nanograss SH surfaces is measured, $\theta_r = 156.9^\circ \pm 1.2^\circ$ with a sessile drop method, by slowly decreasing the drop volume and measuring the contact angle once the contact line starts to recede. These results are summarized in Table A.2.

A.4 Calculation of evaporation mass flux

The evaporation rate of a sessile of water droplet on a flat substrate can be estimated using an analytical model based on pure diffusive process of water vapour, proposed by Popov [146]. In this model, droplet evaporation is assumed to be quasi-steady (which means that the total evaporation time is much larger than the water-vapour diffusion time) and the evaporation process is governed only by vapor diffusion through the surrounding air. The overall evaporation rate is calculated as [146]:

$$\dot{m} = \frac{dm}{dt} = -\pi R_b D(c_s - c_\infty) f(\theta), \tag{A.10}$$

where

$$f(\theta) = \frac{\sin\theta}{1+\cos\theta} + 4\int_0^\infty \frac{1+\cosh 2\theta\tau}{\sinh 2\pi\tau} \tanh[(\pi-\theta)\tau] d\tau. \tag{A.11}$$

To calculate dimensionless mass flux rate, $\dot{M}$, eq. (A.10) is divide by $R_b D(c_s - c_\infty)$:

$$|\dot{M}| = \frac{\dot{m}}{R_b D(c_s - c_\infty)}. \tag{A.12}$$

Following eq. (A.11), dimensionless mass flux rate, $\dot{M}$, depends on $f(\theta)$:

$$|\dot{M}| = \frac{dM}{dt} = -\pi f(\theta), \tag{A.13}$$

where R_b is the droplet base radius, D is the vapor diffusion coefficient, c_s is the saturated vapor concentration at the surface, c_∞ is the vapor concentration away from the droplet, θ is the contact angle between the solid surface and the droplet, and m is the droplet mass. The experiments were performed under 22 °C and 26% relative humidity (RH). Fluid properties under these conditions are listed in the table below:

Besides the vapor-diffusion-based model, Pan et al. [85] performed a numerical study to estimate the evaporation rate based on both vapor-diffusion and evaporative cooling transport mechanisms for a 2-μL evaporating water droplet as a function of contact angle. In their study, a 2D axisymmetric, quasi-steady model is developed to describe the heat and mass transport within and surrounding the evaporating droplets, and the evaporative cooling is included as an energy sink at the interface. Coupled mass and heat transfer are

Table A.3

Fluid properties.

Properties	*Water*
Temperature T (°C)	22
Relative humidity RH (%)	26
Density ρ (kg/m^3)	996.67
Diffusion coefficient D (m^2/s)	24.59×10^{-6}
Saturated vapor concentration at the droplet surface c$_s$ (kg/m^3)	1.94×10^{-2}
Vapor concentration away from the droplet c$_\infty$ (kg/m^3)	0.26 × c$_s$

also solved throughout the substrate, droplet, and gas domains. The ambient temperature was chosen as $21°C$ with 29% relative humidity. The numerical solution is obtained using the pressure-based finite volume scheme, and the software package ANSYS 12.0 (FLUENT solver) [191] is employed in their simulation. The counteracting effect of the two transport mechanisms (evaporative cooling and vapor-diffusion) as a function of the contact angle is revealed by three different regimes. In regime I. (small CA $\leqslant 60°$), gas-phase natural convection enhances evaporation, and the pure diffusion-based model would underestimate the overall evaporation rate. In regime II. (intermediate CA: $60° \leqslant$ CA $\leqslant 90°$), gas-phase convection and evaporative cooling counterbalance, which allows good prediction of the overall evaporation rate from the vapor-diffusion-based model for this range of θ. In regime III. (high CA ≥ 90°), evaporative cooling suppresses the evaporation rate, and the diffusion-based model overestimates the overall evaporation rate. Based on these three regimes found, they provide a correction curve compared to vapor-diffusion model depending on the contact angle [85], and we multiplied the correction curve to the vapor-diffusion model (black dashed line), described by eq. (A.11)–(A.13), to plot the vapor diffusion-evaporative cooling model (solid black line) in Fig. 4 in the main text.

Appendix B

Additional data and analysis for "Effect of a Cationic Surfactant on Droplet Wetting on Superhydrophobic Surfaces"

B.1 Contact angle data of surfactant-laden droplets on Flat hydrophobic and Superhydrophobic surfaces

Here we report the detailed contact angle measurements of a DDAB-laden droplet on both flat PDMS and two types of SH surfaces, S1 ($r = 2.31$, $\phi = 0.34$) and S2 ($r = 1.33$, $\phi = 0.08$), for nine different DDAB concentrations, and for ten droplets on each surface. On the one hand, for the higher-r SH S1, droplets were in a CB state for $C_{\mathrm{S}} \leq 0.25$ CMC and in a W state for $C_{\mathrm{S}} \geq 0.5$ CMC. On the other, both a CB and W state could appear for droplets on the lower-r SH S2 for $C_{\mathrm{S}} \leq 0.75$ CMC, while all the surfactant-laden droplets were in a W state for $C_{\mathrm{S}} = 1$ CMC.

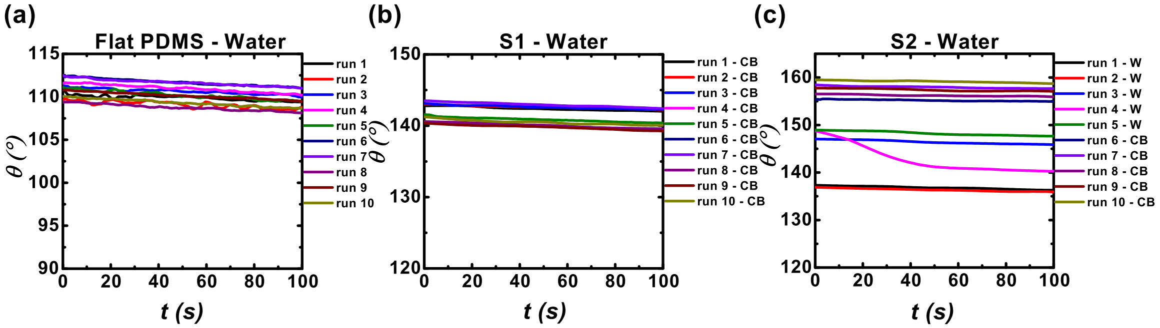

Figure B.1. Contact angle measurements for a pure-water droplet on (a) Flat PDMS, (b) SH S1 ($r = 2.31$, $\phi = 0.34$), and (c) SH S2 ($r = 1.33$, $\phi = 0.08$) surfaces during a period of 100s right after the droplet deposition.

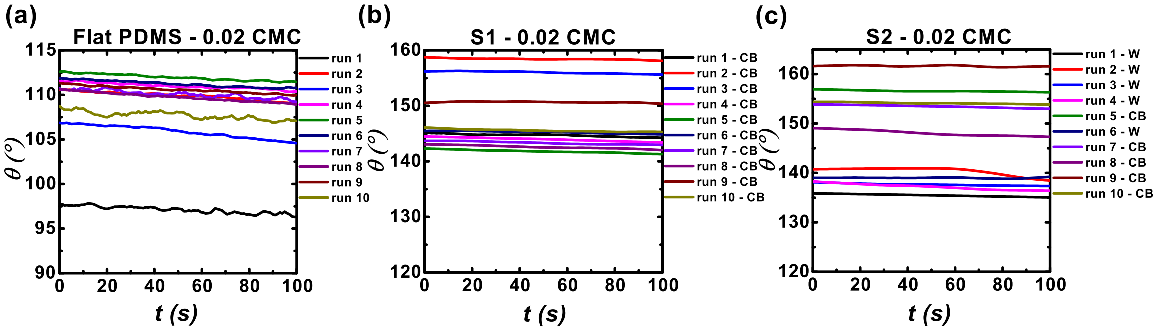

Figure B.2. Contact angle measurements for 0.02 CMC-DDAB droplet on (a) Flat PDMS, (b) SH S1 ($r = 2.31$, $\phi = 0.34$), and (c) SH S2 ($r = 1.33$, $\phi = 0.08$) surfaces during a period of 100s right after the droplet deposition.

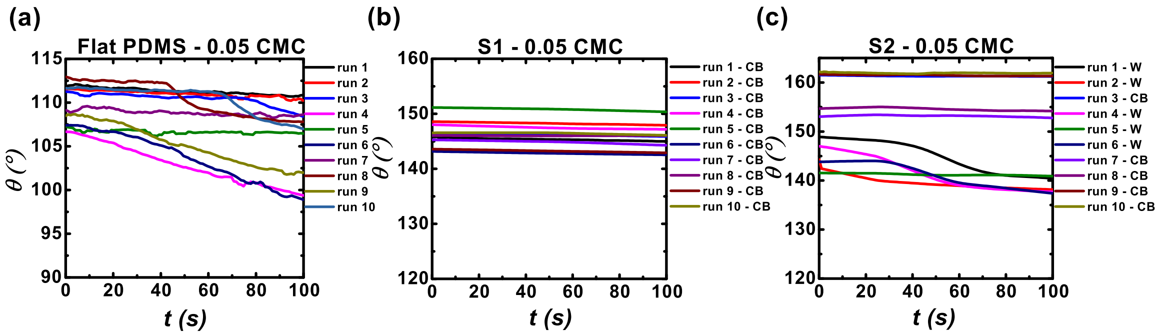

Figure B.3. Contact angle measurements for 0.05 CMC-DDAB droplet on (a) Flat PDMS, (b) SH S1 ($r = 2.31$, $\phi = 0.34$), and (c) SH S2 ($r = 1.33$, $\phi = 0.08$) surfaces during a period of 100s right after the droplet deposition.

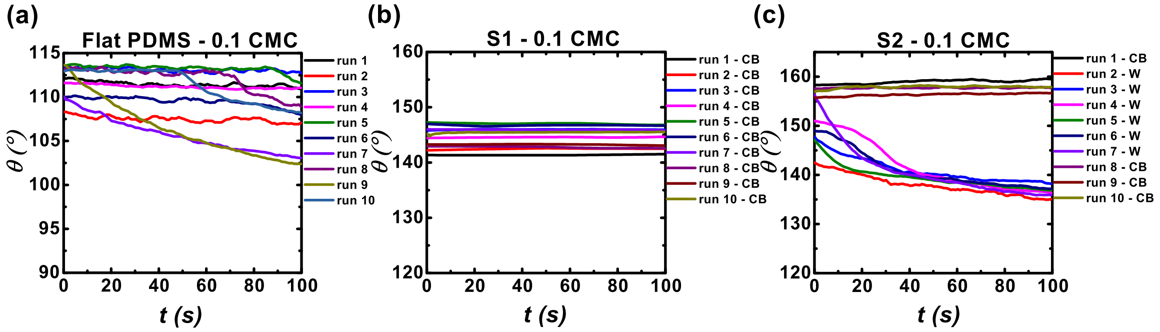

Figure B.4. Contact angle measurements for 0.1 CMC-DDAB droplet on (a) Flat PDMS, (b) SH S1 ($r = 2.31$, $\phi = 0.34$), and (c) SH S2 ($r = 1.33$, $\phi = 0.08$) surfaces during a period of 100s right after the droplet deposition.

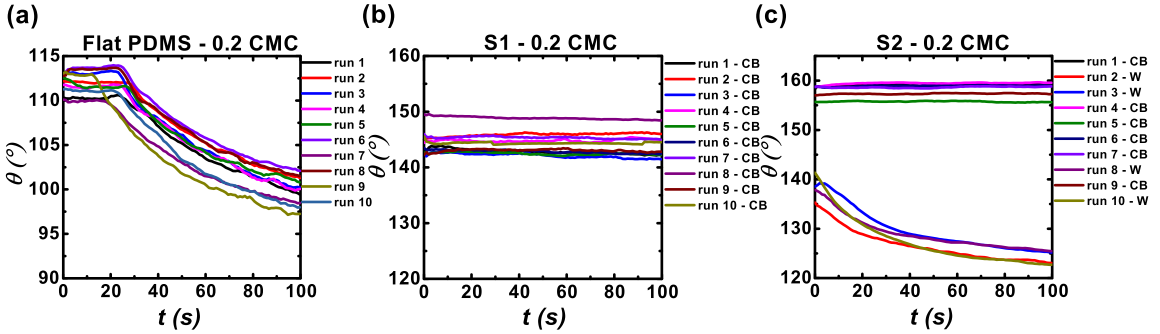

Figure B.5. Contact angle measurements for 0.2 CMC-DDAB droplet on (a) Flat PDMS, (b) SH S1 ($r = 2.31$, $\phi = 0.34$), and (c) SH S2 ($r = 1.33$, $\phi = 0.08$) surfaces during a period of 100s right after the droplet deposition.

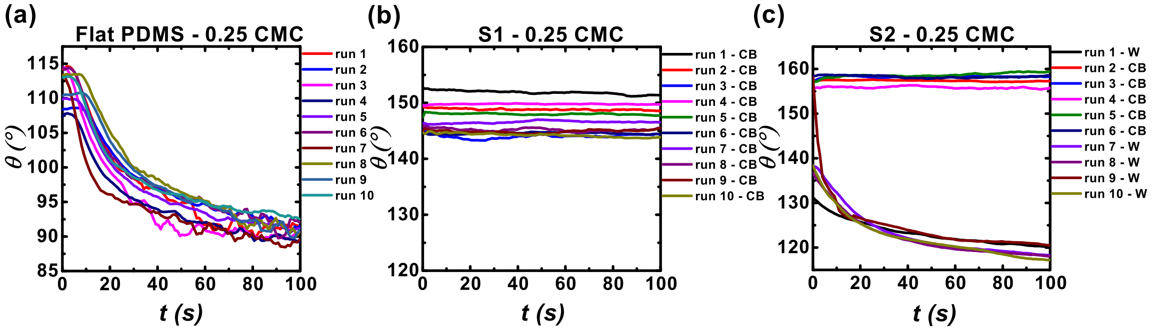

Figure B.6. Contact angle measurements for 0.25 CMC-DDAB droplet on (a) Flat PDMS, (b) SH S1 ($r = 2.31$, $\phi = 0.34$), and (c) SH S2 ($r = 1.33$, $\phi = 0.08$) surfaces during a period of 100s right after the droplet deposition.

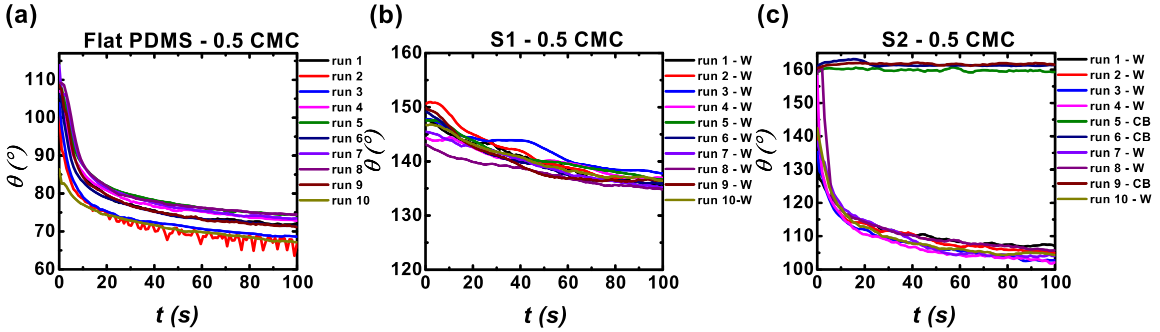

Figure B.7. Contact angle measurements for 0.5 CMC-DDAB droplet on (a) Flat PDMS, (b) SH S1 ($r = 2.31$, $\phi = 0.34$), and (c) SH S2 ($r = 1.33$, $\phi = 0.08$) surfaces during a period of 100s right after the droplet deposition.

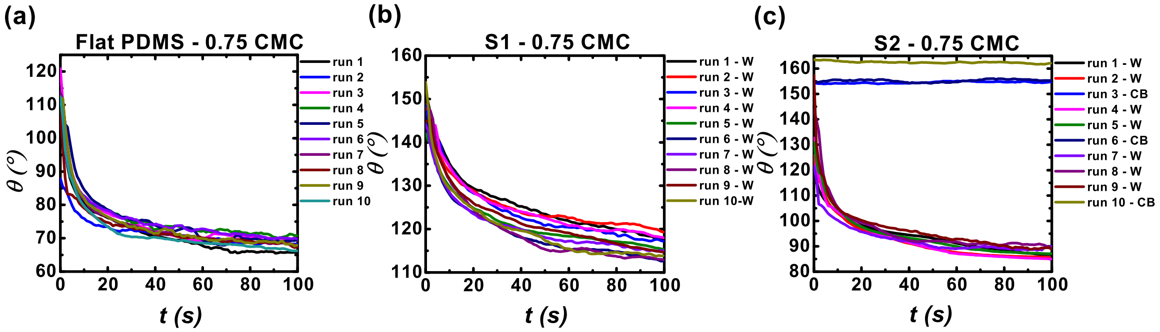

Figure B.8. Contact angle measurements for 0.75 CMC-DDAB droplet on (a) Flat PDMS, (b) SH S1 ($r = 2.31$, $\phi = 0.34$), and (c) SH S2 ($r = 1.33$, $\phi = 0.08$) surfaces during a period of 100s right after the droplet deposition.

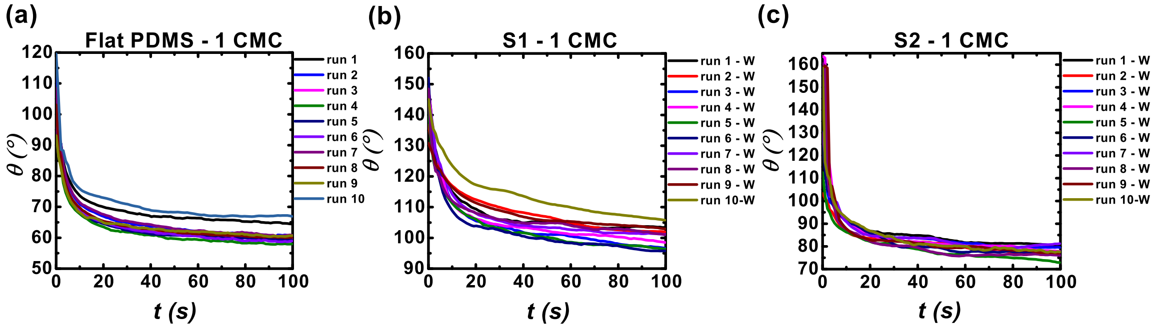

Figure B.9. Contact angle measurements for 1 CMC-DDAB droplet on (a) Flat PDMS, (b) SH S1 ($r = 2.31$, $\phi = 0.34$), and (c) SH S2 ($r = 1.33$, $\phi = 0.08$) surfaces during a period of 100s right after the droplet deposition.

B.2 Fitting of wetting data from Flat PDMS surfaces to determine liquid-vapor and solid-liquid adsorption coefficients

To account for the adsorption fitting parameters for LV and SL interfaces, we first use the Zhu–Gu adsorption isotherm [155] at the LV interface. We extracted LV interfacial tension, $\gamma_{\mathrm{LV}}(C_{\mathrm{S}})$, for DDAB aqueous solution droplets at the studied concentrations from two studies by Biswal-Paria [99, 100] and subsequently used the averaged values for our analysis. Fig.B.10 shows a gradual decrease in the LV interfacial tension with increasing DDAB concentration. The best fit of eq. (3) in the main text to the data is also shown in Fig.B.10. The fit was obtained using MATLAB's curve fitting 'cftool'. To solve the singularity at $\ln(C_{\mathrm{S}}) \to -\infty$, a pure water interfacial tension (γ^0_{LV}) was used as a fitting parameter.

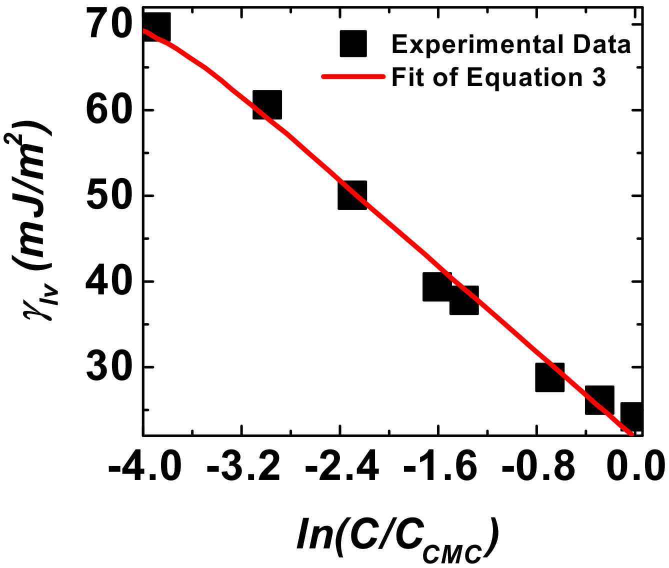

Figure B.10. Liquid-vapor (LV) interfacial tension vs. DDAB concentration in natural logarithmic scale (C/C_{CMC}). The experimental data (■) is the average LV interfacial tension from two studies [99, 100]. The line is the best fit of eq. (3) in the main text to the experimental data. The fitting parameters obtained include: $\Gamma^{\infty}_{\mathrm{LV}} = 4.679 \times 10^{-6}$ mol$/m^2$, $n_{\mathrm{LV}} = 1.235$, $K_{\mathrm{LV}} = 191.5$, and $\gamma^0_{\mathrm{LV}} = 72.2\ mJ/m^2$, with the goodness of fitting parameters, SSE (Sum Squared Error): 6.879×10^{-6} , $R^2 : 0.9652$, adjusted-$R^2 : 0.9512$, and RMSE (Root Mean Square Error): $1.173 \times 10^{-3} J/m^2$.

The best fitting parameters obtained include: $\Gamma_{\mathrm{LV}}^{\infty} = 4.679 \times 10^{-6}\ mol/m^2$, $n_{\mathrm{LV}} = 1.235$, $K_{\mathrm{LV}} = 191.5$, and $\gamma_{\mathrm{LV}}^{0} = 72.2\ mJ/m^2$, with goodness of fit parameters, SSE (Sum Squared Error): 6.879×10^{-6}, $R^2 : 0.9652$, adjusted-$R^2 : 0.9512$, and RMSE (Root Mean Square Error):$1.173 \times 10^{-3} J/m^2$. The fitting parameter $\Gamma_{\mathrm{LV}}^{\infty}$ is the maximum surfactant concentration at the liquid–vapor interface, K_{LV} is the adsorption equilibrium constant, and n_{LV} is an empirical fitting parameter.

To account for the surfactant adsorption at the SL interface, we use the Zhu–Gu adsorption isotherm [155] and arrive at the form of Milne et al. [154] modified Young equation, eq. (4) in the main text, which quantifies the contact angle of a drop on a flat and homogeneous surface as a function of surfactant concentration, by assuming no surfactant adsorption at the SV interface. The average contact angles for the first 10 s and last 10 s of a 100 s recording period are shown in Fig. B.11 and B.12, respectively, along with the best fit of eq. (4) in the main text to our data. The fitting was done using the same way as for the LV adsorption parameters and using the previously found values of $\Gamma_{\mathrm{LV}}^{\infty}$, n_{LV}, K_{LV}, and γ_{LV}^{0}. The singularity at $\ln(C_{\mathrm{S}}) \to -\infty$ was solved by using the contact angle for pure water ($C_{\mathrm{S}} = 0$) as a fitting parameter.

The best fitting parameters found for the first 10 s as in Fig.B.11 were: $\Gamma_{\mathrm{SL}}^{\infty} = 2.979 \times 10^{-6} mol/m^2$, $n_{\mathrm{SL}} = 1.171$, $K_{\mathrm{SL}} = 114$, and $\theta_{\mathrm{Y}}^{0} = 110.84°$, with goodness of fit parameters, SSE: 1.803×10^{-3}, $R^2 : 0.9921$, adjusted-R^2: 0.989, and RMSE: 0.01899. The fitting parameters found for the last 10 s as in Fig. B.12 were: $\Gamma_{\mathrm{SL}}^{\infty} = 3.819 \times 10^{-6} mol/m^2$, $n_{\mathrm{SL}} = 1.311$, $K_{\mathrm{SL}} = 188.1$, and $\theta_{\mathrm{Y}}^{0} = 109.43°$, with goodness of fit parameters, SSE: 5.343×10^{-3}, $R^2 : 0.9916$, adjusted-$R^2 : 0.9882$, and RMSE: 0.03269. The fitting parameter of $\Gamma_{\mathrm{SL}}^{\infty}$ is the maximum surfactant concentration at the solid-liquid interface, K_{SL} is the adsorption equilibrium constant, and n_{SL} is an empirical fitting parameter. Based on the fitting parameters, both LV and SL adsorption process are in the same order of magnitude (10^{-6}) and together contribute to decrease θ_Y as C_{S} increases.

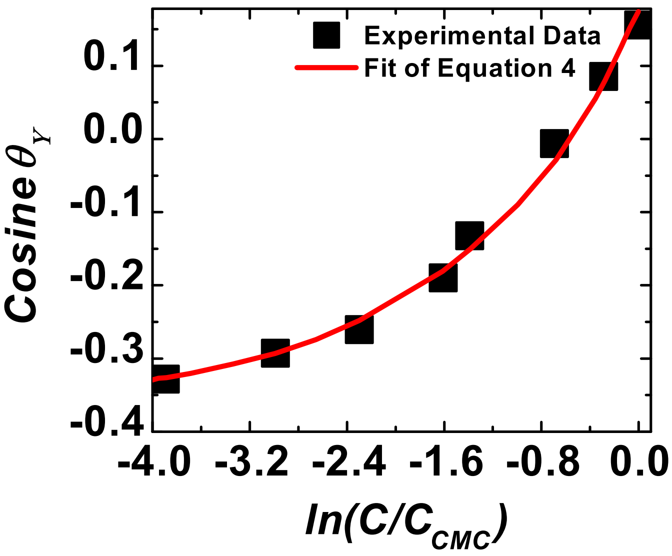

Figure B.11. Cosine of average contact angle on flat PDMS vs. DDAB concentration in natural logarithmic scale (C/C_{CMC}). The experimental contact angle (■) is the average of first 10 s of 100 s recording period. The line is the best fit of eq. (4) in the main text to the experimental data. The fitting parameters are: $\Gamma_{\mathrm{SL}}^{\infty} = 2.979 \times 10^{-6} mol/m^2$, $n_{\mathrm{SL}} = 1.171$, $K_{\mathrm{SL}} = 114$, and $\theta_{\mathrm{Y}}^{0} = 110.84°$, with goodness of fit parameters, SSE: 1.803×10^{-3}, $R^2 : 0.9921$, adjusted-R^2: 0.989, and RMSE: 0.01899.

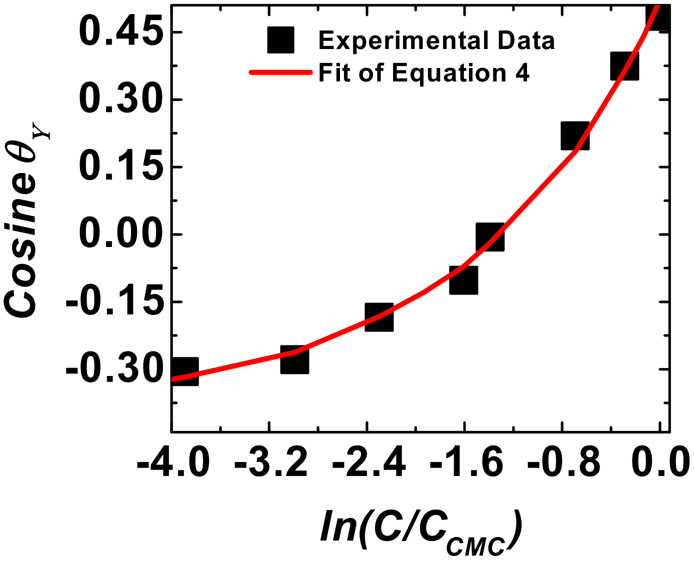

Figure B.12. Cosine of average contact angle on flat PDMS vs. DDAB concentration in natural logarithmic scale (C/C_{CMC}). The experimental contact angle (■) is the average of last 10 s of 100 s recording period. The line is the best fit of eq. (4) in the main text to the experimental data. The fitting parameters are: $\Gamma_{\mathrm{SL}}^{\infty} = 3.819 \times 10^{-6} mol/m^2$, $n_{\mathrm{SL}} = 1.311$, $K_{\mathrm{SL}} = 188.1$, and $\theta_{\mathrm{Y}}^{0} = 109.43°$, with goodness of fit parameters, SSE: 5.343×10^{-3}, R^2 : 0.9916, adjusted-R^2 : 0.9882, and RMSE: 0.03269.

B.3 Free energy derivations for different wetting states

In the derivation, we start from fundamental thermodynamic theories to derive the free energy and finally use this free energy to describe the effect of DDAB-surfactant concentration on a stable Cassie-Baxter and Wenzel wetting state. The free energy analysis of different wetting states of CB and Wenzel was first proposed by Johnson and Dettre [192], and other analyses have been performed for pure liquids on rough surfaces [13, 14, 16, 82, 193]. Here we closely follow the analytical approach of Shardt et al.[91] considering the effect of a surfactant on the free energies of different wetting states. Following Gibbsian composite-system thermodynamics [15, 91, 159, 160, 161, 162, 163], we consider a simplified geometry where the liquid phase has a spherical cap shape (curved), while the SL and SV interfaces are assumed to be flat. We also assume that there are no external forces, such as gravity or pinning/depinning forces at the three phase contact line. According to this approach, the entire system is confined within a movable piston cylinder that interacts with a surrounding reservoir at constant pressure (P^R) and temperature (T^R). The reservoir can exchange energy and volume through the system boundary, but no mass exchange mass with the reservoir since the system is closed. Figure B.13a shows the reference state assumed and in Fig. B.13b a sessile drop with radius R and contact angle θ on a rigid solid. As shown in Fig. B.13b, the assumed system is modeled as two bulk phases (or components). The first component consists of both liquid phase (e.g., water with surfactant) and the vapor phase, and the second component is the solid phase. Using the Gibbsian thermodynamics theory [159], the two phases are separated by a dividing surface that has the following thermodynamic quantities (internal energy, entropy, and moles). The equilibrium conditions of this closed system can be obtained by maximizing the entropy, S, so the differential of the entropy (dS) should equal to zero:

$$\mathrm{d}S^{\mathrm{L}} + \mathrm{d}S^{\mathrm{V}} + \mathrm{d}S^{\mathrm{LV}} + \mathrm{d}S^{\mathrm{S}} + \mathrm{d}S^{\mathrm{SL}} + \mathrm{d}S^{\mathrm{SV}} + \mathrm{d}S^{\mathrm{R}} = 0, \tag{B.1}$$

where the superscripts L, V, LV, S, SL, SV, and R denote the liquid, vapor, liquid-vapor, solid, solid-liquid, solid-vapor, and reservoir phases, respectively.

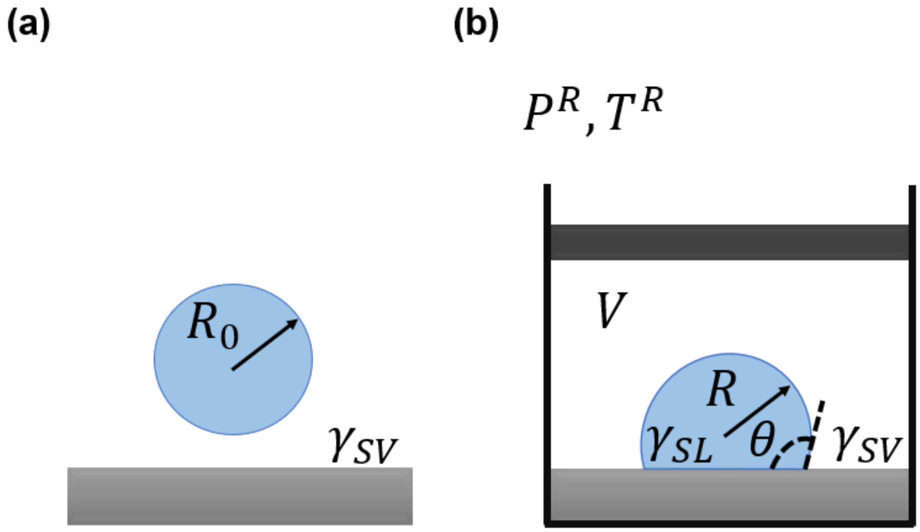

Figure B.13. (a) A Spherical drop without solid-liquid contact is assumed as the reference state. (b) Schematic of a piston-cylinder device in a reservoir containing a liquid drop in the shape of a spherical cap with contact angle θ and radius of curvature R on a rough, chemically homogeneous solid surface (with only component 1) in equilibrium with its vapor (V) and a solid surface (component 2).

Expressions in the differential form of the fundamental equation of thermodynamics of a bulk phase, a flat interface, or a curved interface is given by eqs. (B.2), (B.3), and (B.4), which relate the changes in the internal energies, U due to the changes in the absolute temperature T, volume, V, pressure, P, the area, A, and chemical potential, μ:

$$\mathrm{d}U^{\mathrm{i}} = T^{\mathrm{i}}\mathrm{d}S^{\mathrm{i}} - P^{\mathrm{i}}\mathrm{d}V^{\mathrm{i}} + \sum_{\mathrm{j}=1}^{r} \mu_{\mathrm{j}}^{\mathrm{i}}\mathrm{d}N_{\mathrm{j}}^{\mathrm{i}}, \tag{B.2}$$

$$\mathrm{d}U^{\mathrm{ab}} = T^{\mathrm{ab}}\mathrm{d}S^{\mathrm{ab}} + \gamma^{\mathrm{ab}}\mathrm{d}A^{\mathrm{ab}} + \sum_{\mathrm{j}=1}^{r} \mu_{\mathrm{j}}^{\mathrm{ab}}\mathrm{d}N_{\mathrm{j}}^{\mathrm{ab}}, \tag{B.3}$$

$$\mathrm{d}U^{\mathrm{ab}} = T^{\mathrm{ab}}\mathrm{d}S^{\mathrm{ab}} + \gamma^{\mathrm{ab}}\mathrm{d}A^{\mathrm{ab}} + \sum_{\mathrm{j}=2}^{r} \mu_{\mathrm{j}}^{\mathrm{ab}}\mathrm{d}N_{\mathrm{j}}^{\mathrm{ab}}, \tag{B.4}$$

where i denotes each phase, i.e., liquid, solid, or vapor, j is the phase component, either 1 or 2, N_{j} is the number of moles of component j, γ is the surface tension, and ab denotes each interface, i.e., SL, LV, or SV. To solve the free energy for this system, five constraints are imposed on the system, and we will discuss them below.

Firstly, since the system is closed, there is no mass exchange between the reservoir and the system:

$$\mathrm{d}N_1^{\mathrm{R}} = 0 \qquad \mathrm{d}N_2^{\mathrm{R}} = 0. \tag{B.5}$$

While component 1 can transfer between bulk phases and interfaces of the system,

$$\mathrm{d}N_1^{\mathrm{V}} + \mathrm{d}N_1^{\mathrm{L}} + \mathrm{d}N_1^{\mathrm{S}} + \mathrm{d}N_1^{\mathrm{LV}} + \mathrm{d}N_1^{\mathrm{SV}} + \mathrm{d}N_1^{\mathrm{SL}} + \mathrm{d}N_1^{\mathrm{R}} = 0. \tag{B.6}$$

Secondly, both the reservoir and the system are isolated so that

$$\mathrm{d}U^{\mathrm{V}} = -\ \mathrm{d}U^{\mathrm{R}} - \mathrm{d}U^{\mathrm{S}} - \mathrm{d}U^{\mathrm{L}} - \mathrm{d}U^{\mathrm{SL}} - \mathrm{d}U^{\mathrm{SV}} - \mathrm{d}U^{\mathrm{LV}}. \tag{B.7}$$

Thirdly, the system can exchange volume with the reservoir through the movable piston so

$$\mathrm{d}V^{\mathrm{R}} = -\ \mathrm{d}V^{\mathrm{V}} - \mathrm{d}V^{\mathrm{S}} - \mathrm{d}V^{\mathrm{L}}. \tag{B.8}$$

Fourthly, the solid surface is assumed to be rigid (incompressible) means that no volume changes happen in the solid:

$$\mathrm{d}V^{\mathrm{S}} = 0. \tag{B.9}$$

Finally, the solid surface is considered nonvolatile means that component 2 can only transfer between the solid phase and the SL and SV interfaces:

$$\mathrm{d}N_2^{\mathrm{S}} = -\ \mathrm{d}N_2^{\mathrm{SL}} - \mathrm{d}N_2^{\mathrm{SV}}. \tag{B.10}$$

Based on the“Gibbs dividing surface” approach, the excess surface quantity (component 2) is assumed to be zero for the flat SL and SV interfaces, which means:

$$\mathrm{d}N_2^{\mathrm{SL}} = 0 \qquad \mathrm{d}N_2^{\mathrm{SV}} = 0 \quad \rightarrow \quad \mathrm{d}N_2^{\mathrm{S}} = 0. \tag{B.11}$$

Also, it is worth mentioning here that for any increase or decrease in the SV interface area, there is an equivalent decrease or increase of the SL interfacial area: $A^{\mathrm{SV}} = -A^{\mathrm{SL}}$.

The volume of the spherical cap of the liquid drop, V^{L}, (shown in Fig. B.13b) and areas for the LV and SL interfaces (A^{LV} and A^{SL}, respectively) can be written in terms of the radius of curvature, R, and the contact angle, θ [15, 162]:

$$V^{\mathrm{L}} = \int_0^{\theta} \pi R^3 \sin^3\varphi\ \mathrm{d}\varphi = \frac{\pi R^3}{3}(2 - \cos\theta(2 + \sin^2\theta)) = \frac{\pi R^3}{3}(2 - 3\cos\theta + \cos^3\theta), \tag{B.12}$$

$$A^{\mathrm{LV}} = \int_0^{\theta} 2\pi R^2 \sin\varphi \,\mathrm{d}\varphi = 2\pi R^2(1-\cos\theta), \tag{B.13}$$

$$A^{\mathrm{SL}} = \pi R^2 \sin^2\theta. \tag{B.14}$$

To obtain the equilibrium conditions for the defined system, we first take the differential forms of the volume and the interfacial areas, eqs. (B.12)-(B.14) (with respect to both R and θ). We subsequently substitute eqs. (B.2) - (B.4), the constraints (B.5) - (B.11), the derivatives of (B.12) - (B.14) into eq. (B.1) and collect the similar terms, and get the following equation:

$$\begin{aligned}
&\left(\frac{1}{T^{\mathrm{L}}}-\frac{1}{T^{\mathrm{V}}}\right)\mathrm{d}U^{\mathrm{L}} + \left(\frac{P^{\mathrm{R}}}{T^{\mathrm{R}}}-\frac{P^{\mathrm{V}}}{T^{\mathrm{V}}}\right)\mathrm{d}V^{\mathrm{R}} - \left(\frac{\mu_1^{\mathrm{L}}}{T^{\mathrm{L}}}-\frac{\mu_1^{\mathrm{V}}}{T^{\mathrm{V}}}\right)\mathrm{d}N_1^{\mathrm{L}} \\
&\quad + \left(\frac{1}{T^{\mathrm{S}}}-\frac{1}{T^{\mathrm{V}}}\right)\mathrm{d}U^{\mathrm{S}} + \left(\frac{1}{T^{\mathrm{LV}}}-\frac{1}{T^{\mathrm{V}}}\right)\mathrm{d}U^{\mathrm{LV}} \\
&\quad - \left(\frac{\mu_1^{\mathrm{LV}}}{T^{\mathrm{LV}}}-\frac{\mu_1^{\mathrm{V}}}{T^{\mathrm{V}}}\right)\mathrm{d}N_1^{\mathrm{LV}} + \left(\frac{1}{T^{\mathrm{SL}}}-\frac{1}{T^{\mathrm{V}}}\right)\mathrm{d}U^{\mathrm{SL}} \\
&\quad - \left(\frac{\mu_1^{\mathrm{SL}}}{T^{\mathrm{SL}}}-\frac{\mu_1^{\mathrm{V}}}{T^{\mathrm{V}}}\right)\mathrm{d}N_1^{\mathrm{SL}} + \left(\frac{1}{T^{\mathrm{SV}}}-\frac{1}{T^{\mathrm{V}}}\right)\mathrm{d}U^{\mathrm{SV}} \\
&\quad - \left(\frac{\mu_1^{\mathrm{SV}}}{T^{\mathrm{SV}}}-\frac{\mu_1^{\mathrm{V}}}{T^{\mathrm{V}}}\right)\mathrm{d}N_1^{\mathrm{SV}} + \left(\frac{1}{T^{\mathrm{R}}}-\frac{1}{T^{\mathrm{V}}}\right)\mathrm{d}U^{\mathrm{R}} \\
&\quad + \Bigg[\left(\frac{P^{\mathrm{L}}}{T^{\mathrm{L}}}-\frac{P^{\mathrm{V}}}{T^{\mathrm{V}}}\right)(2-\cos\theta(2+\sin^2\theta))\pi R^2 \\
&\quad - \frac{\gamma^{\mathrm{LV}}}{T^{\mathrm{LV}}}(1-\cos\theta)4\pi R + \frac{(\gamma^{\mathrm{SV}}-\gamma^{\mathrm{SL}})}{T^{\mathrm{SL}}}(2\pi R\sin^2\theta)\Bigg]\mathrm{d}R \\
&\quad + \Bigg[\left(\frac{P^{\mathrm{L}}}{T^{\mathrm{L}}}-\frac{P^{\mathrm{V}}}{T^{\mathrm{V}}}\right)(\sin\theta(2+\sin^2\theta)-2\sin\theta\cos^2\theta)\frac{\pi R^3}{3} \\
&\quad - \frac{\gamma^{\mathrm{LV}}}{T^{\mathrm{LV}}}2\pi R^2\sin\theta + \frac{(\gamma^{\mathrm{SV}}-\gamma^{\mathrm{SL}})}{T^{\mathrm{SL}}}(2\pi R^2\sin\theta\cos\theta)\Bigg]\mathrm{d}\theta = 0.
\end{aligned} \tag{B.15}$$

For the above expression to be valid for any arbitrary displacement about equilibrium, the coefficients in front of each differential must be equal to zero. Setting all the coefficient of each independent variation to zero, yielding to the following equilibrium conditions:

$$T^{\mathrm{L}} = T^{\mathrm{LV}} = T^{\mathrm{S}} = T^{\mathrm{SL}} = T^{\mathrm{SV}} = T^{\mathrm{V}} = T^{\mathrm{R}}, \tag{B.16}$$

$$\mu_1^{\mathrm{L}} = \mu_1^{\mathrm{LV}} = \mu_1^{\mathrm{SL}} = \mu_1^{\mathrm{SV}} = \mu_1^{\mathrm{V}}, \tag{B.17}$$

$$P^{\mathrm{R}} = P^{\mathrm{V}}. \tag{B.18}$$

In addition, the Laplace equation and Young equation can be obtained by setting the coefficients in front of dR and dθ to zero in eq. (B.15) as follows:

$$P^{\mathrm{L}} - P^{\mathrm{V}} = \frac{2\gamma^{\mathrm{LV}}}{R}, \tag{B.19}$$

$$\gamma^{\mathrm{SV}} - \gamma^{\mathrm{SL}} = \gamma^{\mathrm{LV}} \cos\theta. \tag{B.20}$$

Given these equilibrium conditions, assuming that the pressure in the system is constant, and moving terms to the right-hand side, eq. (B.15) is simplified to:

$$-(\gamma^{\mathrm{SV}} - \gamma^{\mathrm{SL}})A^{\mathrm{SL}} + \gamma^{\mathrm{LV}} A^{\mathrm{LV}} = 0. \tag{B.21}$$

Therefore, the total free energy of this system, E, is:

$$E = (\gamma^{\mathrm{SL}} - \gamma^{\mathrm{SV}})A^{\mathrm{SL}} + \gamma^{\mathrm{LV}} A^{\mathrm{LV}}, \tag{B.22}$$

which has the common form of the free energy as follows [159, 160, 161, 162]:

$$E = G^{\mathrm{V}} + F^{\mathrm{L}} + F^{\mathrm{S}} + F^{\mathrm{SL}} + F^{\mathrm{LV}} + F^{\mathrm{SV}} + P^{\mathrm{V}} V^{\mathrm{L}}, \tag{B.23}$$

where G and F are Gibbs and Helmholtz free energies, respectively. As mentioned before, since the energy should be calculated with respect to a reference level, we choose the system of a spherical drop with no SL contact area as a reference point, and we assume that it is an equilibrium state. The total energy of this reference state, E_0, is given by:

$$E_0 = 4\pi R_0^2 \gamma^{\mathrm{LV}}. \tag{B.24}$$

Therefore, the change of the free energy of the current system with respect to the assumed reference point, $E - E_0$ is equal to:

$$E - E_0 = (\gamma^{\mathrm{SL}} - \gamma^{\mathrm{SV}})A^{\mathrm{SL}} + \gamma^{\mathrm{LV}} A^{\mathrm{LV}} - 4\pi R_0^2 \gamma^{\mathrm{LV}}, \tag{B.25}$$

which has the same form as the free energy derived by Shardt et al. [91] for SDS surfactant drops on hydrophobic microstructures. If the current state of the system is also assumed in an equilibrium state, and by substituting the previous derived equilibrium condition, eq. (B.20) and eq. (B.13) - (B.14) for the LV and SL areas, respectively, the final form of the free energy, $E - E_0$, is equal to:

$$E - E_0 = \pi R^2 \gamma^{\mathrm{LV}} (2 - 3\cos\theta + \cos^3\theta) - 4\pi R_0^2 \gamma^{\mathrm{LV}}, \tag{B.26}$$

where E_0 is the reference free energy; defined as the free energy of a spherical drop with no SL contact, R is the spherical cap radius of curvature, R_0 is the initial radius of a spherical drop of 10 μl, and $\cos\theta = f\cos\theta_{\mathrm{Y}} - f_1$. Here, f is the ratio of the SL surface area (pillar-top area) to the total (liquid-solid and liquid-gas) areas. f_1 is the ratio of the LV interfatial area to the total projected area beneath the drop. Finally, eq. (B.26) can be used to predict the free energy difference related to the reference state for a CB, an intermediate, or a Wenzel state, depending on the parameter values of f and f_1.

A CB to Wenzel wetting transition may be modeled through two main processes [15, 16]. Initially, right after droplet deposition, a droplet wetting in the classical CB wetting state has $f = \phi$ and $f_1 = 1 - \phi$. In the first phase, the liquid penetrates the surface structure until it wets the bottom of the surface. We assume that the liquid wets the cylinders walls only, and the bottom surface is not wet, so the value of f increases from ϕ to $(\frac{\pi D^2}{4} + \pi DH)/(P^2)$ since the solid–liquid contact area increases and $f_1 = 1 - f$ does not change. In the second phase, liquid wets the bottom surface from the edges of pillars towards the center, as f continues to increase while $f_1 = r - f$ until the area below the drop is fully wetted. A fully transition of the droplet to W occurs when $f = r$ and $f_1 = 0$, and hence $\cos\theta = r\cos\theta_{\mathrm{Y}}(C_{\mathrm{S}})$ as in the Wenzel equation [8, 9, 15].

B.4 Derivation of the metastability criterion for Cassie-Baxter state

To explain the stability and metastability of CB state, we use a similar approach to the proposed free energy analysis by Gong et al. for a pure water on a square-post microstructures [16]. They outline that there is an energy barrier between CB and W states based on the first derivative of the free energy barrier (i.e., $E_{max} - E_0$, where E_{max} is the maximum free energy state) with respect to the variable f as follows:

$$\left.\frac{\partial(E_{max} - E_{CB})}{\partial f}\right|_{f=\phi} > 0. \tag{B.27}$$

Shardt et al. [16] used the same approach to analyze sodium dodecyl sulfate (SDS) surfactant-laden drops on hydrophobic microstructures. To apply eq. (B.27), we first substitute the variable R in eq. (B.26) by the corresponding value from the spherical cap volume approximation, i.e., eq. (B.12). We subsequently replace the variable $\cos\theta$ by $\cos\theta = f\cos\theta_{\mathrm{Y}} - f_1$, where $f_1 = 1 - \phi$ as in the first process of CB-W transition. We obtained the energy barrier, $E_{max} - E_0$, by substituting all theses values into eq. (B.26) and simplifying the equation:

$$E_{max} - E_0 = \pi^{1/3}(3V^{\mathrm{L}})^{2/3}\gamma^{\mathrm{LV}}\Big\{2 - 3[f\cos\theta_{\mathrm{Y}} - (1-\phi)] + [f\cos\theta_{\mathrm{Y}} - (1-\phi)]^3\Big\}^{1/3} - 4\pi R_0^2\gamma^{\mathrm{LV}}. \tag{B.28}$$

The first partial derivative of eq. (B.28) for the first process of CB-W transition with respect to f is:

$$\left.\frac{\partial(E_{max} - E_0)}{\partial f}\right|_{f=\phi} = \frac{\pi^{1/3}(3V^{\mathrm{L}})^{2/3}\gamma^{\mathrm{LV}}[3\cos\theta_{\mathrm{Y}}(f\cos\theta_{\mathrm{Y}} + \phi - 1)^2 - 3\cos\theta_{\mathrm{Y}}]}{3[(f\cos\theta_{\mathrm{Y}} + \phi - 1)^3 - 3(f\cos\theta_{\mathrm{Y}} + \phi - 1) + 2]^{2/3}}. \tag{B.29}$$

Note that the common term in the nominator $\pi^{1/3}(V^{\mathrm{L}})^{2/3}\gamma^{\mathrm{LV}}$ and the denominator $3[(f\cos\theta_{\mathrm{Y}} + \phi - 1)^3 - 3(f\cos\theta_{\mathrm{Y}} + \phi - 1) + 2]^{2/3}$ are always positive. To get the solution for eq. (B.27) and based on the above observation, eq. (B.29) is simplified to:

$$\cos\theta_{\mathrm{Y}}(\phi\cos\theta_{\mathrm{Y}} + \phi - 1)^2 - \cos\theta_{\mathrm{Y}} > 0. \tag{B.30}$$

The above equation can be simplified further to the following form:

$$\phi^2\cos^3\theta_{\mathrm{Y}} - 2\phi(1-\phi)\cos^2\theta_{\mathrm{Y}} + (1-\phi)^2\cos\theta_{\mathrm{Y}} - \cos\theta_{\mathrm{Y}} > 0. \tag{B.31}$$

To solve for the ranges of $\cos\theta_{\mathrm{Y}}$ (or θ_Y) that fulfills the eq. (B.31) criteria, we first set the left hand side of eq. (B.31) $=0$, which has three roots:

$$\cos\theta_{\mathrm{Y}} = -1, 0, \frac{-\phi+2}{\phi}. \tag{B.32}$$

Since the values of the packing fraction, ϕ, are restricted to the range between 0 and 1 ($0 < \phi < 1$), and the range of the cosine function is from -1 to 1, there is no possible solution for $(-\phi+2)/(\phi)$ because $(-\phi+2)/(\phi)$ is always greater than 1. Therefore, for the solution of eq. (B.31) criteria to be valid for the presence of a metastable CB (i.e., with a presence of energy barrier), only two remaining roots are possible: $\cos\theta_{\mathrm{Y}} = -1$ and 0, which corresponds to $\theta_{\mathrm{Y}} = 180°$ and $90°$, respectively. To fulfill the eq. (B.31) criteria would require that the cosine function of the Young's equation should be $-1 < \cos\theta_{\mathrm{Y}} < 0$. In other words, the solution to eq. (B.31) is $90° < \theta_{\mathrm{Y}} < 180°$. Consequently, there is an energy barrier observed for both SH surfaces studied when $\theta_{\mathrm{Y}} > 90°$. In contrast, in the case of $\theta_{\mathrm{Y}} < 90°$, the first derivative of the free energy with respect to f will be less than 0 (as $\partial E/\partial f|_{f=\phi} < 0$), and thus a stable W will always occur at any values of r and ϕ when $\theta_{\mathrm{Y}} < 90°$.

To locate the metastable regime, we used and calculated the critical point at the CB to Wenzel wetting transition, which is given by $\cos\theta^*_{\mathrm{Y}} = \frac{\phi-1}{r-\phi}$ (described in the main text) to locate the upper boundary, above which a CB state is more stable thermodynamically. For our two studied surfaces S1 ($\phi = 0.34$ and $r = 2.31$) and S2 ($\phi = 0.08$ and $r = 1.33$), the predicted critical Young angles are $\theta^*_{\mathrm{Y}} = 109.6°$ and $\theta^*_{\mathrm{Y}} = 137.4°$, respectively. Consequently, the metastable regime is located between 90° and θ^*_{Y} (see Fig. 6c in the main text). In this $\theta_{\mathrm{Y}}(C_{\mathrm{S}})$-range, there is an energy barrier, and hence a CB state is metastable.

Appendix C

Derivation of the critical contact angle for "Fabrication of transparent and microstructured superhydrophobic substrates using additive manufacturing"

C.1 Derivation of the critical contact angle

The total surface energy for a CB or a Wenzel droplet on the 3D-printed microtexture, denoted by E_{CB} and E_W, respectively, can be modeled by [11, 13, 14, 15, 16]:

$$E_{\mathrm{CB}} = N\ [\gamma_{\mathrm{ls}} D^2 + \gamma_{\mathrm{sg}}(4Dh + P^2 - D^2) + \gamma_{\mathrm{lg}}(P^2 - D^2)] + \gamma_{\mathrm{lg}} S_{\mathrm{cap}}\ , \tag{C.1}$$

$$E_{\mathrm{W}} = N\ [\gamma_{\mathrm{ls}}(P^2 + 4Dh)] + \gamma_{\mathrm{lg}} S_{\mathrm{cap}}, \tag{C.2}$$

where $N = \frac{S_\mathrm{b}}{P^2}$ is the number of asperities beneath the drop, γ_ls, γ_sg, and γ_lg are the interfacial tensions for the liquid-solid, solid-gas, and liquid-gas interfaces, respectively, S_cap is the spherical cap surface area of the water drop entirely in contact with the air, and S_b is the base surface area. Here, we assume flat menisci beneath the drop. Using the Young–Duprè equation [194], $\gamma_\mathrm{ls} = \gamma_\mathrm{sg} - \gamma_\mathrm{lg} \cos\theta_\mathrm{Y}$, the total surface energies for the two states on the superhydrophobic microstructures can be calculated using the roughness, r, and the solid fraction, ϕ:

$$E_\mathrm{CB} = S_\mathrm{b} \left[\gamma_\mathrm{sg} r + \gamma_\mathrm{lg}(1 - \phi\ (1 + \cos\theta_\mathrm{Y}))\right] + \gamma_\mathrm{lg} S_\mathrm{cap}\ , \tag{C.3}$$

$$E_\mathrm{W} = S_\mathrm{b} \left[\gamma_\mathrm{sg} r - \gamma_\mathrm{lg} r \cos\theta_\mathrm{Y}\right] + \gamma_\mathrm{lg} S_\mathrm{cap}. \tag{C.4}$$

The energy difference, $E_{CB} - E_W$, allows us to predict the critical contact angle θ^* when $E_{CB} = E_W$. Using the above two equations, one can arrive

$$\cos\theta^* = \frac{\phi - 1}{r - \phi}. \tag{C.5}$$

Theoretically, a CB droplet is thermodynamically more stable when $E_{CB} < E_W$, which corresponds to a larger contact angle, $\theta > \theta^*$.